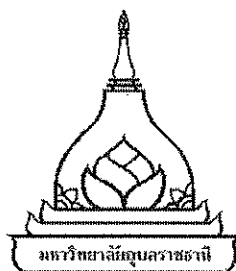


**CFD EVALUATION OF SUITABLE GEOMETRICAL LOCATION OF
WIND TURBINE INSTALLED OVER TERRAIN**

THITIPONG UNCHAI

**A THESIS SUBMITTED IN PARTIAL FULFILLMENT OF THE REQUIREMENTS
FOR THE DEGREE OF DOCTOR OF PHILOSOPHY
MAJOR IN MECHANICAL ENGINEERING
FACULTY OF ENGINEERING
UBON RACHATHANI UNIVERSITY
YEAR 2012**

COPYRIGHT OF UBON RACHATHANI UNIVERSITY



THESIS APPROVAL

UBON RATCHATHANI UNIVERSITY

DOCTOR OF PHILOSOPHY

MAJOR IN MECHANICAL ENGINEERING FACULTY OF ENGINEERING

TITLE CFD EVALUATION OF SUITABLE GEOMETRICAL LOCATION OF
WIND TURBINE INSTALLED OVER TERRAIN

NAME MR.THITIPONG UNCHAI

THIS THESIS HAS BEEN ACCEPTED BY

.....*Adun Janyalertadun*.....

CHAIR

(ASST.PROF.DR.ADUN JANYALERTADUN)

.....*Umphisak*.....

COMMITTEE

(ASST.PROF.DR.UMPHISAK TEEBOONMA)

.....*[Signature]*.....

COMMITTEE

(ASST.PROF.DR.DENPONG SOODPHAKDEE)

.....*[Signature]*.....

DEAN

(ASST.PROF.DR.NOTE SANGTIAN)

APPROVAL BY UBON RATCHATHANI UNIVERSITY

.....*Utith Inprasit*.....

(ASSOC.PROF.DR.UTITH INPRASIT)

VICE PRESIDENT FOR ACADEMIC AFFAIRS

FOR THE PRESIDENT OF UBON RATCHATHANI UNIVERSITY


ACADEMIC YEAR 2012

ACKNOWLEDGEMENT

I would like to express my special gratitude to my supervisors Asst. Prof. Adun Janyalertadun, Ph.D. Department of Mechanical Engineering at Ubonratchathani University and Prof. Arne Erik Holdø, Ph.D. Department of Energy and Environmental Technology at Narvik University College, Norway. I am grateful for their follow-up through the entire process. They have all contributed to this thesis with good general advice and feedback. In addition, they have provided me with expert advice in different fields. I would like to thank my very grateful mom for support all of my life. I want to thank my sister for mathematical proof of this thesis. I want to thank my beloved wife and daughter for plentifully affection.

I would like to thank the Office of the Higher Education Commission, Thailand for supporting by grant fund under the program Strategic Scholarships for Frontier Research Network for the Ph.D. Program Thai Doctoral degree for this research. I would like to thank Thai Meteorological Department of Ubonratchathani for meteorological data and instruments to use in this thesis.

Finally, I want to remember my beloved dad.



(Mr. Thitipong Unchai)

Researcher

บทคัดย่อ

ชื่อเรื่อง : การประเมินตำแหน่งทางเรขาคณิตที่เหมาะสมสำหรับติดตั้งกังหันลมกรณี
การไหลผ่านเนินเขาด้วยการจำลองการไหลของพลศาสตร์

โดย : จุติพงษ์ อุ่นใจ

ปริญญา : ปรัชญาคุณบัณฑิต

สาขาวิชา : วิศวกรรมเครื่องกล

ประธานกรรมการที่ปรึกษา : ผู้ช่วยศาสตราจารย์ ดร.อดุลย์ จรรยาเลิศอดุลย์

ศัพท์สำคัญ : พลังงานลม การจำลองของไหลพลศาสตร์ แบบจำลองความปั่นป่วน
เนินเขารูปทรงสี่เหลี่ยมคางหมู

งานวิจัยนี้ได้ศึกษาตำแหน่งทางเรขาคณิตที่เหมาะสมสำหรับติดตั้งกังหันลมกรณีการไหลผ่านเนินเขาด้วยการจำลองการไหลของพลศาสตร์ โดยในส่วนของงานได้ทำการบันทึกข้อมูลลมรายชั่วโมงของจังหวัดอุบลราชธานี ที่ระดับความสูง 10, 30 และ 40 เมตร เป็นระยะเวลา 3 ปี ตั้งแต่วันที่ 1 มกราคม 2551 ถึงวันที่ 31 ธันวาคม 2553 เพื่อประเมินความหนาแน่นพลังงานลม โดยศึกษาการกระจายตัวของ Weibull ด้วยวิธีการประมาณค่าผลการวิเคราะห์พบว่าความหนาแน่นพลังงานลมของจังหวัดอุบลราชธานี ที่ระดับความสูง 10, 30 และ 40 เมตร มีค่า 9.61, 34.10 และ 90.00 วัตต์ต่อตารางเมตร ตามลำดับ

ส่วนที่สองของงานวิจัยมุ่งประเด็นไปที่การจำลองของไหลพลศาสตร์ เพื่อศึกษาดำเนินการศักยภาพลมจากผาแต้ม โดยเปรียบเทียบระหว่างผลที่ได้จากการทดลองและผลจากการจำลองของไหลพลศาสตร์ แบบจำลองความปั่นป่วนที่นำมาใช้ในการจำลองได้แก่ แบบจำลอง standard k- ϵ , แบบจำลอง standard k- ω และแบบจำลอง Reynolds Stress ซึ่งผลที่ได้จากการทดลองพบว่าผลที่ได้จากแบบจำลอง standard k- ϵ มีความแม่นยำเทียบกับการทดลองในบริเวณก่อนเข้าปะทะเนินเขา หลังการปะทะ แบบจำลอง Reynolds Stress จะให้ผลสอดคล้องกับการทดลองมากที่สุด ตั้งแต่ระยะ $x/H = 1.0$ เป็นต้นไป ส่วนผลจากแบบจำลอง standard k- ϵ และแบบจำลอง standard k- ω ให้ผลที่มีค่าต่ำกว่าการทดลองมาก

ส่วนที่สามนำเสนอผลการจำลองเปรียบเทียบระหว่างผาแต้มที่มีรูปทรงสอดคล้องกับรูปทรงสี่เหลี่ยมคางหมู โดยแบบจำลองภูมิประเทศที่ใช้สำหรับการจำลองของไหลพลศาสตร์ได้นำเข้ามาจากข้อมูลสารสนเทศภูมิศาสตร์ ที่ความละเอียด 1:50,000 เพื่อศึกษาและนำเสนอตำแหน่งศักยภาพลมของเนินเขาเมื่อมีการเปลี่ยนแปลงความเร็วลม มุมชั้นของเนินเขา และความขรุขระของพื้นผิว ผลการจำลองแสดงให้เห็นว่าสำหรับเนินเขาที่มีความคล้ายคลึงกับรูปทรงเลขาคณิตที่ระดับร้อยละ 95.46 จะแสดงตำแหน่งศักยภาพลมที่มีความคลาดเคลื่อนเพียงร้อยละ 9.72

ในส่วนท้ายได้นำเสนอชุดแผนภาพแสดงตำแหน่งศักยภาพลมสำหรับการไหลผ่านเนินเขารูปทรงสี่เหลี่ยมคางหมู ซึ่งขยายด้วยวิธีการประมาณค่านอกช่วงให้ครอบคลุมเงื่อนไขเริ่มต้นที่ความเร็วลม 2 – 40 เมตรต่อวินาที ความขรุขระของพื้นผิว 0.0001 – 0.1 เมตร และมุมชั้นของเนินเขา 5 - 45°

ABSTRACT

TITLE : CFD EVALUATION OF SUITABLE GEOMETRICAL LOCATION OF
WIND TURBINE INSTALLED OVER TERRAIN

BY : THITIPONG UNCHAI

DEGREE : DOCTOR OF PHILOSOPHY (MECHANICAL ENGINEERING)

MAJOR : MECHANICAL ENGINEERING

CHAIR : ASST. PROF. ADUN JANYALERTADUN, Ph.D.

KEYWORDS : WIND ENERGY / COMPUTATIONAL FLUID DYNAMICS /
TURBULENCE MODEL / TRAPEZOID TERRAIN

This research investigated to find geometrical location of wind turbine installed over terrain using Computational Fluid Dynamics techniques. In first period of the paper, the hourly measured wind data from 1st January 2008 to 31st December 2010 at 10 m, 30 m and 40 m height for Ubon Ratchathani province have been statically analyzed to determine the energy potential of wind power generation. Weibull distribution parameters have been estimated and compared annually and on monthly bases was designated in this paper as approximated method, which depends on the standard deviation and average wind speed. The average annual wind power density at 10 m, 30 m and 40 m height was found to be 9.61 W/m², 34.10 W/m² and 90.00 W/m², respectively.

The second period of the thesis focuses on the flow dependency on the comparison results from measurements and simulations of Pha Taem terrain to show optimization turbulence model and possibility of replacing measurement with simulation. The standard k- ϵ model, standard k- ω model and Reynolds Stress Model have been applied in this section. Results of the standard k- ϵ model are comparing precisely with the measures in front of the hill top; while the Reynolds Stress Model showed exactly result after $x/H = 1.0$ but standard k- ϵ model and standard k- ω model showed more underestimation.

Third, comparison of Pha Taem terrain and reference geometry has been applied to investigate the resembling. The 1:50,000 scale data of Geographic Information System was imported to be a geographic model of the simulations to find relation of suitable site of turbine with depended wind speed, hill angle and roughness height. The initial and boundary conditions of the reference geometry and the geography illustrated 95.46 % matching terrain have 9.72 % of suitable site error.

Finally, series of the wind turbine suitable site charts for trapezoid terrain are presented. The extrapolate technique have been used to expand the chart to cover 2 – 40 m/s of background wind speed, 0.0001 – 0.1 m of roughness height and 5 - 45° of hill angle.

CONTENTS

	PAGE
ACKNOWLEDGEMENTS	I
THAI ABSTRACT	II
ENGLISH ABSTRACT	IV
CONTENTS	VI
LIST OF TABLES	IV
LIST OF FIGURES	XI
LIST OF ABBREVIATION SYMBOLS	XIV
CHAPTER	
1 INTRODUCTION	
1.1 Background and motivation	1
1.2 Objective	2
1.3 Scope of the work	2
2 THEORY	
2.1 Meteorology of wind	5
2.2 Wind energy potential assessment	8
2.3 Wind speed statistics	9
2.4 Computational fluid dynamics	13
2.5 Turbulence model	20
2.6 Geographic information system	25
2.7 Extrapolation technique	29
3 LITERATURE REVIEWS	
3.1 Meteorology of wind	31
3.2 Wind energy potential assessment	34
3.3 Computational fluid dynamics	36
3.4 Topographic data from geographic information system	40

CONTENTS (CONTINUED)

	PAGE
4 MATERIALS AND METHODS	
4.1 Weather station	42
4.2 Measurement site	46
4.3 Wind potential calculation	47
4.4 Terrain model	48
4.5 Grid dependence	49
4.6 Initial and boundary conditions	51
4.7 Processing	52
4.8 Generate wind turbine suitable site chart	53
5 RESULTS AND DISCUSSIONS	
5.1 Wind energy potential assessment	55
5.2 Grid dependence	69
5.3 Simulation results of Pha Taem hill	70
5.4 Comparison of Pha Taem geography and geometry shape	78
5.5 Generate wind turbine suitable site chart	82
6 CONCLUDING REMARKS	
6.1 Wind energy potential assessment	89
6.2 Simulation of Pha Taem hill	89
6.3 Comparison of hill shape and geometry shape	90
6.4 Generate wind turbine suitable site chart	90
6.5 Suggestion and comments for farther study	90
REFERENCES	91

CONTENTS (CONTINUED)

	PAGE
APPENDICES	
A Wind data of Ubonratchathani in year 2008 – 2010	98
B Simulation results of Pha Taem and trapezoid geometry	102
C Wind turbine suitable site chart for trapezoid terrain	106
D List of publication from this thesis	115
E Wind turbine suitable site chart instruction manual	120
F List of publications from this work	125
VITAE	126

LIST OF TABLES

TABLE		PAGE
2.1	Electricity consumption and percent of electricity import for the whole country	5
2.2	Power classes of wind	9
2.3	Generalized representation of transport equations	16
4.1	Technical specifications of the KRIWAN INT10 barometer	43
4.2	Technical specifications of the KRIWAN INT30 wind direction sensors	43
4.3	Technical specifications of the temperature transmitter probe	44
4.4	Technical specifications of the P-GE 8/11 digital barometers	44
4.5	Technical specifications of the HIOKI 8421-51(32ch) data logger	45
4.6	Essential sizes of the grid dependence test	50
4.7	Initial and boundary conditions of the simulations	52
4.8	Typical canopy height in surrounding	54
5.1	Weibull parameters calculated using graphical method and approximated method at 10 m height	59
5.2	Weibull parameters calculated using graphical method and approximated method at 30 m height	60
5.3	Weibull parameters calculated using graphical method and approximated method at 40 m height	61
5.4	Monthly wind speed and power density calculated using Weibull parameters for years 2008–2010 in Ubonratchathani at a height of 10 m	64
5.5	Monthly wind speed and power density calculated using Weibull parameters for years 2008–2010 in Ubonratchathani at a height of 30 m	65
5.6	Monthly wind speed and power density calculated using Weibull parameters for years 2008–2010 in Ubonratchathani at a height of 40 m	66

LIST OF TABLES (CONTINUED)

TABLE		PAGE
A.1	The frequency of wind speeds for height of 10 m for year 2008-2010	99
A.2	The frequency of wind speeds for height of 30 m for year 2008-2010	100
A.3	The frequency of wind speeds for height of 40 m for year 2008-2010	101
B.1	Parameters in Weibull approximation method for wind power density calculation	105
E.1	Typical roughness length	122

LIST OF FIGURES

FIGURE	PAGE
2.1 ASEAN power grid interconnection projects	4
2.2 Coriolis force	8
2.3 A finite volume in one dimension	18
2.4 Raster model represented divided geographic space	27
4.1 Experimental setup for meteorological measurement	46
4.2 Flowchart of wind power calculation	47
4.3 Location and contours of Pha Taem hill	48
4.4 Pha Taem terrain topography	49
4.5 Grid visualization of terrain coding	50
4.6 Distribution of grids cells used in the simulations coding	51
4.7 Hill angle distance structure and variable	53
5.1 Mean monthly wind speed data at 10 m height	55
5.2 Mean monthly wind speed data at 30 m height	56
5.3 Mean monthly wind speed data at 40 m height	56
5.4 Diurnal mean wind speeds variation	57
5.5 Probability density function of wind speeds at 10 m height	62
5.6 Probability density function of wind speeds at 30 m height	62
5.7 Probability density function of wind speeds at 40 m height	63
5.8 Polar diagram of wind direction for the year 2008-2010 in Ubonratchathani	68
5.9 Grid resolution sensitivity	70
5.10 Wind velocity profile at reference station	71
5.11 Comparison of increasing speed at hill top	72
5.12 Comparison of velocity in longitudinal direction	73
5.13 Comparison of turbulence kinetic energy in longitudinal direction	75
5.14 Mean velocity component in the longitudinal direction	77
5.15 Pha Taem topography associate with reference trapezoid geometry	79

LIST OF FIGURES (CONTINUED)

FIGURE	PAGE
5.16 Increasing of velocity comparison of Pha Taem hill topography and reference geometry shape	80
5.17 Comparison of turbulence kinetic energy increasing of the flow over Pha Taem hill topography and reference geometry shape	81
5.18 Suitable position from simulation results of the flow over trapezoid geometry terrain	82
5.19 Suitable site chart for trapezoid hill shape at 0.0001 m of roughness height	85
5.20 Suitable site chart for trapezoid hill shape at 0.001 m of roughness height	86
5.21 Suitable site chart for trapezoid hill shape at 0.01 m of roughness height	87
5.22 Suitable site chart for trapezoid hill shape at 0.1 m of roughness height	88
C.1 Filled contour plot of the velocity magnitude from the flow over terrain calculated with k- ϵ turbulence model	107
C.2 Filled contour plot of the velocity magnitude from the flow over Pha Taem terrain calculated with k- ω turbulence model	107
C.3 Filled contour plot of the velocity magnitude from the flow over terrain calculated with RSM	108
C.4 Filled contour plot of the vertical velocity from the flow over terrain calculated with k- ϵ turbulence model	108
C.5 Filled contour plot of the vertical velocity from the flow over terrain calculated with k- ω turbulence model	109
C.6 Filled contour plot of the vertical velocity from the flow over terrain calculated with RSM	109
C.7 Filled contour plot of the static pressure from the flow over terrain calculated with k- ϵ turbulence model	110
C.8 Filled contour plot of the static pressure from the flow over terrain calculated with k- ω turbulence model	110

LIST OF FIGURES (CONTINUED)

FIGURE		PAGE
C.9	Filled contour plot of the static pressure from the flow over terrain calculated with RSM	111
C.10	Filled contour plot of the turbulence kinetic energy from the flow over terrain calculated with k- ϵ turbulence model	111
C.11	Filled contour plot of the turbulence kinetic energy from the flow over terrain calculated with k- ω turbulence model	112
C.12	Filled contour plot of the turbulence kinetic energy from the flow over terrain calculated with RSM	112
C.13	Filled contour plot of the turbulence intensity from the flow over terrain calculated with k- ϵ turbulence model	113
C.14	Filled contour plot of the turbulence intensity from the flow over terrain calculated with k- ω turbulence model	113
C.15	Filled contour plot of the turbulence intensity from the flow over terrain calculated with RSM	114
D.1	Result of SciLab console interface for SciLab 4.1.2 programing	119
E.1	Stage of site selection	123
E.2	Selecting intersection point from the chart	124

LIST OF ABBREVIATION SYMBOLS

SYMBOLS MEAN

A	Area (m^2)
c	Scale factor (m/s)
c_j	Newton extrapolating polynomial coefficients
D	Diffusivity
D_{eff}	Effective values of diffusivity
D_v	Viscous term of Navier-Stokes equation
D_R	Viscous term of Reynolds-averaging equation
E	Wind power density (W/m^2)
F_w	Probability for wind speed
$f_w(V)$	Probability of observed wind speed
G	Filter function
h	Enthalpy
j	Nonnegative integer
k	Shape factor
k_{eff}	Effective values of conductivity
m_r	Mass diffusion
n	Total number of observations
P	Pressure (Pa)
P_m	Mean power of wind (W)
P_w	Power of wind per unit (W)
P_{wma}	Monthly power of wind per unit (W)
P_{wmb}	Weibull monthly power of wind per unit (W)
$q_{i,cmd}$	Heat conduction
T	Temperature ($^{\circ}C$)
\bar{u}	Mean wind speed (m/s)
$\overline{u'_i u'_j}$	Turbulent stresses

LIST OF ABBREVIATION SYMBOLS (CONTINUED)

SYMBOLS MEAN

u_i	Specific wind speed (m/s)
U_j	Reynolds averaged components of the mean flow
V	Wind speed (m/s)
ν_t	Eddy-viscosity
w	Number of different values of wind speed observed
V_m	Average wind speed (m/s)
V_{mWeib}	Weibull average wind speed (m/s)
y^+	Near wall resolution
α_{ijkl}	Fourth rank tensor
$\Gamma(x)$	Gamma function of x
ε	Dissipation rate
μ	Viscosity (kg/s·m)
μ_{eff}	Effective values of viscosity
μ_t	Turbulence viscosity
ρ	Air density (kg/m ³)
ρ_m	Extensive property available in a unit volume
σ	Standard deviation
σ^2	Variance
τ_{ij}	Reynolds stress
Φ	Mean value of flow variables
ϕ'	Fluctuating part of flow variables
ω	Specific dissipation rate

CHAPTER 1

INTRODUCTION

1.1 Background and motivation

The world energy consumption has increased significantly in last decade that seems fossil fuels will terminate in recently year. However, the uses of fossil fuels create serious environmental problems, including acid emissions, air pollution and climate changed in finally. So, many countries provide renewable energy such as solar, wave, geothermal and wind energy. Nowadays, the use of wind energy technology developed very fast [1-5]. Given that wind power is a local resource that clean and environmentally friendly.

The Energy Policy and Planning Office of Thailand (EPPO) indicated electricity consumption is 134,729.89 GWh in year 2009, which 2,460.09 GWh imported from neighbor countries. The cumulative electricity energy consumption is increasing by an average of 10.5% and 39.9% from year 2005 and 1999, respectively. Main energy resources using in Thailand are crude oil, coal and natural gas. The reports of EPPO showed in 31st December 2008 raw energies reserved were 183 MMBBL of crude oil and 12,003 BCF of natural gas [6]. Wind energy is an alternative energy which assists to reduce electrical energy imported and environmental friendly.

Ubonratchathani region has 16,112 square kilometers with 1.8 million populations [7] on plateau in northeastern of Thailand. The average ground level is situated at approximately 123 m from sea level. The 51.07% of region is farmland, while 78% of electricity used is from household and agricultures [6].

In order to study wind power in a particular site, the long-term records of wind data have to be statistically analyzed. A practical method of quantitative analysis of wind data can be performed by establishing the wind speed pattern, level and prevailing direction. To avoid the time and expense associated with processing multiple year to records the data, it is very important to describe the variation of wind speeds with statistical functions for optimizing the design of the systems. The most widely used functions, which are used to fit a measured wind speed probability distribution in a given site over a certain period of time, are Weibull and Rayleigh distribution

functions. Weibull distribution has been used to assess the potential of wind power in many countries [8-12]. The Rayleigh distribution has been also widely used to fit the measured probability distribution functions for different locations [13-17].

Computational fluid dynamics technique were used worldwide to investigated suitable site for installed the turbines. Effect of roughness surface, wall function problem, turbulent model was simulated [7-11] to adopt maximum energy from the wind. Commercially available CFD codes with turbulent models were used in this thesis because their ready availability well developed interface and broad verification and validation.

1.2 Objective

1.2.1 Investigate wind energy potential of Ubonratchathani region.

1.2.2 Find suitable location of wind turbine install over terrain using Computational Fluid Dynamics simulations.

1.2.3 Generate suitable geometrical location chart of wind turbine installed for the flow over terrain.

1.3 Scope of the work

From the objectives of this thesis, thus the scope of the study may best be summarized as follows,

1.3.1 Wind data collection

The wind data were collected from 1st January, 2008 to 31st December, 2010. The sampling periods are 60 minutes and the altitude of the measurement point was 10 m, 30 m and 40 m height. The main focuses are on investigating possibility of the region.

1.3.2 Wind energy potential assessment

Statistical analyses have been used to determine the potential of wind power. Weibull distribution parameters have been estimated and compared annually on monthly power, which depends on the standard deviation and average wind speed.

1.3.3 Simulation of Pha Taem hill

To investigate optimal turbulence model for the simulations, the Reynolds Stress Model, standard k- ϵ model and standard k- ω model adopt to be initial conditions of the simulations. The results are compared with results from the experiments to find optimal turbulence model for next procedure.

1.3.4 Comparison of hill shape and geometry shape

The Pha Taem hill topography is similar with trapezoid shape. To investigate suitable site of wind turbine matching with real topography, the reference geometry was used to associate with the hill structure.

1.3.5 Generate wind turbine suitable site chart

The simulation results of the flow over topography and reference geometry are compares to find suitable site to install turbine for varying hill angle, wind speed and roughness height. Suitable of turbine site and position are present in series of line charts.

CHAPTER 2

THEORY

The growing environmental concern of air quality around the world were created a move to green sources of energy such as wind and solar which provide a pollution-free electricity. Wind is plentiful source available in the nature which utilized by mechanically converting wind power to electrical energy using wind turbine.

Thailand is located in south-east of Asia. Figure 2.1 shows ASEAN power grid interconnection projects (APG) which establish by ASEAN Plan of Action Energy Cooperation (APAEC) in 2003 to maximize the use of regional power and resources. Table 2.1 indicated electricity consumption of Thailand from year 1990 to 2009, which increasing 352.83 % in last two decades. As is known, the petroleum crisis in the end quarter of the 20th century has turned the attention of universities and other investigation foundations to new and renewable energy resources. Wind is rapidly becoming a practical source of energy for electric utilities around the world. Many firms in different countries have undertaken development of commercial wind power plants. Wind is expected to be an important source of electric energy in the future in many regions of Thailand.

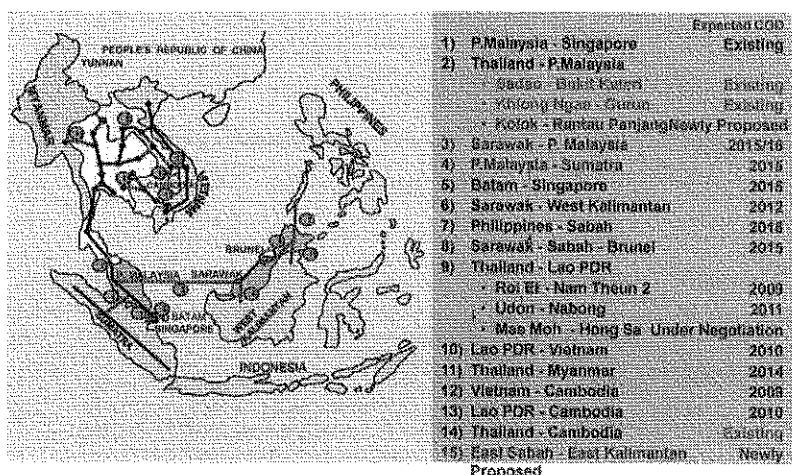


Figure 2.1 ASEAN power grid interconnection projects

Table 2.1 Electricity consumption and percent of electricity import for the whole country

Year	Electricity consumption for whole country (GWH)	Import of electricity (GWH)	Percent of electricity import (%)
1990	38,202.96	599.50	1.57
1991	44,238.87	593.11	1.34
1992	49,331.17	479.88	0.97
1993	55,231.29	644.51	1.17
1994	62,558.02	870.82	1.39
1995	70,870.31	699.12	0.99
1996	77,082.95	805.61	1.05
1997	81,998.02	745.63	0.91
1998	79,899.63	1,622.71	2.03
1999	80,985.50	2,255.66	2.79
2000	87,747.09	2,966.26	3.38
2001	93,020.68	2,881.76	3.10
2002	99,407.11	2,812.18	2.83
2003	106,207.83	2,473.41	2.33
2004	114,325.66	3,377.85	2.95
2005	120,637.37	4,371.89	3.62
2006	127,237.24	5,151.85	4.05
2007	132,492.12	4,488.36	3.39
2008	134,936.63	2,783.57	2.06
2009	134,792.89	2,460.09	1.83

2.1 Meteorology of wind

The earth's atmosphere can be modeled as a gigantic heat engine. It extracts energy from the sun and delivers heat to another reservoir at a lower temperature as space. In the process, work is done on the gases in the atmosphere and upon the earth-atmosphere boundary. There will

be regions where the air pressure is temporarily higher or lower than average. This difference in air pressure causes atmospheric gases or wind to flow from the region of higher pressure to that of lower pressure. These regions are typically hundreds of kilometers in diameter.

Wind is simply air in motion. It is caused by the uneven heating of the Earth's surface by the sun. Because the Earth's surface is made of very different types of land and water, it absorbs the sun's heat at different rates. One example of this uneven heating can be found in the daily wind cycle. During the day, the air above the land heats up more quickly than the air over water. The warm air over the land expands and rises, and the heavier, cooler air rushes in to take its place, creating wind. At night, the winds are reversed because the air cools more rapidly over land than over water. In the same way, the atmospheric winds that circle the earth are created because the land near the Earth's equator is heated more by the sun than the land near the North and South Poles.

Within the atmosphere, there will be large regions of alternately high and low pressure. These regions are formed by complex mechanisms, which are still not fully understood. Solar radiation, surface cooling, humidity, and the rotation of the earth all play important roles. In order for a high pressure region to be maintained while air is leaving it at ground level, there must be air entering the region at the same time. The only source for this air is above the high pressure region. That is, air will flow down inside a high pressure region (and up inside a low pressure region) to maintain the pressure. This descending air will be warmed adiabatically (i.e. without heat or mass transfer to its surroundings) and will tend to become dry and clear. Inside the low pressure region, the rising air is cooled adiabatically, which may result in clouds and precipitation. This is why high pressure regions are usually associated with good weather and low pressure regions with bad weather.

The greater the pressure gradient, the greater is the force on the air, and the higher is the wind speed. Since the direction of the force is from higher to lower pressure, and perpendicular to the isobars, the initial tendency of the wind is to blow parallel to the horizontal pressure gradient and perpendicular to the isobars. However, as soon as wind motion is established, a deflective force is produced which alters the direction of motion. This force is called the Coriolis force.

The Coriolis force is due to the earth's rotation under a moving particle of air. From a fixed observation point in space air would appear to travel in a straight line, but from our vantage point on earth it appears to curve. To describe this change in observed direction, an equivalent force is postulated.

The basic effect is shown in Figure 2.2. The two curved lines are lines of constant latitude, with point *B* located directly south of point *A*. A parcel of air (or some projectile like a cannon ball) is moving south at point *A*. If we can imagine our parcel of air or our cannon ball to have zero air friction, then the speed of the parcel of air will remain constant with respect to the ground. The direction will change, however, because of the earth's rotation under the parcel. At point *A*, the parcel has the same eastward speed as the earth. Because of the assumed lack of friction, it will maintain this same eastward speed as it moves south. The eastward speed of the earth increases, however, as we move south (in the Northern Hemisphere). Therefore, the parcel will appear to have a westward component of velocity on the latitude line passing through point *B*. During the time required for the parcel to move from the first latitude line to the second, point *A* has moved eastward to point *A'* and point *B* has moved eastward to point *B'*. The path of the parcel is given by the dashed line. Instead of passing directly over point *B'* which is directly south of point *A'*, the parcel has been deflected to the right and crosses the second latitude line to the west of *B'*. The total speed relative to the earth's surface remains the same, so the southward moving component has decreased to allow the westward moving component of speed to increase.

Another statement we shall accept on faith is that the deflection of the parcel of air must cease when the wind direction becomes parallel to the isobars. Otherwise the wind would be blowing in the direction of increasing pressure, which would be like water running uphill. Since the Coriolis force acts in a direction 90° to the right of the wind, it must act in a direction opposite to the pressure gradient at the time of maximum deflection. If there are no other forces present, this Coriolis force will exactly balance the pressure gradient force and the wind will flow parallel to the isobars, with higher pressure to the right of the wind direction. For straight or slightly curved isobars this resultant wind is called the geostrophic wind.

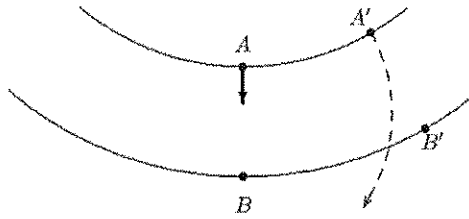


Figure 2.2 Coriolis force

2.2 Wind potential energy assessment

Wind power is the conversion of wind energy into a useful form of energy, such as using wind turbines to make electricity, windmills for mechanical power, wind pumps for water pumping or drainage, or sails to propel ships.

The power of the wind that flows at speed V through a blade sweep area A increases with the cube of the wind speed and the area, that is,

$$P(V) = \frac{1}{2} \rho A V^3 \quad (2.1)$$

The wind power density of a site based on a probability density function can be expressed as follows:

$$E = \frac{P}{A} = \int_0^{\infty} \frac{1}{2} \rho V^3 f(V) dV \quad (2.2)$$

This equation can be used to calculate the available wind energy for any defined period of time when the wind speed frequency distributions are for a different period of time. The Betz limit, which has been commonly used now for decades, gives that a wind turbine would not extract more than 59% of the available wind power. Therefore, the maximum extractable power from the wind will be the product of the factor 0.59 and the calculated result from Equation 2.2.

To assess potential site of wind power energy, mean wind speed in class 4 and above are adopt to be suitable and sufficiency for install turbines and generate electricity power in

wind industrial. However, lower wind speed in class 1 – 3 are sufficiency for cut-in speed of commercial wind turbines which have mean cut-in speed about 2.5 – 3.0 m/s as indicated wind power class and speed in Table 2.2. Therefore, mentions of suitable site in poor efficiency site are important for local site and under 1,000 W turbines.

Table 2.2 Power classes of wind

Wind Power Class	Height of 10 m		Height of 50 m	
	Wind Power	Speed	Wind Power	Speed
	Density (W/m ²)	(m/s)	Density (W/m ²)	(m/s)
1	0 – 100	0 – 4.4	0 – 200	0 – 5.6
2	100 – 150	4.4 – 5.1	200 – 300	5.6 – 6.4
3	150 – 200	5.1 – 5.6	300 – 400	6.4 – 7.0
4	200 – 250	5.6 – 6.0	400 – 500	7.0 – 7.5
5	250 – 300	6.0 – 6.4	500 – 600	7.5 – 8.0
6	300 – 400	6.4 – 7.0	600 – 800	8.0 – 8.8
7	400 – 1,000	7.0 – 9.4	800 – 2,000	8.8 – 11.9

2.3 Wind speed statistics

The speed of the wind is continuously changing, making it desirable to describe the wind by statistical methods. We shall pause here to examine a few of the basic concepts of probability and statistics, leaving a more detailed treatment to the many books written on the subject.

One statistical quantity which we have mentioned earlier is the average or arithmetic mean. If we have a set of numbers u_i , such as a set of measured wind speeds, the mean of the set is defined as

$$\bar{u} = \frac{1}{n} \sum_{i=1}^n u_i \quad (2.3)$$

where \bar{u} is mean wind speed (m/s) u_i is specific wind speed (m/s) and the sample size or the number of measured values is n .

Another quantity seen occasionally in the literature is the median. If n is odd, the median is the middle number after all the numbers have been arranged in order of size. As many numbers lie below the median as above it. If n is even the median is halfway between the two middle numbers when we rank the numbers.

In addition to the mean, we are interested in the variability of the set of numbers. We want to find the discrepancy or deviation of each number from the mean and then find some sort of average of these deviations. The mean of the deviations $u_i - \bar{u}$ is zero, which does not tell us much. We therefore square each deviation to get all positive quantities. The variance σ^2 of the data is then defined as

$$\sigma^2 = \frac{1}{n-1} \sum_{i=1}^n (u_i - \bar{u})^2 \quad (2.4)$$

The standard deviation σ is then defined as the square root of the variance.

$$\text{Standard deviation} = \sqrt{\text{variance}} \quad (2.5)$$

Wind speeds are normally measured in integer values, so that each integer value is observed many times during a year of observations. The numbers of observations of a specific wind speed u_i will be defined as m_i . The mean is then

$$\bar{u} = \frac{1}{n} \sum_{i=1}^w m_i u_i \quad (2.6)$$

where w is the number of different values of wind speed observed and n is still the total number of observations.

It can be shown that the variance is given by

$$\sigma^2 = \frac{1}{n-1} \left[\sum_{i=1}^w m_i u_i^2 - \frac{1}{n} \left(\sum_{i=1}^w m_i u_i \right)^2 \right] \quad (2.7)$$

The two terms inside the brackets are nearly equal to each other so full precision needs to be maintained during the computation. This is not difficult with most of the hand calculators that are available.

2.3.1 Weibull distribution

The probability distribution, which is widely used to describe the long-term records of wind speeds, is Weibull distribution. The probability density function of a Weibull distribution is given by

$$f_w(V) = \frac{k}{c} \left(\frac{V}{c} \right)^{k-1} \exp \left(- \left(\frac{V}{c} \right)^k \right) ; (k > 0, V > 0, c > 1) \quad (2.8)$$

where, $f_w(V)$ is the probability of observed wind speed, k is the shape factor, c is the scale factor, and V is the wind speed. The cumulative distribution function is given by

$$F_w(V \leq V_0) = 1 - e \left[- \left(\frac{V_0}{c} \right)^k \right] \quad (2.9)$$

where, F_w represents the probability for the speed V to be less than or equal to V_0 . There are several methods used to determine the shape factor and scale factor [18-20]. In this work the approximated method [19] have been used.

The shape factor and scale factor of Weibull distribution are given as [19]

$$k = \left(\frac{\sigma}{V_m} \right)^{-1.086} \quad (1 \leq k \leq 10) \quad (2.10)$$

$$c = \frac{V_m}{\Gamma(1+1/k)} \quad (2.11)$$

where, σ is the standard deviation, V_m is the average wind speed, $\Gamma(x)$ is the gamma function of x which is defined by the following integral

$$\Gamma(x) = \int_0^{\infty} t^{x-1} e^{-t} dt \quad (2.12)$$

2.3.2 Estimation of wind speed and power density

The monthly average wind speed using Weibull and Rayleigh distributions is determined, respectively, as [21]

$$V_{mWei} = c \Gamma\left(1 + \frac{1}{k}\right) \quad (2.13)$$

The power of the wind per unit area is given as

$$P_w = \frac{1}{2} \rho V^3 \quad (2.14)$$

where, ρ is the air density which adopt from the weather station.

The average power density for each month is calculated using actual probability density distribution for the specified month, which is calculated using Equation (2.14), and is given as

$$P_{Wma} = \sum_{i=1}^n \frac{1}{2} \rho V_{mi}^3 f(V_i) \quad (2.15)$$

where, The subscript m stands for the month and n is the number of records for the specified month.

The average power density using Weibull probability distribution is calculated as follows [22]

$$P = \frac{1}{2} \rho c^3 \Gamma \left[1 + \frac{3}{k} \right] \quad (2.16)$$

where Γ is the gamma function and given as

$$\Gamma(x) = \int_0^{\infty} \xi^{x-1} e^{-\xi} d\xi \quad (2.17)$$

where,

$$\xi = \left(\frac{V_{mi}}{c} \right)^k \quad (2.18)$$

2.4 Computational fluid dynamics

Computational fluid dynamics (CFD) is concerned with numerical solution of differential equations governing transport of mass, momentum, and energy in moving fluids. CFD activity emerged and gained prominence with availability of computers in the early 1960s. Today, CFD finds extensive usage in basic and applied research, in design of engineering equipment, and in calculation of environmental and geophysical phenomena. Since the early 1970s, commercial software packages (or computer codes) became available, making CFD an important component of engineering practice in industrial, defense and environmental organizations.

For a long time, design (as it relates to sizing, economic operation, and safety) of engineering equipment such as heat exchangers, furnaces, cooling towers, internal combustion engines, gas turbine engines, hydraulic pumps and turbines, aircraft bodies, sea-going vessels, and rockets depended on painstakingly generated empirical information. The same was the case with numerous industrial processes such as casting, welding, alloying, mixing, drying, air-conditioning, spraying, environmental discharging of pollutants and so on. The empirical information is typically displayed in the form of correlations or tables and nomograms among the main

influencing variables. Such information is extensively availed by designers and consultants from handbooks.

The main difficulty with empirical information is that it is applicable only to the limited range of scales of fluid velocity, temperature, time, or length for which it is generated. Thus, to take advantage of economies of scale, for example, when engineers were called upon to design a higher capacity power plant, boiler furnaces, condensers, and turbines of ever higher dimensions had to be designed for which new empirical information had to be generated all over again. The generation of this new information was by no means an easy task. This was because the information applicable to bigger scales had to be, after all, generated via laboratory-scale models. This required establishment of scaling laws to ensure geometric, kinematic and dynamic similarities between models and the full-scale equipment. This activity required considerable experience as well as ingenuity, for it is not an easy matter to simultaneously maintain the three aforementioned similarities. The activity had to, therefore, be supported by flow-visualization studies and by simple (typically, one-dimensional) analytical solutions to equations governing the phenomenon under consideration. Ultimately, experience permitted judicious compromises. Being very expensive to generate, such information is often of a proprietary kind. In more recent times, of course, scaling difficulties are encountered in the opposite direction. This is because electronic equipment is considerably miniaturized and, in materials processing, for example, the more relevant phenomena occur at micro scales (even molecular or atomic scales where the continuum assumption breaks down). Similarly, small-scale processes occur in biocells.

Clearly, designers need a design tool that is scale neutral. The tool must be scientific and must also be economical to use. An individual designer can rarely, if at all, acquire or assimilate this scale neutrality. Fortunately, the fundamental laws of mass, momentum, and energy, in fact, do embody such scale-neutral information. The key is to solve the differential equations describing these laws and then to interpret the solutions for practical design.

The potential of fundamental laws (in association with some further empirical laws) for generating widely applicable and scale-neutral information has been known almost ever since they were invented nearly 200 years ago. The realization of this potential (meaning the ability to solve the relevant differential equations), however, has been made possible only with the

availability of computers. The past five decades have witnessed almost exponential growth in the speed with which arithmetic operations can be performed on a computer.

By way of reminder, we note that the three laws governing transport are the following:

- (1) The law of conservation of mass (transport of mass)
- (2) Newton's second law of motion (transport of momentum)
- (3) The first law of thermodynamics (transport of energy).

2.4.1 Governing equations

The afore mentioned laws are applied to an infinite small control volume located in a moving fluid. This application results in partial differential equations (PDEs) of mass, momentum and energy transfer. Here, it will suffice to mention that the law of conservation of mass is written for a single-component fluid or for a mixture of several species. When applied to a single species of the mixture, the law yields the equation of mass transfer when an empirical law, namely, Fick's law of mass diffusion ($m_j'' = -\rho D \partial \omega_j / \partial x_j$), is invoked. Newton's second law of motion, combined with Stokes's stress laws, yields three momentum equations for velocity in directions x_j ($j = 1, 2, 3$). Similarly, the first law of thermodynamics in conjunction with Fourier's law of heat conduction ($q_{i, \text{cond}} = -K \partial T / \partial x_i$) yields the so-called energy equation for the transport of temperature T or enthalpy h . Using tensor notation, we can state these laws as follows:

2.4.1.1 Conservation of Mass for the Mixture

$$\frac{\partial \rho_m}{\partial t} + \frac{\partial (\rho_m u_j)}{\partial x_j} = 0 \quad (2.19)$$

2.4.1.2 Equation of Mass Transfer for Species k

$$\frac{\partial (\rho_m \omega_k)}{\partial t} + \frac{\partial (\rho_m u_j \omega_k)}{\partial x_j} = \frac{\partial}{\partial x_j} \left[\rho_m D_{\text{eff}} \frac{\partial \omega_k}{\partial x_j} \right] + R_k \quad (2.20)$$

2.4.1.3 Momentum Equations u_i ($i = 1, 2, 3$)

$$\frac{\partial (\rho_m u_i)}{\partial t} + \frac{\partial (\rho_m u_j u_i)}{\partial x_j} = \frac{\partial}{\partial x_j} \left[\mu_{\text{eff}} \frac{\partial u_i}{\partial x_j} \right] - \frac{\partial p}{\partial x_i} + \rho_m B_i + S_{u_i} \quad (2.21)$$

2.4.1.4 Energy Equation in Enthalpy Form

$$\frac{\partial(\rho_m h)}{\partial t} + \frac{\partial(\rho_m u_j h)}{\partial x_j} = \frac{\partial}{\partial x_j} \left[\frac{k_{\text{eff}}}{C_{pm}} \frac{\partial h}{\partial x_j} \right] + Q''' \quad (2.22)$$

where enthalpy $h = C_{pm} (T - T_{\text{ref}})$, and

2.4.1.5 Energy Equation in Temperature Form

$$\frac{\partial(\rho_m T)}{\partial t} + \frac{\partial(\rho_m u_j T)}{\partial x_j} = \frac{\partial}{\partial x_j} \left[\frac{k_{\text{eff}}}{C_{pm}} \frac{\partial T}{\partial x_j} \right] + \frac{Q'''}{C_{pm}} \quad (2.23)$$

In these equations, the suffix m refers to the fluid mixture. For a single component fluid, the suffix may be dropped and the equation of mass transfer becomes irrelevant. Similarly, the suffix *eff* indicates effective values of mass diffusivity D , viscosity μ , and thermal conductivity k . In laminar flows, the values of these transport properties are taken from property tables for the fluid under consideration. In turbulent flows, however, the transport properties assume values much in excess of the values ascribed to the fluid; moreover, the effective transport properties turn out to be properties of the flow [23], rather than those of the fluid. From the point of view of further discussion of numerical methods, it is indeed a happy coincidence that the set of Equations 2.19 - 2.23 can be cast as a single equation for a general variable Φ . Thus,

Table 2.3 Generalized representation of transport equations

Equation	Φ	Γ_{eff} (ex ch coefficient)	S_Φ (net source)
2.19	1	0	0
2.20	ω_k	$\rho_m D_{\text{eff}}$	R_k
2.21	u_i	μ_{eff}	$-\frac{\partial p}{\partial x_i} + \rho_m B_i$ $+ S_{u_i}$
2.22	h	k_{eff}/C_{pm}	Q'''
2.23	T	k_{eff}/C_{pm}	Q'''/C_{pm}

The meanings of Γ_{eff} and S_{Φ} for each Φ are listed in Table 2.3. Equation 2.23 is called the transport equation for property Φ . The rate of change (or time derivative) term is to be invoked only when a transient phenomenon is under consideration. The term $\rho_m \Phi$ denotes the amount of extensive property available in a unit volume. The convection term accounts for transport of Φ due to bulk motion. This first-order derivative term is relatively uncomplicated but assumes considerable significance when stable and convergent numerical solutions are to be economically obtained. Both the transient and the convection terms require no further modelling or empirical information.

The greatest impediment to obtaining physically accurate solutions is offered by the diffusion and the net source (S) terms because both these terms require empirical information. In laminar flows, the diffusion term represented by the second-order derivative offers no difficulty because, Γ being a fluid property, can be accurately determined (via experiments) in isolation of the flow under consideration. In turbulent (or transitional) flows, however, determination of Γ_{eff} requires considerable empirical support. This is labeled as turbulence modelling. This extremely complex phenomenon has attracted attention for over 150 years. Although turbulence models of adequate generality (at least, for specific classes of flows) have been proposed, they by no means satisfy the expectations of an equipment designer. These models determine Γ_{eff} from simple algebraic empirical laws. Sometimes, Γ_{eff} is also determined from other scalar quantities (such as turbulent kinetic energy and its dissipation rate) for which differential equations are constituted. Fortunately, these equations often have the form of Equation 2.23.

The term net source implies an algebraic sum of sources and sinks of Φ . Thus, in a chemically reacting flow, a given species k may be generated via some chemical reactions and destroyed (or consumed) via some others and R_k will comprise both positive and negative contributions. Also, some chemical reactions may be exothermic, whereas others may be endothermic, making positive and negative contributions to Q''' . Similarly, the term B_i in the momentum equations may represent a buoyancy force, a centrifugal and Coriolis force, an electromagnetic force, etc. Sometimes, B_i may also represent resistance forces. Thus, in a mixture of gas and solid particles (as in pulverized fuel combustion), B_i will represent the drag offered by the particles on air, or, in a fluid flow through a densely filled medium (a porous body or a shell-and-tube geometry), the resistance will be a function of the porosity of the medium.

Such empirical resistance laws are often determined from experiments. The S_{u_i} terms represent viscous terms arising from Stokes's stress laws that are not accounted for in the $\frac{\partial}{\partial x_j} \left[\mu_{\text{eff}} \frac{\partial u_i}{\partial x_j} \right]$ term in Equation 2.21.

2.4.2 Finite volume methods

The finite volume method is currently the most popular method in CFD. The main reason is that it can resolve some of the difficulties that the other two methods have. Generally, the finite volume method is a special case of finite element, when the function W is equal to 1 everywhere in the domain.

A typical finite volume, or cell, is shown in Figure 2.2. In this figure the centroid of the volume, point P , is the reference point at which we want to discretize the partial differential equation.

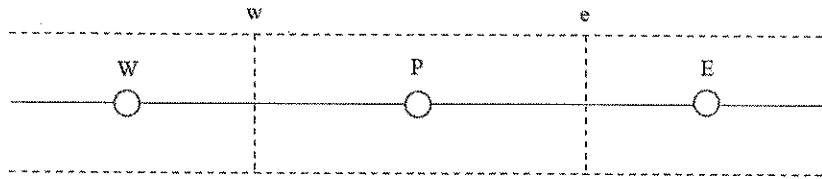


Figure 2.3 A finite volume in one dimension

The neighboring volumes are denoted as, W , volume to the west side, and E , the volume to the east side of the volume P . For the one-dimensional finite volume shown in Figure 2.3, the volume with centroid P , has two boundary faces at w and e .

The second derivative of a variable at P can be written as the difference between the first derivatives of the variable evaluated at the volume faces

$$\left[\frac{\partial^2 u}{\partial x^2} \right]_P = \frac{\left[\left(\frac{\partial u}{\partial x} \right)_e - \left(\frac{\partial u}{\partial x} \right)_w \right]}{x_e - x_w} \quad (2.24)$$

The first derivatives at the volume faces can be written as to be the differences in the values of the variable at the neighboring volume centroids

$$\left[\frac{\partial u}{\partial x} \right]_e = \frac{u_E - u_P}{x_E - x_P} \quad (2.25)$$

and

$$\left[\frac{\partial u}{\partial x} \right]_w = \frac{u_P - u_W}{x_P - x_W} \quad (2.26)$$

We can apply this technique in Equation 2.22 to obtain its finite volume formulation. The above method is also referred to as the Cell Centered (CC) Method, where the flow variables are allocated at the center of the computational cell. The CC variable arrangement is the most popular, since it leads to considerably simpler implementations than other arrangements. On the other hand, the CC arrangement is more susceptible to truncation errors, when the mesh departs from uniform rectangles.

Traditionally the finite volume methods have used regular grids for the efficiency of the computations. However, recently, irregular grids have become more popular for simulating flows in complex geometries. Obviously, the computational effort is more when irregular grids are used, since the algorithm should use a table to lookup the geometrical relationships between the volumes or element faces. This involves finding data from a disk store of the computer, which increases the computational time.

2.4.3 Navier-Stokes equations

The Navier-Stokes equations form a coupled system of nonlinear PDE's describing the conservation of mass, momentum and energy for a fluid. For a Newtonian fluid in one dimension, they can be written as

$$\frac{\partial Q}{\partial t} + \frac{\partial E}{\partial x} = 0 \quad (2.27)$$

Many flows of engineering interest are steady (time-invariant), or at least may be treated as such. For such flows, we are often interested in the steady-state solution of the Navier-Stokes equations, with no interest in the transient portion of the solution. The steady solution to the one-dimensional Navier-Stokes equations must satisfy

$$\frac{\partial E}{\partial x} = 0 \quad (2.28)$$

If we neglect viscosity and heat conduction, the Euler equations are obtained. In two-dimensional Cartesian coordinates, these can be written as

$$\frac{\partial Q}{\partial t} + \frac{\partial E}{\partial x} + \frac{\partial F}{\partial y} = 0 \quad (2.29)$$

The Navier-Stokes equations include both convective and diffusive fluxes. This motivates the choice of our two scalar model equations associated with the physics of convection and diffusion. Furthermore, aspects of convective phenomena associated with coupled systems of equations such as the Euler equations are important in developing numerical methods and boundary conditions. Thus we also study linear hyperbolic systems of PDE's.

2.5 Turbulence model

Turbulence flow is complicate to define precisely, and is most often described by its properties. The first property of turbulence described by Panofsky and Dutton, states that the fluid velocity is a chaotic and apparently random function of both space and time. This means that the turbulent information is contained in the velocity fluctuations. The only expression containing the velocity fluctuations is the Reynolds stresses, which therefore represent the turbulence of the flow. Another property of the turbulence is non-linearity. The Reynolds stresses are also non-linear terms, in accordance with its property are in the Reynolds Averaged Navier-Stokes equations:

$$\rho \frac{\partial U_i}{\partial t} + U_j \frac{\partial U_i}{\partial x_j} = -\frac{1}{\rho} \frac{\partial p}{\partial x_i} - \frac{\partial \overline{U_i U_j}}{\partial x_j}, \quad (2.30)$$

$$\frac{\partial U_i}{\partial x_i} = 0 \quad (2.31)$$

where U_j is the Reynolds averaged components of the mean flow, P is the pressure ρ is the density and $\overline{u_i u_j}$ with an over bar are turbulent stresses. This formulation includes both vertical and horizontal turbulent flux divergence. Equations for each of the six Reynolds stresses and dissipation are solved at each time step to close the mean equations. The model equations are solved using a fractional step method in which the equation for pressure is derived in such a way that it ensures a divergence-free momentum field.

2.5.1 Eddy-viscosity models

The eddy-viscosity concept is based on similarity reasoning, with turbulence being a physical concept connected to the viscosity. In the Navier-Stokes equation the viscous term is

$$D_v = \frac{\partial}{\partial x_j} \left[\nu \left(\frac{\partial U_i}{\partial x_j} + \frac{\partial U_j}{\partial x_i} \right) \right] \quad (2.32)$$

It can be argued that similarly to viscosity, turbulence affects the dissipation, diffusion and mixing processes. Thus it is reasonable to model the Reynolds stresses in a fashion closely related to the viscous term. The Reynolds stress term produced by the Reynolds-averaging is

$$D_R = \frac{\partial R_{ij}}{\partial x_j} = \frac{\partial}{\partial x_j} - (\overline{u'_i u'_j}) \quad (2.33)$$

A turbulent flow will, compared to a laminar flow, enhance the above properties, and thus a model for the Reynolds stress could be

$$-\overline{u'_i u'_j} = \alpha_{ijkl}(x, y, z, t) \left(\frac{\partial U_k}{\partial x_l} + \frac{\partial U_l}{\partial x_k} \right) \quad (2.34)$$

where α_{ijkl} is a fourth rank tensor.

In the Eddy-viscosity models concept this coefficient loses the directional properties, and hence turbulence becomes isotropic, the spatial variation is modeled using some algebraic relation, while the temporal variation is in most cases dropped. Thus the eddy-viscosity ν_t using the Eddy-viscosity models concept is incorporated in the RANS equation as

$$-\overline{u'_i u'_j} = \nu_t(x, y, z) \left(\frac{\partial U_i}{\partial x_j} + \frac{\partial U_j}{\partial x_i} \right) \quad (2.35)$$

This method was first postulated by Boussinesq [24] and consequently denoted the Boussinesq hypothesis.

2.5.2 Reynolds Averaged Navier-Stokes model

The airflow is governed by the Navier-Stokes equation. Since it is not feasible to use Direct Numerical Simulation for solving such a flow, the Navier-Stoke's equation should be approximated in order to make it solvable with the present capacity of computers. By using Reynolds averaged approach, flow variables can be written as

$$\phi = \Phi + \phi' \quad (2.36)$$

where, Φ is the mean value of flow variables, and ϕ' is the fluctuating part of flow variables. On the other hand, LES uses a filter to obtain large-scale flow variables

$$\bar{\phi}(\vec{x}, t) = \iiint_V \phi(\vec{x}, t) G(\vec{x}, \vec{x}', t) d\vec{x}' \quad (2.37)$$

where the over bar denotes the filtered variables, and G is a filter function.

The two methods can transform the Navier-Stoke's equation into a single form

$$\frac{\partial \bar{u}_i}{\partial x_i} = 0 \quad (2.38)$$

$$\frac{\partial \bar{u}_i}{\partial t} + \bar{u}_j \frac{\partial \bar{u}_i}{\partial x_j} = -\frac{1}{\rho} \frac{\partial \bar{P}}{\partial x_i} + \nu \frac{\partial^2 \bar{u}_i}{\partial x_i \partial x_j} \frac{\partial \tau_{ij}}{\partial x_j} \quad (2.39)$$

where the over bar denotes mean variables for Reynolds Averaged Navier-Stokes equations, and filtered variables for Large Eddy Simulation. The term τ_{ij} in the equation is the Reynolds stress for Reynolds Averaged Navier-Stokes equations

$$\tau_{ij} = -\overline{u'_i u'_j} \quad (2.40)$$

and the subgrid-scale stress for Large Eddy Simulation

$$\tau_{ij} = \bar{u}_i \bar{u}_j - \overline{u'_i u'_j} \quad (2.41)$$

Many turbulence models use Boussinesq approximation to simplify the second order symmetrical tensor by correlating it to a scalar ν_t and transform Equation 2.35 into

$$\frac{\partial \bar{u}_i}{\partial t} + \bar{u}_j \frac{\partial \bar{u}_i}{\partial x_j} = -\frac{1}{\rho} \frac{\partial \bar{P}}{\partial x_i} + \frac{\partial}{\partial x_j} \left[(\nu + \nu_t) \frac{\partial \bar{u}_i}{\partial x_j} \right] \quad (2.42)$$

where ν_t is the turbulence viscosity for the Reynolds Averaged Navier-Stokes model and the subgrid-scale turbulence viscosity for Large Eddy Simulation.

2.5.3 k- ϵ model

The standard k- ϵ model is the industrial standards turbulence model in engineering practice. In this case, the transport equations of momentum, potential temperature, mixing ratio of water vapors and turbulence energy was adopted, while the near-wall treatment are enhanced. Because of their computational robustness and efficiency, the two-equation k- ϵ turbulence model and its variants are most commonly used in wind energy researches [25-26]. In particular, they have been extensively validated and calibrated for engineering application flows around bluff bodies and structures [22].

The standard k- \mathcal{E} model [23] is a semi-empirical model based on model transport equations for turbulence kinetic energy (k) and its dissipation rate (\mathcal{E}). The model transport equation for k is derived from the exact equation, while the model transport equation for \mathcal{E} was obtained using physical reasoning and bears little resemblance to its mathematically exact counterpart.

In the derivation of the k- \mathcal{E} model, it was assumed that the flow is fully turbulent, and the effects of molecular viscosity were negligible. The standard k- \mathcal{E} model is therefore valid only for fully turbulent flows, so that

$$\mu_{eff} = \mu + \mu_t \quad (2.43)$$

where μ_t is the turbulence viscosity. The k- \mathcal{E} model assumes that the turbulence viscosity is linked to the turbulence kinetic energy and dissipation via the relation

$$\mu_t = C_\mu \rho \frac{k^2}{\mathcal{E}} \quad (2.44)$$

2.5.4 k- \mathcal{O} model

The standard k- \mathcal{O} model is an empirical model based on model transport equations for the turbulence kinetic energy (k) and the specific dissipation rate (\mathcal{O}), which can also be thought of as the ratio of \mathcal{E} to k [27].

One of the advantages of the k- \mathcal{O} formulation is the near wall treatment for low-Reynolds number computations. The k- \mathcal{O} model does not involve the complex non-linear damping functions required for the k- \mathcal{E} model and is therefore more accurate and more robust. A low-Reynolds k- \mathcal{O} model would typically require a near wall resolution of $y^+ < 0.2$, while a low-Reynolds number k- \mathcal{E} model would require at least $y^+ < 2$. In industrial flows, even $y^+ < 2$ cannot be guaranteed in most applications and for this reason, a new near wall treatment was developed for the k- \mathcal{O} model. It allows for smooth shift from a low-Reynolds number form to a wall function formulation.

The $k-\omega$ models assumes that the turbulence viscosity is linked to the turbulence kinetic energy and turbulent frequency via the relation

$$\mu_t = \rho \frac{k}{\omega} \quad (2.45)$$

2.5.5 Reynolds Stress Model

The Reynolds stress model [28-32] involves calculation of the individual Reynolds stresses, $\overline{u'_i u'_j}$, using differential transport equations. The individual Reynolds stresses are then used to obtain closure of the Reynolds-averaged momentum equation

$$\begin{aligned} \frac{\partial}{\partial t}(\rho u_i) + \frac{\partial}{\partial x_i}(\rho u_i u_j) = & -\frac{\partial p}{\partial x_i} + \frac{\partial}{\partial x_j} \left[\mu \left(\frac{\partial u_i}{\partial x_j} + \frac{\partial u_j}{\partial x_i} - \frac{2}{3} \delta_{ij} \frac{\partial u_l}{\partial x_l} \right) \right] \\ & + \frac{\partial}{\partial x_j} (-\rho \overline{u'_i u'_j}) \end{aligned} \quad (2.46)$$

The exact form of the Reynolds stress transport equations may be derived by taking moments of the exact momentum equation. This is a process where in the exact momentum equations are multiplied by a fluctuating property, the product then being Reynolds averaged. Unfortunately, several of the terms in the exact equation are unknown and modeling assumptions are required in order to close the equations. In this section, the Reynolds stress transport equations are presented together with the modeling assumptions required to attain closure.

2.6 Geographic information system

Geographic information system (GIS) is a system designed to capture, store, manipulate, analyze, manage, and present all types of geographical data. In the simplest terms, geographic information system is the merging of cartography, statistical analysis, and database technology. Geographic information system can be thought of as a system-it digitally creates and manipulates spatial areas that may be jurisdictional, purpose, or application oriented. Generally, geographic information system is custom designed for an organization. Hence, geographic information system developed for an application, jurisdiction, enterprise, or purpose may not be

necessarily interoperable or compatible with the GIS that have been developed for some other application, jurisdiction, enterprise, or purpose. What goes beyond GIS is a spatial data infrastructure (SDI), a concept that has no such restrictive boundaries.

In a general sense, the term describes any information system that integrates stores, edits, analyzes, shares, and displays geographic information for informing decision making. The term GIS-Centric, however, has been specifically defined as the use of the GIS geodatabase as the asset/feature data repository central to computerized maintenance management system (CMMS) as a part of enterprise asset management and analytical software systems. GIS-centric certification criteria have been specifically defined by the National Association of GIS-Centric Solutions (NAGCS). GIS applications are tools that allow users to create interactive queries (user-created searches), analyze spatial information, edit data in maps, and present the results of all these operations [33]. Geographic information science is the science underlying geographic concepts, applications, and systems [34].

2.6.1 GIS uncertainties

The GIS accuracy depends upon source data, and how it is encoded to be data referenced. Land surveyors have been able to provide a high level of positional accuracy utilizing the GPS derived positions [35]. the high-resolution digital terrain and aerial imagery, the powerful computers, Web technology, are changing the quality, utility, and expectations of GIS to serve society on a grand scale, but nevertheless there are other source data that has an impact on the overall GIS accuracy like: paper maps that are not found to be very suitable to achieve the desired accuracy since the aging of maps affects their dimensional stability.

In developing a digital topographic data base for a GIS, topographical maps are the main source of data. Aerial photography and satellite images are extra sources for collecting data and identifying attributes which can be mapped in layers over a location facsimile of scale. The scale of a map and geographical rendering area representation type are very important aspects since the information content depends mainly on the scale set and resulting local ability of the map's representations. In order to digitize a map, the map has to be checked within theoretical dimensions, and then scanned into a raster format, and resulting raster data has to be given a theoretical dimension by a rubber sheeting/warping technology process as shown in Figure 2.4.

A quantitative analysis of maps brings accuracy issues into focus. The electronic and other equipment used to make measurements for GIS is far more precise than the machines of conventional map analysis. All geographical data are inherently inaccurate, and these inaccuracies will propagate through GIS operations in ways that are difficult to predict.

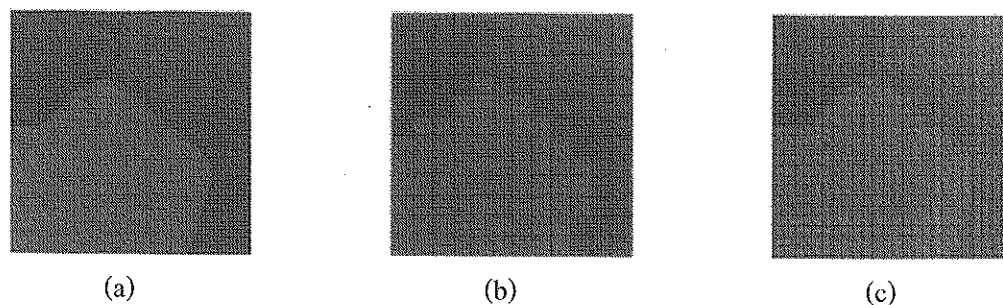


Figure 2.4 Raster model represented divided geographic space

(a) geographic (b) large grid cell (c) small grid cell

2.6.2 Data representation

GIS data represents real objects such as roads, land use, elevation, trees, waterways, etc. with digital data determining the mix. Real objects can be divided into two abstractions: discrete objects e.g., a house, tree and continuous fields such as rainfall amount, or elevations. Traditionally, there are two broad methods used to store data in a GIS for both kinds of abstractions mapping references: raster images and vector. Points, lines, and polygons are the stuff of mapped location attribute references. A new hybrid method of storing data is that of identifying point clouds, which combine three dimensional points with RGB information at each point, returning a 3D color image. GIS Thematic maps then are becoming more and more realistically visually descriptive of what they set out to show or determine.

2.6.3 Slope and aspect

Slope, aspect and surface curvature in terrain analysis are all derived from neighborhoods operations using elevation values of a cell's adjacent neighbors. Slope is a function of resolution, and the spatial resolution used to calculate slope and aspect should always be specified [36]

The elevation at a point will have perpendicular tangents passing through the point, in an east-west and north-south direction. These two tangents give two components, $\partial z/\partial x$ and $\partial z/\partial y$, which then be used to determine the overall direction of slope, and the aspect of the slope. The gradient is defined as a vector quantity with components equal to the partial derivatives of the surface in the x and y directions [37].

The calculation of the overall 3 x 3 grid slope and aspect for methods that determine east-west and north-south component use the following formulas respectively

$$\tan S = \sqrt{\left(\frac{\partial z}{\partial x}\right)^2 + \left(\frac{\partial z}{\partial y}\right)^2} \quad (2.47)$$

$$\tan A = \left(\frac{\left(\frac{-\partial z}{\partial y}\right)}{\left(\frac{\partial z}{\partial x}\right)} \right) \quad (2.48)$$

another algorithm for calculating aspect, as follows

$$A = 270^\circ + \arctan \left(\frac{\left(\frac{\partial z}{\partial x}\right)}{\left(\frac{\partial z}{\partial y}\right)} \right) - 90^\circ \left(\frac{\left(\frac{\partial z}{\partial y}\right)}{\left|\frac{\partial z}{\partial y}\right|} \right). \quad (2.49)$$

2.6.4 Data analysis

It is difficult to relate wetlands maps to rainfall amounts recorded at different points such as airports, television stations, and high schools. A GIS, however, can be used to depict two and three dimensional characteristics of the Earth's surface, subsurface, and atmosphere from information points. For example, a GIS can quickly generate a map with isopleth or contour lines that indicate differing amounts of rainfall.

Such a map can be thought of as a rainfall contour map. Many sophisticated methods can estimate the characteristics of surfaces from a limited number of point measurements. A two dimensional contour map created from the surface modeling of rainfall point measurements may be overlaid and analyzed with any other map in a GIS covering the same area.

Additionally, from a series of three-dimensional points, or digital elevation model, isopleth lines representing elevation contours can be generated, along with slope analysis, shaded relief, and other elevation products. Watersheds can be easily defined for any given reach, by computing all of the areas contiguous and uphill from any given point of interest. Similarly, an expected valley way of where surface water would want to travel in intermittent and permanent streams can be computed from elevation data in the GIS.

2.7 Extrapolation Technique

In this session, descriptions of the value compute of an extrapolating polynomial at a given point, using Neville's Method. However, the theorem that serves as the basis for Neville's Method can easily be used to compute the extrapolating polynomial itself. The basic idea is to represent extrapolating polynomials using the Newton form, which uses linear factors involving the extrapolation points, instead of monomials of the form x^j .

Call that if the extrapolation points x_0, \dots, x_n are distinct, then the process of finding a polynomial that passes through the points (x_i, y_i) , $i = 0, \dots, n$, is equivalent to solving a system of linear equations $Ax = b$ that has a unique solution. The matrix A is determined by the choice of basis for the space of polynomials of degree n or less. Each entry a_{ij} of A is the value of the j th polynomial in the basis at the point x_i .

In Newton extrapolation, the matrix A is upper triangular, and the basis functions are defined to be the set $\{N_j(x)\}_{j=0}^n$, where

$$N_0(x) = 1, \quad N_j(x) = \prod_{k=0}^{j-1} (x - x_k), \quad j = 1, \dots, n \quad (2.50)$$

The advantage of Newton extrapolation is that the extrapolating polynomial is easily updated as extrapolation points are added, since the basis functions $\{N_j(x)\}; j = 0, \dots, n$ do not change from the addition of the new points.

The coefficients c_j of the Newton extrapolating polynomial

$$p_n(x) = \sum_{j=0}^n c_j N_j(x) \quad (2.51)$$

are given by

$$c_j = f[x_0, \dots, x_j] \quad (2.52)$$

Where $f[x_0, \dots, x_j]$ denotes the divided difference of x_0, \dots, x_j . The divided difference is defined as follows,

$$\begin{aligned} f[x_i] &= y_i \\ f[x_i, x_{i+1}] &= \frac{y_{i+1} - y_i}{x_{i+1} - x_i}, \end{aligned} \quad (2.53)$$

$$f[x_i, x_{i+1}, \dots, x_{i+k}] = \frac{f[x_{i+1}, \dots, x_{i+k}] - f[x_i, \dots, x_{i+k-1}]}{x_{i+k} - x_i}$$

This definition implies that for each nonnegative integer j , the divided difference $f[x_0, x_1, \dots, x_j]$ only depends on the extrapolation points x_0, x_1, \dots, x_j and the value of $f(x)$ at these points. It follows that the addition of new extrapolation points does not change the coefficients c_0, \dots, c_n . Specifically, we have

$$p_{n+1}(x) = p_n(x) + \frac{y_{n+1} - p_n(x_{n+1})}{N_{n+1}(x_{n+1})} N_{n+1}(x) \quad (2.54)$$

This ease of updating makes Newton extrapolation the most commonly used method of obtaining the interpolating polynomial.

The following result shows how the Newton extrapolating polynomial bears a resemblance to a Taylor polynomial.

CHAPTER 3

LIERATURE REVIEWS

3.1 Meteorology of wind

3.1.1 Wind data measurement for potential energy assessment

The wind data records in this work are from weather station at Khong Chiam meteorological station (latitude $15^{\circ}33'$ N, longitude $105^{\circ}30'$ E) which located in Ubonratchathani province. The 3 anemometers with wind vane, thermometer, barometer and data logger are installed to collect wind data from January 1, 2008 to December 31, 2010. Hourly data have been recorded and analyzed to assess the wind potential in Ubonratchathani. The second wind data record occurs at Pha Taem hill to analyze wind profiles of the flow over the hill. In the process of wind data record, several techniques of wind station installation are publishing as follows.

A. Keyhani et al. [31] installed 10 m height of wind tower over land in open area to collect wind speed and direction for eleven years (1995 - 2005) for three hour period measured. Reason of low tower measure is for assessment wind potential to collect and used for battery charging and water pumping. Tehran is the capital of Iran which located in central of territory, the average wind velocity in such region is measured less than 3 m/s. And the most probable wind direction is in range of 22.5° . Finally, the authors inscribed that the wind energy potential in the capital of Iran, Tehran, is quite promising.

Ramazan Kose [32] installed anemometers at 10 m and 30 m height with wind vane, hygrometer, thermometer and barometer in Dumlupinar University for 20 months to collect wind data. The data logger recorded the parameters measured at the observation station every second, and average, minimum and maximum values and their standard deviation were recorded at 10 min intervals. Among all the data collected during that work, 10% of missing data occurs from problem of battery. The electricity backup unit should be providing for the station to avoid this problem.

Meishen Li and Xianguo Li [38] studied wind data at 10 m above the ground level over a 5 years period (1999 -2003). Wind speed data recorded in km/hr unit and convert to SI unit afterward. The wind flow direction is expressed in tens of degrees. To convert wind speed data, standard formula of unit convert have been applied. This procedure illustrated the conversion of data unit retained actual information of data.

Murat Gokcek et al. [39] measure wind data at 10 m height above the ground as hourly for one year. During the period of measure, affected by mild Mediterranean climate during the summer and experiences a dry and hot period about 4 – 5 months in a year is occurs. Besides, the region is exposed to high pressure of from north during the winter season. Consequently, this region is influenced by the winds blowing from the directions of north in whole year. To avoid the alteration of wind data recorded from effect of climate and storm, long time period record should be provide for 3 years in least.

Murat Gokcek et al and F. Ben Amar [40] collected wind data from 11 weather station in Tunisia. The heights of anemometer in each station are slightly from 6 – 12 m from ground, consequence by its affiliation. The raw data have been improved and Weibull methods used to generate data in same height. The authors introduce to install and collect data from same height as possible at least at 10 m to evade error of the data.

W. Al-Nassar et al. [5] used 46 years recorded of wind speed data from Kuwait international airport to considered wind potential for generate electricity. The hourly period measured have been provide from 10 m height tower. The wind data at heights 15 m, 20 m, 25 m and 30 m were obtained by extrapolation from the data using the Power-Law.

Another literature [41-44] about wind data measurement illustrates similarly technique. The wind tower should be provided 3 anemometers or more to install at least 10 m height from ground. Wind vane, thermometer, barometer, data logger and electricity backup unit are valuable connected for another wind data. The maximum frequency period of data record is enhancing, while hourly recorded measure is adequacy. Long time measurement can be avoiding effect of suddenly storm, 3 years data are sufficiency in scientific procedure.

3.1.2 Wind data measurement for the flow profile investigation

Investigation of wind flow over terrain in computational fluid dynamics technique, the wind flow profile contour and streamline are compare with measure data from site.

Many wind speed measure instrument are installed in horizontal and vertical distance cover whole region of the hill. The position of tower and height of instruments should be considered influent of the terrain.

Shuzo Murakami et al. [45] considered to developed local area wind prediction system for selecting suitable site for windmill. Single wind speed data measurement tower installed on the hill top with three anemometer at 10 m, 20m and 30 m height. The obtain data have been used to compare with tunnel test and simulation results to generate wind profile in another position. So, single wind measure station is not sufficiency to investigate the flow over terrain.

Atsushi Yamaguchi et al. [46] collected wind speed data in a coastal region in single longitudinal plane. The six weather stations installed in a row for 2 km width with 5 anemometers in each station at 10 m, 20 m, 40 m, 70 m and 100 m height. The authors presented that the split-fiber probe can give a reasonable accuracy while the conventional X-wire probe measurement contains a large error because of the existence of reverse flow and strong across wind in complex terrain.

T. Takahashi et al. [7] considered the boundary layer flow over two-dimensional hill. Eight positions of anemometers from ground to one-time of hill height provided to keep wind speed data. For two-dimensional flow, single row of wind speed collected station is abundance. The author mentions that the turbulence velocity shows an almost uniform distribution across the windward ascent slope. The turbulence velocity becomes higher at the upper wake region behind the hill. Finally, the porous fences work as stronger wind breaks and weaken the wind velocity near the hill surface.

Necessity of wind data measurement in this section is to investigate wind flow profile in the flow direction. Three wind measure stations with 4 anemometers at least are abundance to inspected profile and streamline of the flow. Split-fiber probe is greatest to collect wind speed and direction [46] while anemometer is fine and give a reasonable accuracy.

3.2 Wind energy potential assessment

In order to study wind power in a particular site, the long-term records of wind speed have to be statistically analyzed. A practical method of quantitative analysis of wind data can be performed by establishing the wind speed pattern, level and prevailing direction. To avoid the time and expense associated with processing multiple year data records of hourly wind speed data, it is very important to describe the variation of wind speeds with statistical functions for optimizing the design of the systems. The most widely used functions, which are used to fit a measured wind speed probability distribution in a given site over a certain period of time, are Weibull and Rayleigh distribution functions. Weibull distribution has been used to assess the potential of wind power in many countries [8-12]. The Rayleigh distribution has been also widely used to fit the measured probability distribution functions for different locations [13-17].

A. Keyhani, M. Ghasemi-Varnamkhasti, M. Khanali and R. Abbaszadeh [31] measure wind data for eleven years of the capital of Iran, Tehran. Statistical analyses are used to find out the wind energy potential. Also, other wind characteristics with the help of two methods of meteorological and Weibull are assessed to evaluate of which at a height of 10 m above ground level and in open area. Results revealed that the highest and the lowest wind power potential are in April and August, respectively. It was found that the wind potential of the region can be adequate for non-grid connected electrical and mechanical applications, such as wind generators for local consumption, battery charging, and water pumping.

Ramazan Kose [32] investigated the possible wind energy potential in Kutahya, Turkey. The data collected in this observation station between the dates of July 1, 2001 and February 28, 2003 at 30 m height. Values from the established measurements are searched to determine whether electricity can be produced from the wind energy. The mean wind speed does not provide economical electricity production from the wind energy, and the measurements should be evaluated in the long term in accordance with technological developments and reduction in the cost of turbines.

Getachew Bekele, Bjorn Palm [47] investigated wind data from four different sites in Ethiopia, Addis Ababa (09:02N, 38:42E), Mekele (13:33N, 39:30E), Nazret (08:32N, 39:22E), and Debrezeit (8:44N, 39:02E). The results show that for three of the four locations the wind

energy potential is reasonable, with average wind speeds of approximately 4 m/s, and less than 3 m/s for the fourth site.

Fawzi A.L. Jowder [21] measured wind speed data hourly for three years at 10 m, 30 m and 60 m height for Kingdom of Bahrain. Extrapolation of the 10 m data, using the Power law, has been used to determine the wind data at heights of 30 m and 60 m. Weibull distribution parameters have been estimated and compared annually and on monthly bases using two methods; the graphical method and the another method. Weibull probability function, using Weibull parameters estimated from the approximated method, has shown to provide more accurate prediction of average wind speed and average power density than the graphical method.

Meishen Li, Xianguo Li [38] measured at an elevation 10 m above the ground level over 5 years to examine the wind characteristics for the Waterloo region in Canada. Characteristics such as annual, seasonal, monthly and diurnal wind speed variations and wind direction variations are examined. Analysis shows that the day time is the windy time, with 2 p.m. in the afternoon being the windiest moment. Moreover, a model derived from the maximum entropy principle is applied to determine the diurnal, monthly, seasonal and yearly wind speed frequency distributions, and the corresponding Lagrangian parameters are determined.

Ioannis Fyrippis, Petros J. Axaopoulos and Gregoris Panayiotou [48] investigated the wind power potential of Koronos village, a remote location in the northeastern part of Naxos Island, Greece, using real wind data by a measurement mast. The obtained wind characteristics were statistically analyzed using the Weibull and Rayleigh distribution functions. The results from this investigation showed that the selected site falls under Class 7 of the international system of wind classification as the mean annual wind speed recorded in the area was 7.4 m/s and the corresponding annual mean power density was estimated to be 420 W/m^2 .

Weibull and Rayleigh distribution functions are prevalent for assessment wind energy potential in site. Wind speed data recorded from site for several years provided to improved and analyzed. The data used for investigated can be collected in several height, power-law and extrapolate technique have been used to complete this section. The shape parameter k and scalar parameter c can be helpful to inspection raw data, affects of climate in the data can be taken off without transformation of trend line.

3.3 Computational fluid dynamics

Computational fluid dynamics (CFD) is concerned with numerical solution of differential equations governing transport of mass, momentum, and energy in moving fluids. Today, CFD finds extensive usage in basic and applied research, in design of engineering equipment, and in calculation of environmental and geophysical phenomena. Since commercial software packages became available, making CFD an important component of engineering practice in industrial, defense, and environmental organizations.

Recently, researchers searched for investigation of speed, flow and dispersion, energy assessment, turbulence characteristics of wind over hills. Meteorological and computational fluid dynamics technique was used to evaluate the flow.

3.3.1 Boundary conditions dependence

Computational fluid dynamics technique were used worldwide to investigate suitable site for turbines. Effect of roughness surface, wall function problem was simulated to take maximum of energy from the wind. Commercially available CFD codes with turbulence models were used in this article because of their ready availability well developed interface and broad verification and validation.

T. Takahashi et al., [7] investigated turbulence characteristics of a boundary layer flow over a two-dimensional hill with a rough surface through experiments conducted in a wind tunnel under neutral conditions by using a hot wire constant temperature anemometer system. The results can analyze and discussed that peak wind speed increased from 0% to 100% porous fences are dissimilar. The porous fences work as stronger wind breaks and weaken the wind velocity near the hill surface.

Bert Blocken et al. [49] used Fluent 6.2 and Ansys CFX 10.0 commercial software to simulated problem of wall function. The manuscript discusses the problem by focusing on the simulation of a neutrally stratified, fully developed, horizontally homogeneous atmospheric boundary layers over uniformly rough, flat terrain. Irrespective of the type of simulation, the inlet profiles, wall functions and near wall grid resolution used, it is advisable to always assess the extent of horizontal inhomogeneity by a simulation in an empty computational domain prior to the actual simulation with the obstacle models present. Sensitivity tests in an empty computational domain are of critical importance. In addition, for every CFD simulation it is advisable to always

report not only the inlet profiles but also the incident flow profiles obtained from the simulation in the empty domain because they characterize the real flow to which the building models are subjected.

D.M. Hargreaves and N.G. Wright [50] shown the neutral ABL can be maintained along a lengthy fetch but only with a modified law of the wall and with a shear stress applied to the top boundary of the domain. It has been shown that, using the default law of the wall and velocity and turbulence profiles specified at the inlet, the atmospheric boundary layers will not be sustained along an empty fetch.

O. Undheim [51] investigated topographical and roughness effect on the wind flow field. 2D simulation are applied to show how the roughness influences the flow developed under uniform conditions, and how the influence of a roughness change spreads upwards in the boundary layer downstream from the roughness change. The results from the simulations are compared to equivalent values from empirical equations. The terrain effects are found to have great influence on the flow field and the mean wind conditions in an area. To predict the sum of these non-linear effects, simulations performed by a non-linear flow solver are recommended to supplement measurements.

Ove Undheim [52] simulated non-linear Navier-Stokes solver 3DWind in complex terrain. The results were compared with measured data and simulation results from the linearized model WAsP. The simulated mean wind map worked out by WAsP and 3DWind. The differences are not large and would probably not cause big differences in the decision process to locate the turbines. Still there is a tendency that WAsP estimates the areas of highest wind speed conditions to be located closer to the edges of steep terrain. The wind conditions are further estimated to be higher in the valleys for WAsP than for 3DWind.

Initial and boundary conditions in the simulation influent precise results, roughness surface, wall function and atmospheric boundary conditions are significant. Near-wall treatment as non-linear functions is vital for unsteady flow conditions. Roughness condition as height, shear condition and stress can afford more accurate results.

3.3.2 Turbulence model dependence

Ian P. Castro and David D. Apsley [53] present a comparison between numerical and laboratory data of the flow and dispersion over two-dimensional hills of various slopes and

submerged. The standard k- ϵ model, curvature modification and dissipation modification were used in the simulation. Compare the results of simulations with laboratory data. It is shown that a suitably modified k- ϵ turbulence model generally produces reasonable agreement for the mean flow behavior, but somewhat lower values for the turbulent kinetic energy and the lateral plume spread.

T. Takahashi, T. Ohtsu, M.F. Yassin and S.Kato [7] investigate turbulence characteristics of a boundary layer flow over a two-dimensional hill with a rough surface. The 2-D hill with a rough surface was measured and investigated the turbulence characteristics in a turbulent boundary layer. The databases of the measure are getting for validating the CFD method for predicting wind over a local terrain. Results of this work show that the profiles of turbulent energy and Reynolds stress also show almost uniform distributions on the windward ascent slope. In the upper wake region, the turbulence energy is generated and shows an apparent peak.

Pual Carpenter and Nicholas Locke [54] simulated atmospheric boundary layers in a wind tunnel to investigate the wind flow over two-dimensional, 1:1,000 scale hills. Computational fluid dynamics with standard high Reynolds number k- ϵ model has been applied in the simulation. In finally, numerical simulations of the wind flow over the various hill geometries have been compared with wind tunnel test results. Only mean speed comparisons have been included in this paper. The root mean square speeds (V_{rms}) were also calculated but showed poor agreement between the wind tunnel and CFD results.

Keith W. Ayotte [55] used computational fluid dynamics technique with linear and nonlinear turbulence model to assessment the wind energy. Results of the simulation were compared with the measurement from the European Wind Atlas. Comparison with field and wind tunnel measurements show that operation in this expanded parameter space leads to more accurate estimates of wind resource. While improvements in accuracy have resulted, a number of challenges still exist in modeling scales of turbulent motion that are near those of the main topographic features, for example, eddies shed in the lee of steep topographic features.

Ove Undheim [52] used micro-scale flow solver 3DWind in a 2D analysis to investigate both topographical and roughness effects on the wind flow field. Simulations were carried out with three different turbulence models, the mixing length, a k-l and a k- ϵ model.

The results from the simulations are compared to equivalent values from empirical equations. The terrain effects are found to have great influence on the flow field and the mean wind conditions in an area. To predict the sum of these non-linear effects, simulations performed by a non-linear flow solver are recommended to supplement measurements.

D.D. Apsley and M.A. Leschziner [56] investigate A new low-Reynolds-number nonlinear two-equation turbulence model for complex flows. By using the nonlinear stress-strain relationship, the sublayer behavior of all turbulent stresses is reproduced. The extension to nonequilibrium conditions is achieved by sensitizing the model coefficients to strain and vorticity invariants on the basis of formal relations derived from the algebraic Reynolds-stress model. The new model has been applied to a number of complex two dimensional (2-D) flows, and its performance is compared to that of other linear and nonlinear eddy-viscosity closures.

Investigation of the flow over terrain, channel flow domain has been creating for the simulations. Low Reynolds number of atmospheric boundary layers flow with less direction change is applied in this work. The two equations turbulence are widely used to investigated solution such as standard k - ϵ model and standard k - ω model, while standard k - l model proper for interior flow. Another turbulence model widely used for exterior and flow over terrain is Reynolds Stress Model. The RSM methods revolutions the turbulence modelling techniques by managing to close the Reynolds stress transport equation.

The k - ϵ turbulence model solves two transport equations, one for the turbulence kinetic energy k and the other one for its dissipation rate ϵ . As usual for the two equations model, the transport equation for k is derived from the exact equation, while the equation for its dissipation rate is obtained using physical reasoning. In its original form, the k - ϵ model is not sensitized to rotation and curvature effects.

The k - ω turbulence model solves two transport equations, one for the turbulence kinetic energy k and one for the specific dissipation ω . The idea of the k - ω turbulence model is to retain the robust and accurate formulation in the near wall region [57], and to take advantage of the free stream independence of the k - ϵ model in the outer part of the boundary layer. To achieve this, a k - ω formulation of a standard k - ϵ model is derived and merged together with the previous model via a blending function being one in the near wall region to activate the standard k - ω model and zero outside activating the k - ϵ model.

Currently, most of the turbulent flows are studied through the mean of the Reynolds Averaged Navier-Stokes method, where the averaged governing equations are solved for the mean variables. One of the main issues of the Reynolds Averaged Navier-Stokes model approach is to model the terms, mainly the Reynolds stress tensor, that appear after the averaging process and describe the turbulent contribution to the mean flow. In order to model them, eddy viscosity models are widely employed since they are easy to implement and computationally convenient. Nevertheless these models show difficulties to correctly predict flow phenomena like shock boundary layer interaction, which are of great interest for hypersonic flow. One of the limits of eddy viscosity models is that turbulence is modeled as an isotropic quantity. This hypothesis is not suitable for hypersonic flows where the strongly anisotropic flow phenomena, taking place in the boundary layer, have a great influence on the overall flow.

3.4 topographic data from Geographic Information System

The geographic information system retains topographical data inside. The geodatabase contain forest and town position, water resources, meteorological data, elevation of geography et al. In CFD simulation, terrain elevation detail can import from geodatabase to improve confidential of the simulation. Researcher import geography detail from GIS data to CFD simulations in experience.

Pual Stangroom [58] investigated capabilities of a RANS bases numerical model in accurately analyzing wind flow over real terrain region. The model performance is tested over a number of terrain types, flat terrain, an axisymmetric hill and a real terrain region. The grid data is available at 50 m intervals. The linear terrain data is only available at 50 m intervals at the time of modeled, though more accurate data is become available for large part in recently. Field survey data is available at 2 m contour levels, unfortunate as errors may be produced due to the lack of data, making it difficult to resolve whether errors are a result of the numerical model, or the lack of available data and other simplifications.

Atsushi Yamaguchi et al. [46] investigated wind flow over complex and steep terrain by a wind tunnel experiment and a numerical simulation. The topographic feature of the area is very complex with a steep cliff along the north-east coast. A 1:2000 scale terrain model which

covers an area of 8 km. In the manuscript, authors indicated results from the numerical simulations as the reference while wind tunnel experiments have been used in compared.

Ian P. Castro and David D. Apsley [53] described numerical prediction flow and dispersion over hill. comparison of predictions with experiment is made for adiabatic flow over 2D hills and stably-stratified flow over real terrain. The calculations were carried out on a variably-spaced 2D grid. Refinement tests confirmed satisfactory grid independence. The simulation with curvature modification and dissipation modification indicated similar results with experiment. Finally, comparison with wind-tunnel data for geographic information system imported hills demonstrate that this level of modelling is capable of predicting summit speed-up and terrain amplification factors provided the basic features of the flow are captured: lateral spread is, however, inevitably underestimated with an isotropic eddy-diffusivity model.

Geographic information system included various data in landscape contain elevations and profile of the hill. The resolution of terrain influent to results accuracy, 1:2000 of resolution is sufficiency for atmospheric boundary layers flow. However, roughness of terrain is lacking in geodatabase. The operator can establish the height of surface in numerical software.

CHAPTER 4

MATERIALS AND METHODS

4.1 Weather station

A weather station is a facility, either on land or sea, with instruments and equipment for observing atmospheric conditions to provide information for weather forecasts and to study the weather and climate. The atmosphere measurements taken include temperature, barometric pressure, humidity, wind speed and direction. Wind measurements are taken as free of other obstructions as possible, while temperature and humidity measurements are kept free from direct solar radiation, or insolation.

In this work, wind data are measured twice. Previously, wind data from 1st January 2008 to 31st December 2010 of Khong Chiam region representative for Ubonratchathani. The station measured wind speed and direction, temperature and air pressure to assess wind potential of Ubonratchathani. Afterward, the 10 m height of weather station were installed in a row to measure wind data from Pha Taem topography. The data used to compare with simulations in the case of geometry hill to generate potential site chart.

To measure wind data, many instrument have been installed into tower to collected data. The mechanism instrument are chooses by investigated the technical specification of the device. The whole instrument specifications of weather station are indicated in followed.

4.1.1 Cup anemometer

Cup anemometer is a common type of anemometer used in weather station. The three type cup anemometer has been used to measure wind speed. Gear box was used to convert speed of wind to be signal and recorded by data logger.

Table 4.1 Technical specifications of the KRIWAN INT10 anemometer

Specification	Details
Measuring range	0 – 40 m/s
Resolution	< 0.1 m/s
Accuracy	± 0.5 m/s
Start-up speed	< 0.4 m/s
Permitted ambient temperature	-40 to +70°C
Permitted relative humidity	0 - 100% r.h.

4.1.2 Wind vane

Wind vane is an instrument to measure direction of wind. Wind vane is a pointer that freely rotated on the top of a fixed vertical rod. It was designed to swing easily and point to the direction from which the wind was blowing. Results of wind direction have shown clockwise in degree as 0° - 360° from north.

Table 4.2 Technical specifications of the KRIWAN INT30 wind direction sensor

Specification	Details
Measuring range	0 - 360°
Resolution	< 1°
Accuracy	± 2.5°
Start-up speed	< 0.4 m/s
Permitted ambient temperature	-40 to +70°C
Permitted relative humidity	0 - 100% r.h.

4.1.3 Thermometer

Thermometer was used in weather station to measure temperature in degree Celsius unit. The thermometer stored in aluminum box to avoid moist, rain and direct solar radiation. Data from thermometer recorded hourly in data logger.

Table 4.3 Technical specifications of the temperature transmitter probe

Specification	Details
Measuring range	-30 to +70°C
Resolution	0.1°C
Accuracy	± 0.1°C
Current in the sensor	<1 mA
Sensitivity to variations of feeding voltage	0.01°C/°C

4.1.4 Barometer

Barometer is an instrument used in meteorology to measure atmospheric pressure. Barometer can record air pressure and altitude in the weather. Data from barometer recorded hourly in data logger.

Table 4.4 Technical specifications of the P-GE 8/11 digital barometer

Specification	Details
Measuring range	500 – 1100 hPa
Resolution	0.1 hPa
Accuracy	± 0.01 hPa
Operating temperature range	-40 to +60°C
Interval	1.0 s

4.1.5 Data logger

Measurement systems known as wind computers also carry out extensive statistical pre-evaluations. But in addition the time series of all measurement data will be registered. At regular intervals of 1 or 10 minutes the average and extreme readings as well as the standard deviations will be calculated and stored. This requires a much larger storage capacity of the data logger and the automatic data transmission to a computer, so that the measurement results can be processed with suitable wind energy software or with standard software for tabular calculations. Further evaluation needs more work (compared to the wind classifier) and more experience with data analysis. On the other hand the possibilities of evaluation are much greater.

Table 4.5 Technical specifications of the HIOKI 8421-51(32ch) data logger

Specification	Details
Input channels	Analog 32 channels
Thermocouple types	K, E, J, T, N, W (WRe5-26), R, S, and B
Platinum measurement resistance	types Pt 100, JPt 100, 3- and 4-line types
Analog voltage input	100 mV, 1 V, 10 V, 100 V
Recording interval	100 ms to 1 hour

4.1.6 Measuring site and heights

The ideal approach would be to measure the wind data at whole height or at the hub height of the wind power generation station that is been installed. Two arguments against this are that the exact hub height is most probably not yet known, since the final decision will be made on the basis of the measurement results, and secondly, that such as high measurement tower is very expensive and difficult to install.

The alternative is to use three anemometers to measure the wind speeds at 10 m, 30 m and 40 m heights. So the height profile on this location is determined (roughness length Z_0), which can be used to calculate the wind speed at other heights. Wind vane is located on top of the tower at 40 m height, while thermometer and barometer installed at 10 m height from ground and the data logger conserve in aluminum box with uninterruptible power supply (UPS) at eyesight level. The experimental setup of wind data measuring was shown in Figure 4.1.

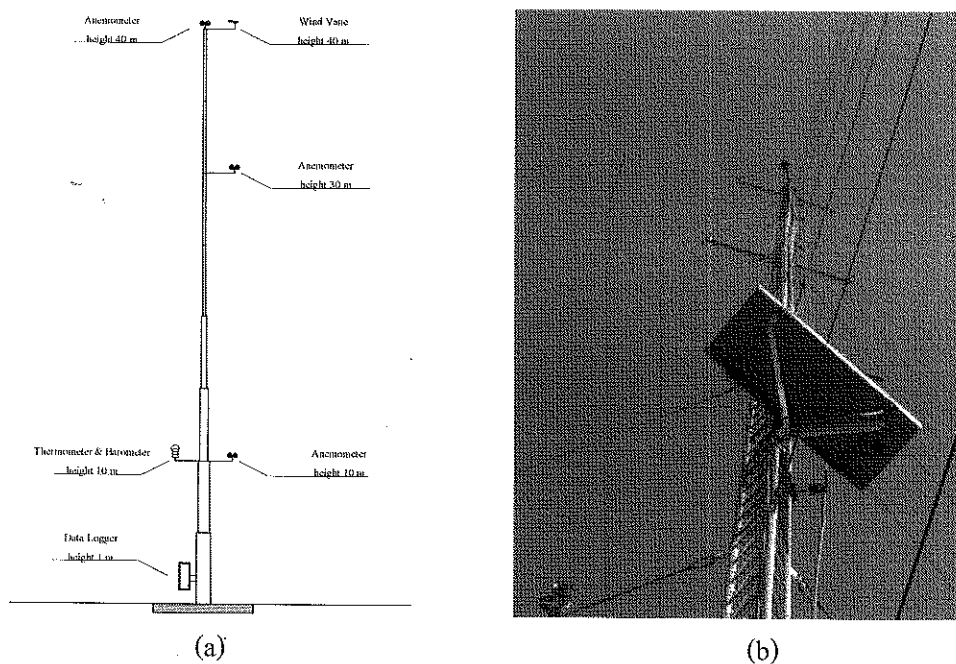


Figure 4.1 Experimental setup for meteorological measurement (a) diagram, (b) site

4.2 Measurement site

The wind data of Ubonratchathani region collected at the Khong Chiam meteorological station (latitude $15^{\circ}33' N$, longitude $105^{\circ}30' E$), from 1st January 2008 to 31st December 2010. The sampling period is 60 minutes and the altitude of the measurement point was 10 m, 30 m and 40 m above the ground. Wind speeds are frequently measured in integers so that each wind speed is measured many times during a year observations. The actual probability density function, are calculated using the relationship $f_i = n_i/N$, where N is the total number of wind data obtained in a specific month and n_i is the frequency of a particular wind speed value.

The second site measured in this work located at Pha Taem national park. Wind speed at 10 m height are collected every 10 second for 15 minutes. Seven stations installed in longitudinal of flow direction, two stations located front of hill top while five stations located at hilltop and afterward. Wind speed data from this session have been used to be reference in the simulations.

4.3 Wind potential calculation

The stage in process of wind power potential of Ubonratchathani region can calculate follow Figure 4.2.

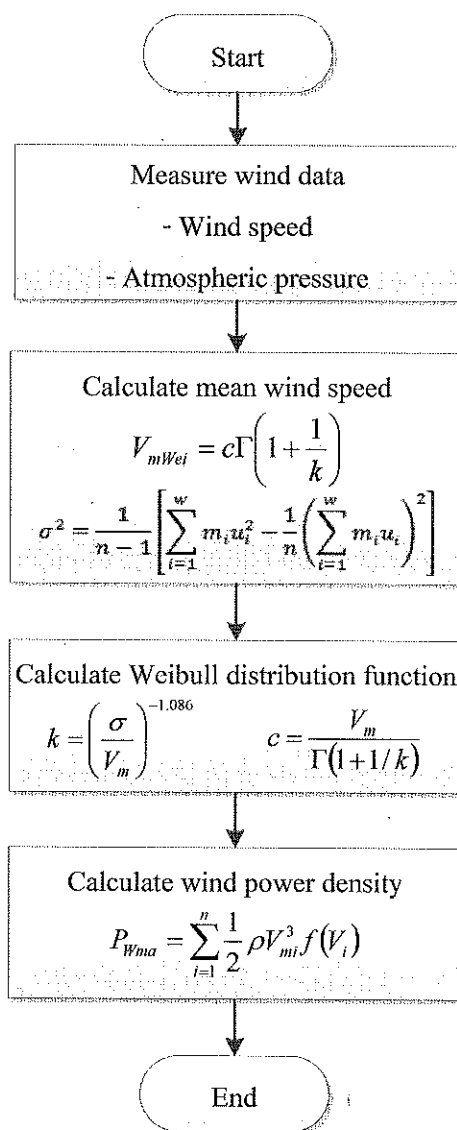
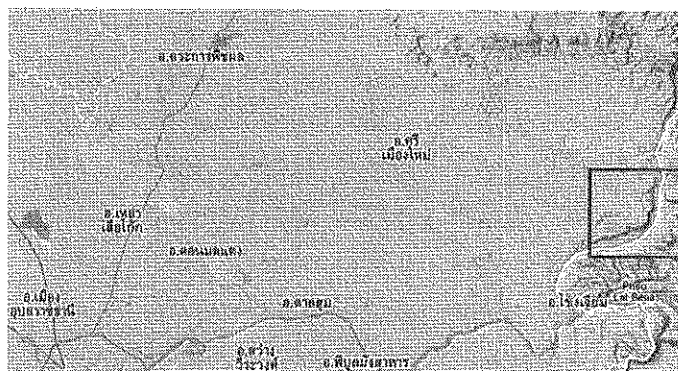


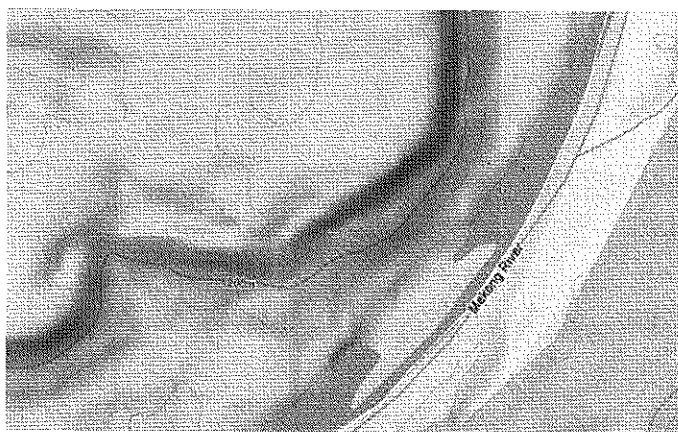
Figure 4.2 Flowchart of wind power calculation

4.4 Terrain model

Pha Taem national park is located at the eastern of Ubonratchathani district near the Mekong river. Figure 4.3 and 4.4 indicated the hill top is 240 m from ground and steep of the hill is 20.06° . The terrain behind the hill top is a 1.66° rockbound slope with few obstacles, while front of the hill are farmland and river. The hill structure is located perpendicular with wind impact direction.



(a)



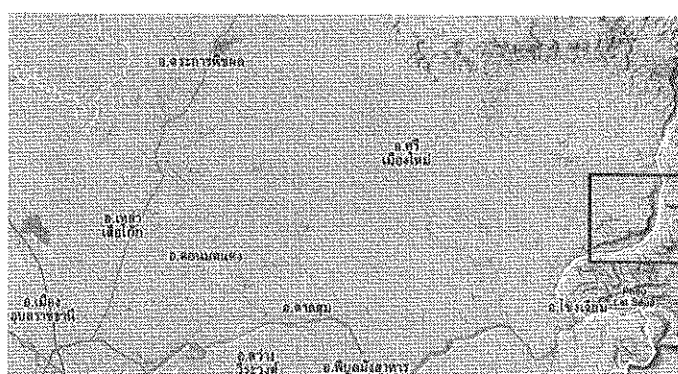
(b)

Figure 4.3 Location and contours of Pha Taem hill

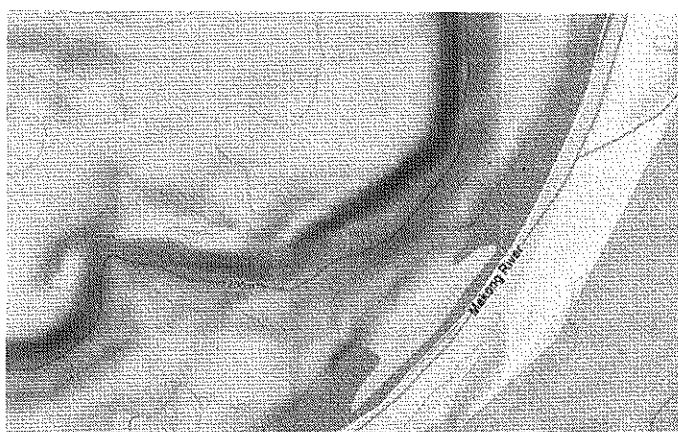
(a) location of Pha Taem hill (b) Contour of Pha Taem

4.4 Terrain model

Pha Taem national park is located at the eastern of Ubonratchathani district near the Mekong river. Figure 4.3 and 4.4 indicated the hill top is 240 m from ground and steep of the hill is 20.06° . The terrain behind the hill top is a 1.66° rockbound slope with few obstacles, while front of the hill are farmland and river. The hill structure is located perpendicular with wind impact direction.



(a)



(b)

Figure 4.3 Location and contours of Pha Taem hill

(a) location of Pha Taem hill (b) Contour of Pha Taem

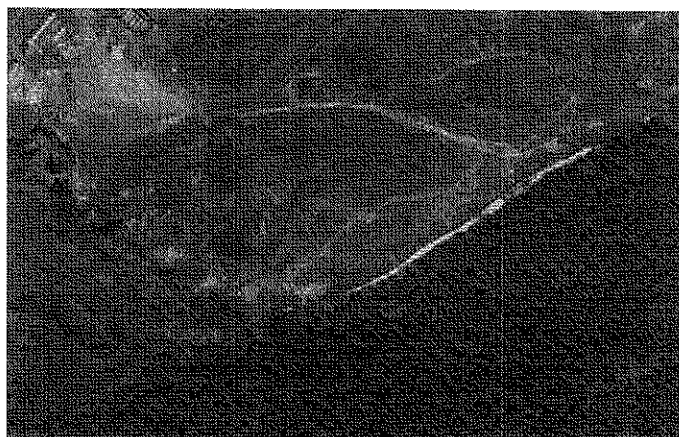


Figure 4.4 Pha Taem terrain topography

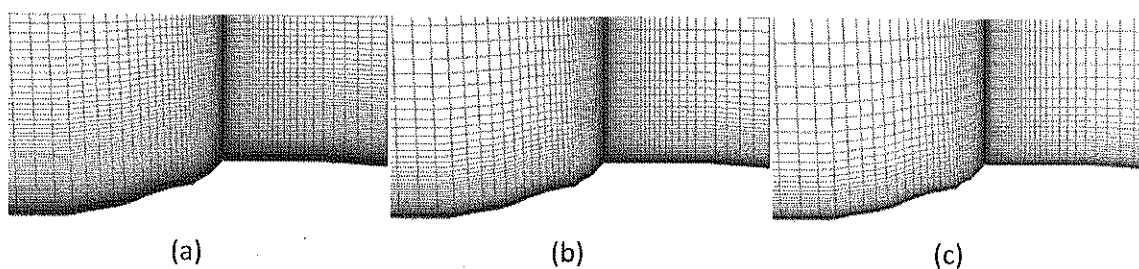
4.5 Grid dependence

An optimal grid is chosen, the model should be able to accurately describe the flow field at a low computational cost. To achieve this, the boundaries of the simulation domain are located in an optimal way to let the inflow and outflow boundary have a minor effect on the flow field around the hill and the recirculation zone. At both the inflow and the outflow boundary, the flow is assumed not to have gradients in the flow direction (x). This is not physical, but the boundaries should be placed far enough from the hill that the error is negligible. Errors caused by flow oscillations in space at inflow, should also be damped to not influence the flow in the hill vicinity. This is also taken into account in the reference simulation, and to be able to compare the results with the reference solution, a natural choice is to use the same domain.

Three different grids described in Table 4.6 and visualized in Figure 4.5 are used to test the grid dependence. To investigate the grid arrangements in this work, the first grid cell enlargement are examined. The three grid cell size domain called coarse, medium and fine with increasing rate of 8%, 10% and 12% have been analyzed. The similar initial and boundary conditions have been applied in this analysis.

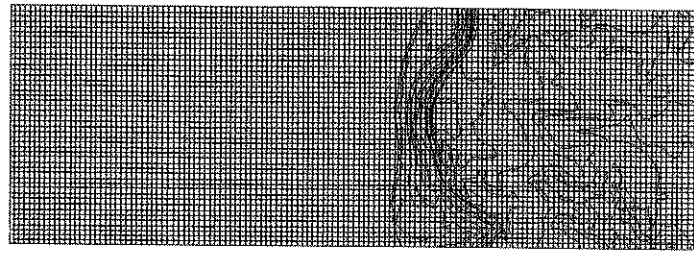
Table 4.6 Essential sizes of the grid dependence test

Properties	Coarse	Medium	Fine
Dimension	2,000×1,000	2,000×1,000	2,000×1,000
First grid cell size (m)	0.25493	0.04181	0.00709
Increasing rate	8%	10%	12%
Largest cell size (m)	70.20	85.64	96.59

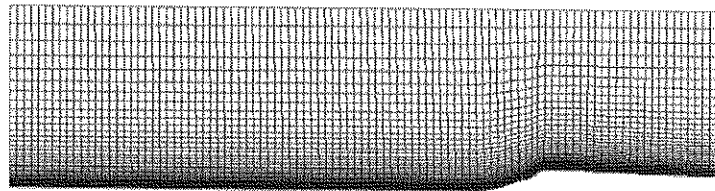
**Figure 4.5** Grid visualization of terrain coding (a) Coarse, (b) Medium, (c) Fine

In the fine grid, the first grid cell is larger than the other, in order to ensure that the first cell center is inside the logarithmic layer for all wall cells. The smallest cells are on the top of the hill, but the velocities are larger here causing the friction velocity to become larger. The grid cell for the coarse, medium and fine have enlarged. The heights of first grid cells of the domain are 0.25493 m, 0.04181 m and 0.00709 m, respectively.

The grid used in the simulations highly influences the results. Both the grid resolution and accuracy of the terrain data are important. The simulation domain is chosen to include the neighboring hills behind the Pha Taem hill, and the grid used in the simulations has a horizontal extension from 1 km in front of the hilltop, to 1 km behind the hilltop. The width of the domain is about 1 km, and the height of the domain is 1 km. The horizontal and vertical distribution of the grid cells is visualized in Figure 4.6(a) and 4.6(b), respectively. The resolution in horizontal direction are $\Delta x = 1.0$ m and $\Delta y = 1.0$ m. The vertical grid distribution, the first grid cell is $\Delta z = 0.00709$ m with a vertical stretching of 12%, the largest vertical extension is 96.59 m.



(a)



(b)

Figure 4.6 Distribution of grids cells used in the simulations coding

(a) Horizontal distribution, (b) Vertical distribution

4.6 Initial and boundary conditions

A one-dimensional simulation is done to establish a profile over homogeneous conditions. With the roughness length $z_0 = 0.04$ m, the simulated velocity at inlet flow of the domain is 3.014 m/s. This profile is used as whole inflow boundary and initial conditions for the entire domain. At the side boundaries there are periodic boundary conditions, and at the outflow boundary there is a zero-gradient condition. The surface boundary condition is expressed by wall functions, connecting the velocity in the first cell to the roughness and the log law assumption. The top boundary is as a zero-gradient surface in all variables except the vertical velocity, which is defined not to allow any material transports through the boundary. This means a vertical velocity equal to zero at the top boundary. The initial conditions and boundary conditions of the simulations illustrated in Table 4.7.

Table 4.7 Initial and boundary conditions of the simulations

Parameters	Type
Solver	Segregated
Formulation	Implicit
Space	3D
Time	Unsteady
Velocity Formulation	Absolute
Unsteady Formulation	1 st Order Implicit
Turbulent Model	- Standard k- ϵ model - Standard k- ω model - Reynolds Stress Model
Near Wall Treatment	Enhance Wall Treatment
Model Constant	$C_\mu, C_{\epsilon 1}, C_{\epsilon 2}, \sigma_k, \sigma_\epsilon$
Air Density	1.225 kg/m ³
Time Step	0.1 second
Max Iteration / Time Step	2000

4.7 Processing

The processing of the CFD computation is done in single on a standard PC with two core duo CPU with 2.00 GHz and 8 GB of RAM. A computation for full of the domain without computation of the free surface take about 9 hours with a mesh of about 15 million of cells. Usually the computations are performed in model scale in order to reduce the number of cells in the mesh and the computational effort. Thus, the results of the computation can directly be compared with towing tank measurements.

4.8 Generate wind turbine suitable site chart

4.8.1 Hill angle dependence

The hill model depend on front hill angle was duplicates from 5° to 45° vary on 5° rising. Another initial and boundary conditions of model were unchanged. To maintain the hill angle and height, distance in front of the hill will be validated. Figure 4.7 shown distance of front hill rising vary on front hill angle.

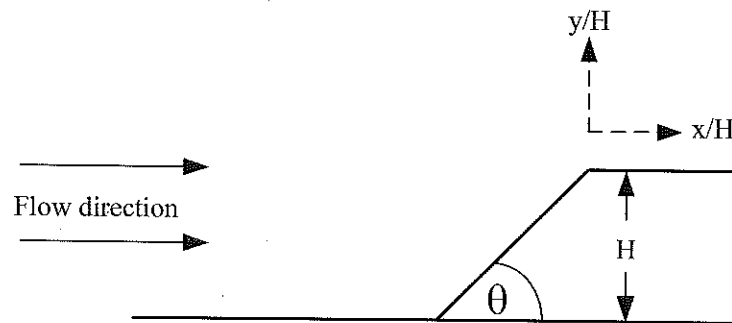


Figure 4.7 Hill angle distance structure and variable

The grid used in the simulations has horizontal and vertical arrangements similar with Pha Taem hill model. The horizontal domains of simulations were from 1 km in front of the hill top, to 1 km behind the hilltop. The width of the domain is 1 km, and the height of the domain is 1 km.

4.8.2 Wind speed dependence

Commercial wind turbines have working range from start-up wind speed 3 m/s to cut-off speed which emergency stop system will be working at about 40 m/s. To create the chart in whole range, background wind speeds from 2 m/s to 40 m/s are considered to create the chart. Step of 2 m/s are considered in this work.

4.8.3 Roughness dependence

An important parameter of wind is the variation of vertical wind speed. This variation of wind speed is called vertical wind shear which express to canopy height. The obstacles in surrounding such as tree, bush, farmland or grass have difference height as shown

in Table 4.8. This work adjusts roughness heights from 0.0001 m – 0.1 m in the simulations to generated the chart.

4.8.4 Chart generation

Investigation of potential site of wind turbine hub depends on hill angle, wind speed and roughness surface are observed. Trend line of suitable position from the simulation are created for extend the chart. Extrapolation technique of the boundary have been used to determine for expand the charts. Series of linear charts are provided in sequences of canopy height.

Extrapolation is the process of constructing new data points. It is similar to the process of extrapolation, which constructs new points between known points, but the results of extrapolations are often less meaningful, and are subject to greater uncertainty. It may also mean extension of a method, assuming similar methods will be applicable.

Extrapolation means creating a tangent line at the end of the known data and extending it beyond as that limit. Linear extrapolation will only provide good results when used to extend the graph of an approximately linear function or not too far beyond the known data.

Table 4.8 Typical canopy height in surrounding

Land Cover Types	Typical Roughness Length (m)
Urban and suburban areas	0.4-0.55
Small towns	0.55
Outskirts of towns	0.40
Woodlands and forest	0.4-1.2
Farmland and grassy plains	0.025-0.30
Many trees and hedges, a few buildings	0.30
Scattered trees and hedges	0.15
Few trees (summer)	0.055
Crops and tall grass	0.050
Isolated trees	0.025
Large expanses of water	0.0001-0.001

CHAPTER 5

RESULTS AND DISCUSSIONS

5.1 Wind energy potential assessment

5.1.1 Wind data collections

The wind data collected from Khong Chiam meteorological station (latitude $15^{\circ}33'$ N, longitude $105^{\circ}30'$ E), which is located in Ubonratchathani province, from 1st January 2008 to 31st December 2010. The sampling period is 60 minutes and the altitude of the measurement point was 10 m, 30 m and 40 m above the ground and frequency of the wind speeds illustrated in Appendix A.

5.1.2 Monthly wind speed variations

The determination of the mean monthly wind speed of the selected site showed wind characteristics. The maximum mean monthly wind speed recorded in January with the mean wind speed reaching 2.90 m/s and the windiest month is September with the mean wind speed approximately 1.83 m/s. Mean monthly wind speed data varying at height 10 m, 30 m and 40 m height are shown in Figures 5.1 – 5.3.

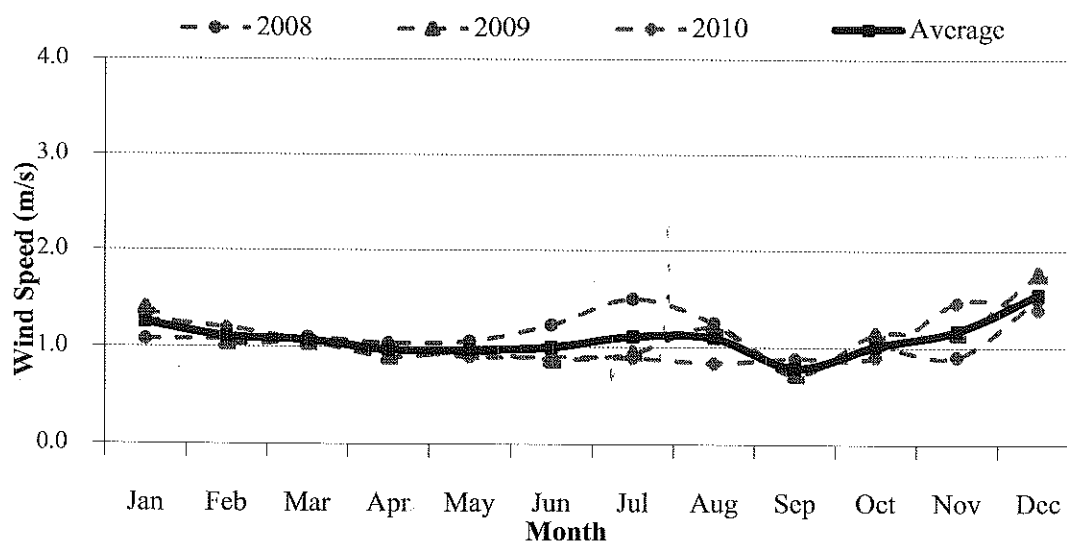


Figure 5.1 Mean monthly wind speed data at 10 m height

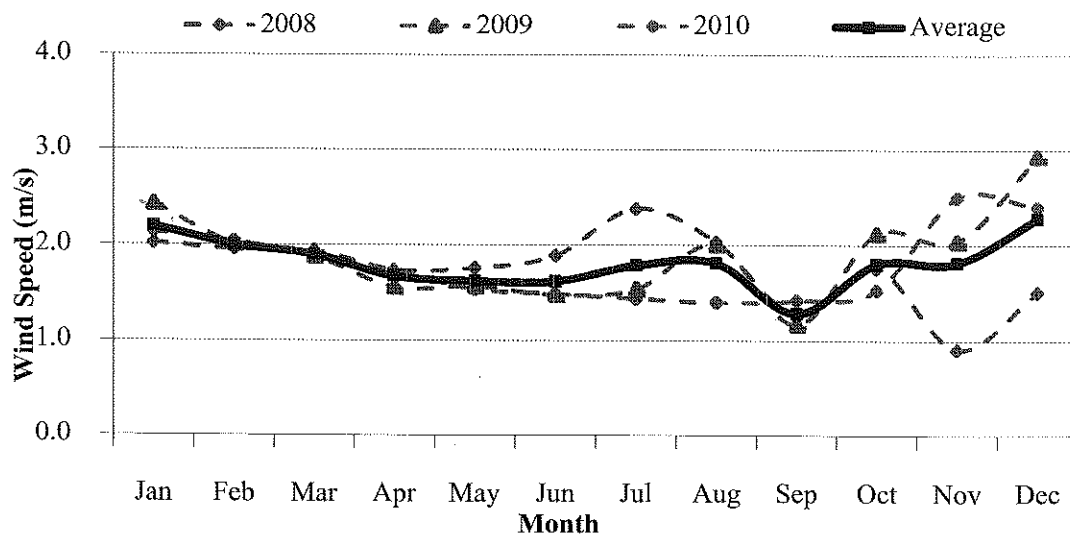


Figure 5.2 Mean monthly wind speed data at 30 m height

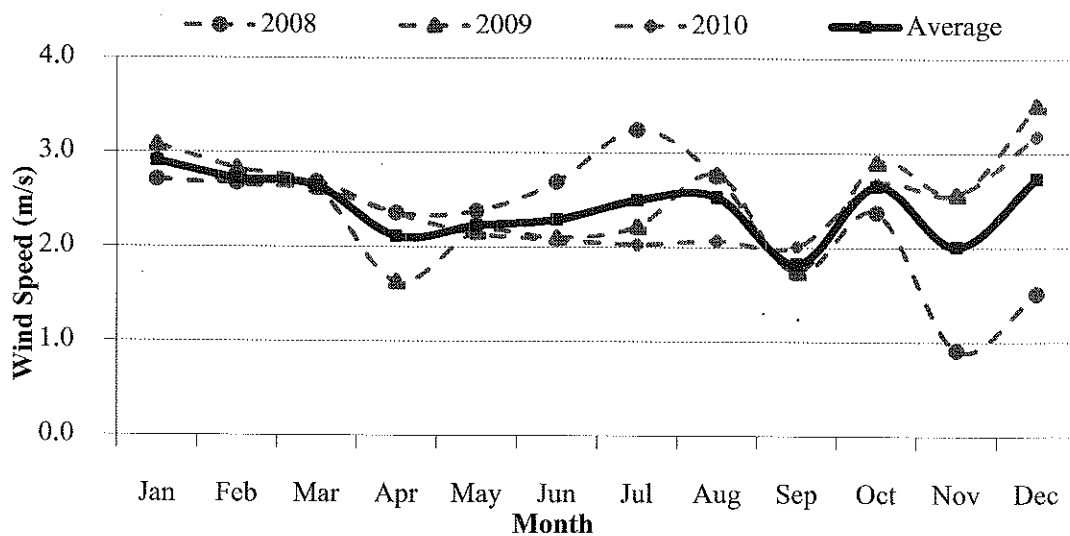


Figure 5.3 Mean monthly wind speed data at 40 m height

The monthly wind speed data indicated maximum in December which in winter, while minimum showed in September which in rainy season. In winter, the monsoon or typhoon prevail lies across the Northeastern from South China Sea. Therefore, Ubonratchathani region adopt wind dynamistic into the opposite of Pha Taem hill. In rainy season, height atmospheric pressure and moistness construct less difference temperature in nearby region. The heavier air

maintained in ground level or slowly leaving, wind flow from neighboring must be gradually entering. This cause minimum mean wind speed indicated in September.

The mean monthly wind speed has been recorded maximum value in December in 2009 and 2010 while year 2008 is found in July. This cause effect of tropical storm BILIS with maximum speed at 93 km/hr have been blow over Ubonratchathani region.

5.1.3 Diurnal wind speed variations

Another interesting outcome of the analysis of the mean wind speed is diurnal variation. As shown in Figure 5.4, the diurnal variation increased in daytime and significant in nighttime. The wind speeds start to increase slightly in the early morning at 6:00 and start to decrease early afternoon from 13:00 to 5:00. This may be explained by the temperature stratification. An argument that may be used to explain the diurnal variation, for the daytime, assuming constant horizontal pressure force, is the variation in atmospheric stability, which in turn affects the vertical exchange in momentum. Vertical exchange in momentum which would be most pronounced during early morning because of thermal convection, would result in an increase of wind speed. At nighttime the vertical exchange in momentum is less.

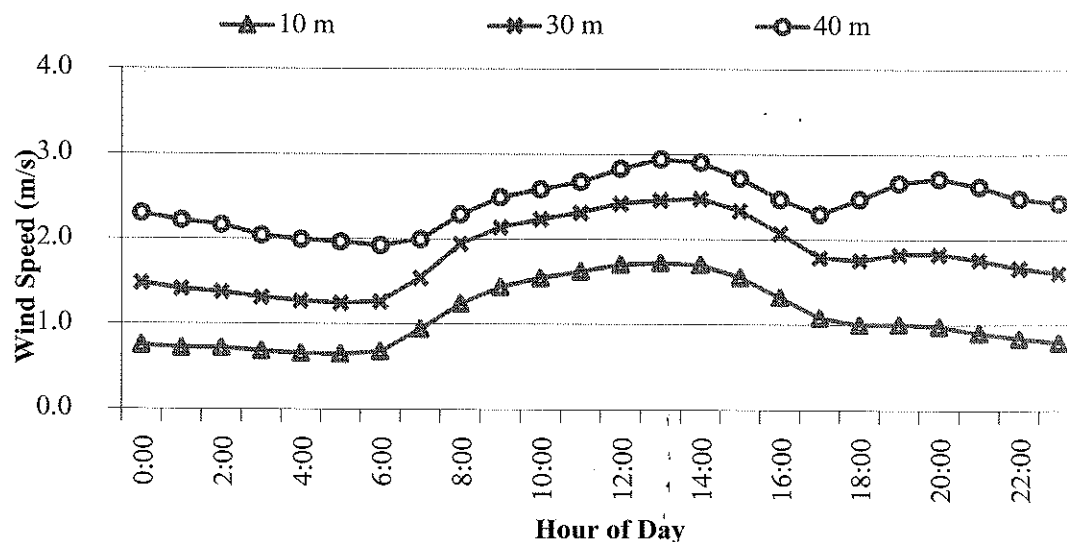


Figure 5.4 Diurnal mean wind speeds variation

The wind speed is raising and become lower twice in diurnal. It is caused by the heating of the earth's surface by the sun. From 6:00 to 13:00 the mean wind speeds regularly

increases and reduce after that until 17:00. Since, the ground absorbs the sun radiation and creates daily wind cycle in daytime. The second circle of the wind speed increase start from 17:00 to 20:00 and decrease afterward until 6:00.

In subdivision of the year, weather are changed refer to position and distance of earth on the sun. Atmospheric character is differing in each season, mean wind speed is average in summer, wind flows in rainy season are still or least mean wind speed and maximum of the flow appear in winter.

5.1.4 Wind data processing

Wind data for Ubonratchathani for 3 years from 2008 to 2010 have been statistically analyzed. Table 5.1 – 5.3 shows, respectively, the wind data processing for Ubonratchathani for years 2008–2010 for a height of 10 m, 30 m and 40 m. The average wind speed V_m for each month is calculated as follows

$$V_m = \frac{1}{N} \left[\sum_{i=1}^N V_i \right] \quad (5.1)$$

where, N is the number of records for each month. The standard deviation σ is also calculated for each month using

$$\sigma = \sqrt{\frac{1}{N-1} \sum_{i=1}^N (V_i - V_m)^2} \quad (5.2)$$

Following the procedure presented in previous section and Weibull parameters (k and c) are determined using both approaches.

It can be seen from Tables 5.1 – 5.3 that the highest wind speed occurs in November while the lowest wind speed occurs in May at all heights studied. The smallest standard deviation σ is found to be in May. This indicates that the wind speed records are close to the average wind speed. The average annual wind speed is found to be 2.12 m/s for 10 m height, 2.87 m/s for 30 m height and 3.53 m/s for 40 m height.

Table 5.1 Weibull parameters calculated using approximated method at 10 m height

Month	Average wind speed V_m (m/s)	Standard deviation σ (m/s)	Weibull approximated	
			Parameter k	Parameter c
January	1.250	1.111	1.137	1.209
February	1.110	0.840	1.353	1.111
March	1.070	0.826	1.325	1.063
April	0.970	0.740	1.342	0.957
May	0.970	0.772	1.281	0.947
June	1.000	0.803	1.269	0.977
July	1.110	0.936	1.203	1.081
August	1.100	0.947	1.177	1.063
September	0.790	0.566	1.436	0.770
October	1.020	0.916	1.124	0.964
November	1.180	1.123	1.055	1.105
December	1.560	1.367	1.154	1.541
Annual	1.094	0.912	1.238	1.066

Table 5.2 Weibull parameters calculated using approximated method at 30 m height

Month	Average wind speed V_m (m/s)	Standard deviation σ (m/s)	Weibull approximated	
			Parameter k	Parameter c
January	2.20	1.606	1.407	2.116
February	2.01	1.319	1.581	1.939
March	1.50	1.296	1.172	1.285
April	1.67	1.211	1.418	1.536
May	1.62	1.203	1.381	1.474
June	1.62	1.199	1.387	1.475
July	1.79	1.327	1.384	1.660
August	1.81	1.407	1.315	1.664
September	1.29	1.032	1.275	1.091
October	1.80	1.480	1.237	1.628
November	1.82	1.750	1.044	1.551
December	2.28	1.807	1.287	2.164
Annual	1.784	1.386	1.324	1.632

Table 5.3 Weibull parameters calculated using approximated method at 40 m height

Month	Average wind speed V_m (m/s)	Standard deviation σ (m/s)	Weibull approximated	
			Parameter k	Parameter c
January	2.910	1.761	1.726	2.865
February	2.720	1.520	1.882	2.664
March	2.640	1.495	1.854	2.573
April	2.310	1.409	1.711	2.190
May	2.230	1.404	1.652	2.094
June	2.290	1.410	1.693	2.166
July	2.500	1.541	1.691	2.401
August	2.530	1.606	1.638	2.428
September	1.830	1.313	1.434	1.615
October	2.460	1.733	1.463	2.316
November	2.190	2.005	1.101	1.870
December	2.730	2.000	1.402	2.596
Annual	2.445	1.600	1.604	2.315

It can be seen from Table 5.1 – 5.3 that the highest wind speed occurs in November while the lowest wind speed occurs in September at all height studies. The smallest standard variation is found to be in September. This is indicated that the wind speed records are closed to average wind speed. The small shape factor k indicated wind data distribution of speed near maximum velocity which whole are in agreement value while scalar factor c indicated how windy of wind in records. Therefore, the calculation details of Weibull parameters are illustrated in Appendix B.

Figures 5.5 – 5.7 shows the actual probability density function, Weibull probability distribution function from approximated method for all height under consideration. These functions used in the coming section to predicate the average wind speed and average wind power corresponding to each height.

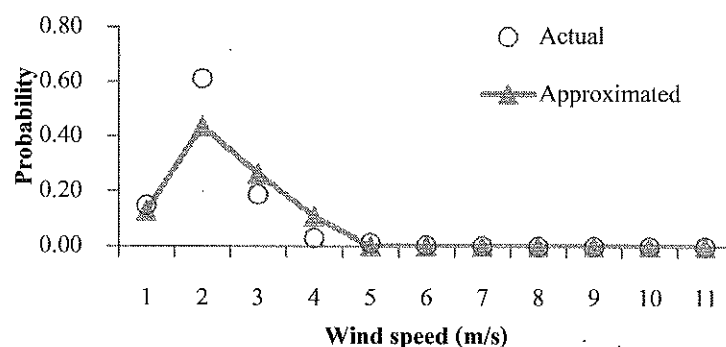


Figure 5.5 Probability density function of wind speeds at 10 m height

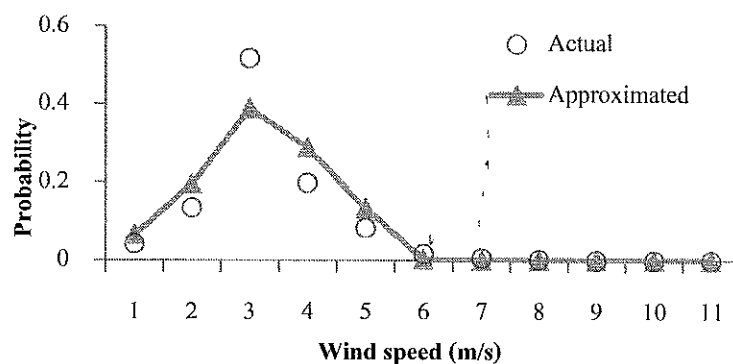


Figure 5.6 Probability density function of wind speeds at 30 m height

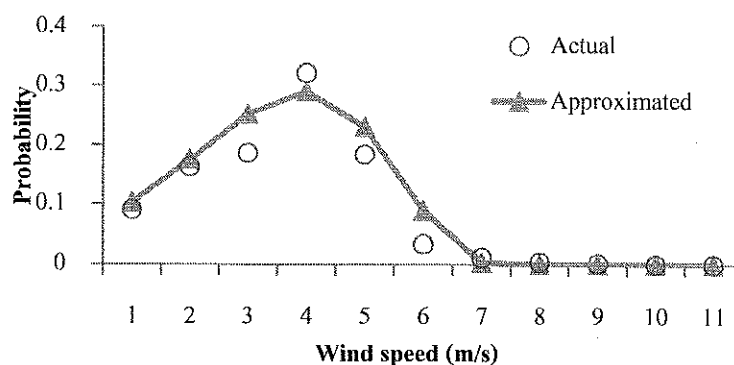


Figure 5.7 Probability density function of wind speeds at 40 m height

The Weibull distributions signify the wind regime in the region and are the most appropriate parameters for the measured frequency distribution. The Weibull distribution and its special case have been used to study the wind data. The use of this frequency distribution approach can provide a simple method to predict the energy output of a wind energy conversion system.

5.1.5 Estimation of average monthly wind speed and power density

The average monthly wind speed and average monthly power density at 10 m, 30 m and 40 m heights estimated from actual probability density function, Weibull probability distribution function using approximated method are presented in Table 5.4 -5.6. The last row of each table shows the annual average wind speed and annual wind power density. The maximum power density throughout the year is found in November and the lowest power densities occur in May. The Weibull distributions, using both approaches predicts the maximum and the minimum power densities at the right month. Thus, the Weibull distribution, calculated using approximated approach, is accurately presenting the wind speed variation in Ubonratchathani.

Table 5.4 Monthly wind speed and power density calculated using Weibull parameters for years 2008–2010 in Ubomratchathani at a height of 10 m

Month	V_m (m/s)	Measurement			Weibull approximated		
		P/A (W/m ²)	E/A (kWh/m ² /month)	P/A (W/m ²)	E/A (kWh/m ² /month)		
January	1.250	1.34	0.33	1.16	0.28		
February	1.110	0.84	0.18	0.78	0.17		
March	1.070	0.73	0.13	0.66	0.12		
April	0.970	0.51	0.07	0.45	0.06		
May	0.970	0.52	0.07	0.45	0.06		
June	1.000	0.59	0.09	0.51	0.08		
July	1.110	0.87	0.17	0.75	0.15		
August	1.100	0.83	0.16	0.71	0.13		
September	0.790	0.32	0.02	0.27	0.02		
October	1.020	0.68	0.10	0.55	0.08		
November	1.180	1.12	0.31	0.90	0.25		
December	1.560	2.64	0.94	2.42	0.86		
Annual	1.094	11.00	2.57	9.61	2.26		

Table 5.5 Monthly wind speed and power density calculated using Weibull parameters for years 2008–2010 in Ubonratchathani at a height of 30 m

Month	V_m (m/s)	Measurement			Weibull approximated		
		P/A (W/m ²)	E/A (kWh/m ² /month)	P/A (W/m ²)	E/A (kWh/m ² /month)	P/A (W/m ²)	E/A (kWh/m ² /month)
January	2.20	7.31	3.07	5.93	2.49		
February	2.01	5.01	2.07	4.04	1.67		
March	1.50	2.02	0.73	1.20	0.44		
April	1.67	2.63	0.77	1.86	0.54		
May	1.62	2.44	0.89	1.68	0.61		
June	1.62	2.50	0.89	1.72	0.61		
July	1.79	3.64	1.49	2.65	1.09		
August	1.81	3.70	1.49	2.65	1.07		
September	1.29	1.37	0.35	0.77	0.19		
October	1.80	3.73	1.51	2.58	1.05		
November	1.82	4.13	1.65	2.51	1.00		
December	2.28	8.24	4.25	6.52	3.36		
Annual	1.784	46.72	19.16	34.10	14.12		

Table 5.6 Monthly wind speed and power density calculated using Weibull parameters for years 2008–2010 in Ubonratchathani at a height of 40 m

Month	V_m (m/s)	Measurement			Weibull approximated		
		P/A (W/m ²)	E/A (kWh/m ² /month)	P/A (W/m ²)	E/A (kWh/m ² /month)		
January	2.910	16.93	11.88	14.39	10.11		
February	2.720	12.42	8.53	10.36	7.12		
March	2.640	11.01	7.44	9.04	6.11		
April	2.310	6.95	4.16	5.28	3.16		
May	2.230	6.37	3.66	4.72	2.71		
June	2.290	7.06	4.21	5.33	3.18		
July	2.500	9.92	6.17	7.84	4.88		
August	2.530	10.10	6.39	7.98	5.05		
September	1.830	3.92	1.71	2.45	1.07		
October	2.460	9.52	5.54	7.20	4.19		
November	2.190	7.19	2.95	4.32	1.77		
December	2.730	14.14	8.47	11.08	6.63		
Annual	2.445	115.52	71.10	90.00	55.97		

A comparison of the monthly mean wind speeds and mean wind power density is shown in Table 5.4 – 5.6. It is clear that Weibull approximation methods changing wind power density trend. However, the rate of change is different as a small variation in the wind speed can cause larger wind power density predictions due to the fact that the wind power density is proportional to the cube of the wind speed. This effect is more pronounced at higher wind speed conditions.

To conclude the analysis of the collected data, it became apparent that for the purpose of mapping the variation of the wind potential of Ubonratchathani region, it was better to choose the wind power density since it incorporated not only the distribution of wind speeds, but also the dependence of the power density on air density and on the cube of the wind speed.

5.1.6 Wind direction

Determining wind speed according to wind direction is important to conduct wind energy researches and displays the impact of geographical features on the wind. The wind direction is illustrated in polar diagrams and is measured clockwise in degrees. The cycle (360°) which divided in 16 sectors and each of them covers an arc of 22.5° . The frequencies are plotted in polar diagrams with the wind blows. The duration of the stillness as a fraction of time is presented with a specific cycle of appropriate radius at the center of each polar diagram. In Figure 5.8, the wind data and the polar diagrams of Ubonratchathani for the years 2008–2010 are presented.

A comparison of the polar diagrams for the years studied, shows that the direction of wind blow in Ubonratchathani is characterized by a significant stability. The most probable wind direction for the three years period is on 157.5° in the three-quarter, which on the south-east. On the other hand, for all the years the stillness percentage is in the range of 15–48 %.

The prevailing directions indicated were south, south-southeastern and southeastern. It should be mentioned that the percentage of energy depicted in the wind direction corresponds to the distribution of the available wind energy and not that delivered by a potentially installed wind turbine. Although, the difference is relatively small, it is mainly associated with the cases where the wind speed from a particular direction is larger than the turbine's cut-out speed.

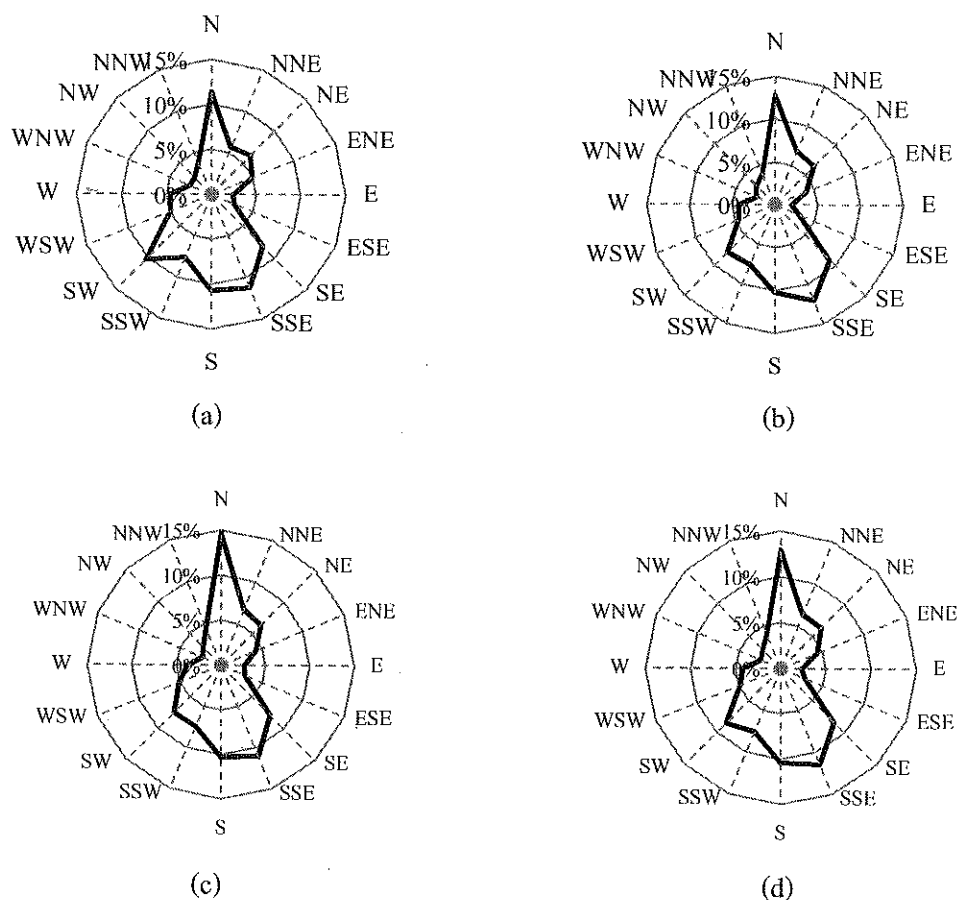


Figure 5.8 Polar diagram of wind direction for the year 2008-2010 in Ubonratchathani

(a) 2008, (b) 2009, (c) 2010, (d) whole year

Finally, the calms have not been considered as it is believed that during the calms the direction recorded by the wind vanes was not necessarily representative. The percentage of calm conditions, where the wind speed is less than or equal to 2.0 m/s is significantly. It is apparent that the high percentage of calm conditions is found in September and November.

Conclusively, the outcomes of the analysis of the wind direction are presented in Table 5.4 – 5.6, in which the prevailing wind directions and the corresponding percentages of time and available wind energy for each month studied are included.

When comparing direction of the flow becomes obvious that the best wind sector based on time did not necessarily coincide with the best sector based on the available wind energy.

This remark was not unexpected when considering that although wind might be blowing from one direction for a relatively long period, the corresponding speeds recorded might not be high.

5.2 Grid dependence

The results of this analysis showed small differences between the grids as shown in Figure 5.9. However, the results are found to differ significantly from the reference solution. This was surprising since preliminary results coincided well with the reference solution. The solution is dependent on the thickness of the first cell. To test first cell thickness sensitivity, simulations were performed with the medium grid, without thickness enlargement. This gave a very different flow pattern compared to the simulation with the enlarged first grid cell. The Figure 5.9 showed the separation point sensitivity to the thickness of the first cell is huge.

Generally, the medium grid gave almost the same result as the fine grid, but the extra computational effort of the fine grid was considerable. The coarse grid lost some details, and the separation and the reattachment point had a larger grid dependency.

The sensitivity is found to be particular strong for the indirect wall function approach. In this approach, the results without enlarged thickness of the first cell are almost identical to the reference $k-\epsilon$ simulation. On the other hand the simulation with the enlarged first cell differs considerably from the reference $k-\epsilon$ simulation. The recirculation zone is shorter and thinner. This is mainly caused by changed separation point. Before separation, the results are almost identical.

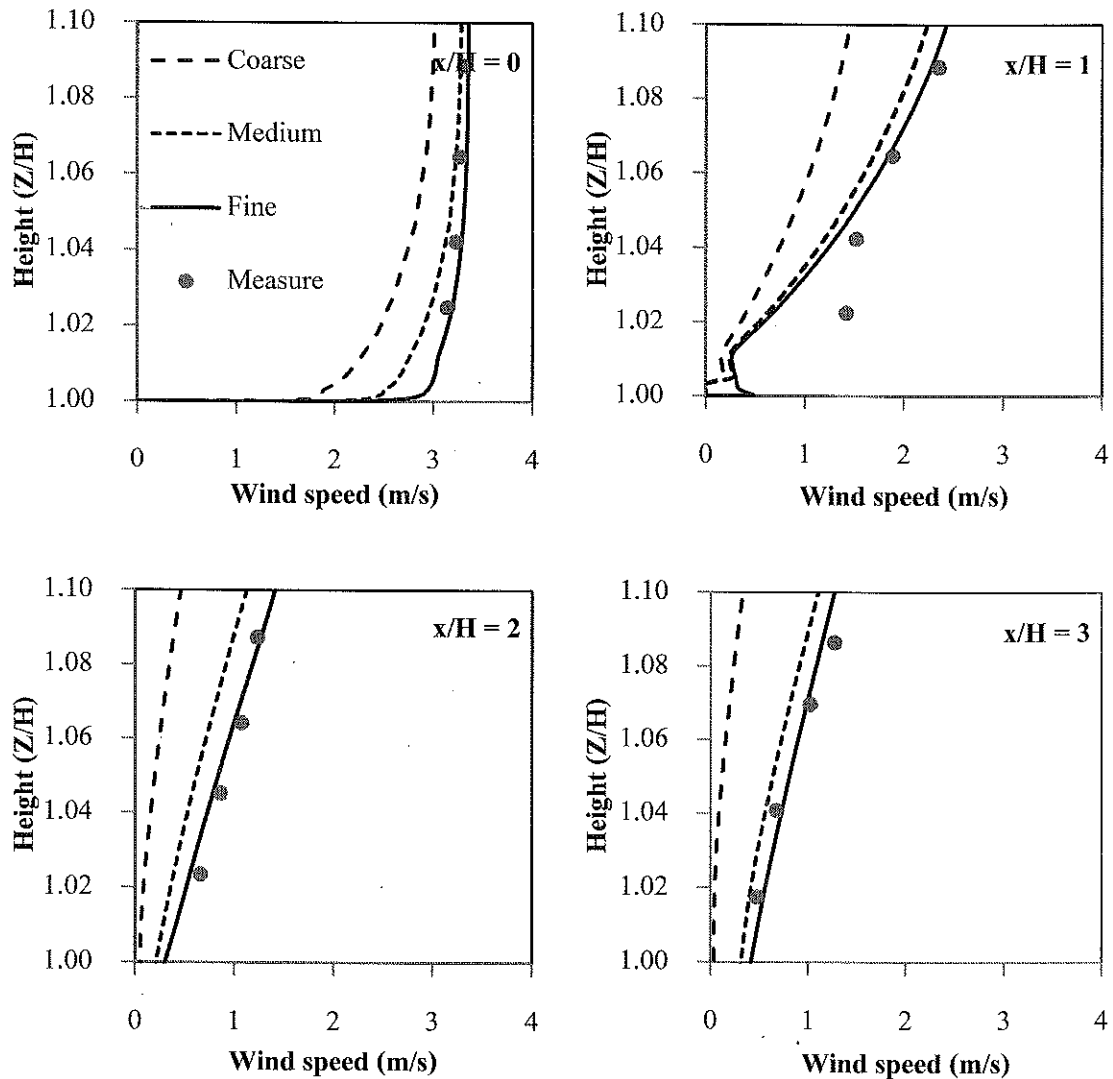


Figure 5.9 Grid resolution sensitivity

5.3 Simulation results of Pha Taem hill

5.3.1 velocity profile at reference station

Figure 5.10 indicated comparison of wind profile at reference station from standard $k-\epsilon$ model, standard $k-\omega$ model, RSM and measurements at the vertical velocity along $x/H = -1.0$. The simulations and measurements were compared at 5 m, 10 m, 15 m and 20 m height. The result from standard $k-\epsilon$ model was related with the measures while standard $k-\omega$ model and RSM was dissimilar. The standard $k-\epsilon$ model has been shown to be useful for free-shear layer flows with relatively small pressure gradients. Similarly, for wall-bounded and internal

flows, the model gives good results only in cases where mean pressure gradients are small; accuracy has been shown experimentally to be reduced for flows containing large adverse pressure gradients.

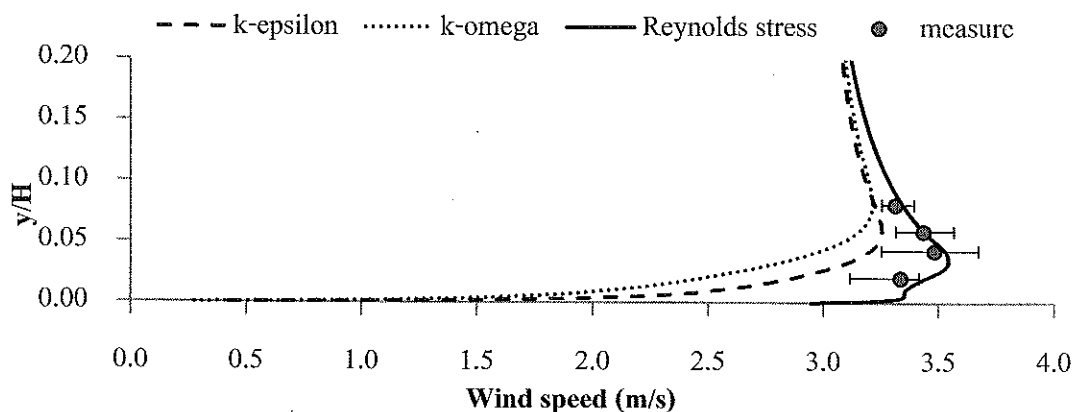


Figure 5.10 The velocity profile at reference station of difference models

From the overview results seen in Figures 5.10, it is seen that the modelling results are generally close to both the experimental results at the reference station. Both models with RSM and standard k- ω are different with reference solution of the measured. In the streamline plot, the only method that is significantly followed is the standard k- ϵ model.

The result in Figure 5.10 shows that it is difficult to really distinguish between the different models and watch local effects. The near wall flow at the hill summit from ground to 0.02 y/H heights has recirculation flow, as well as the reconstruction of the boundary layer is magnified.

5.3.2 Comparison of velocity

The increased velocity profiles indicated RSM result is similar with the measurements while k- ϵ model and k- ω model showed dissimilar. Figure 5.11 indicate most increased velocity of RSM, k- ϵ model and k- ω model occurred 18.089%, 8.523% and 7.179% respectively. The maximum velocity in simulation appeared at y/H are 0.03465 m, 0.05882 m and 0.08076 m.

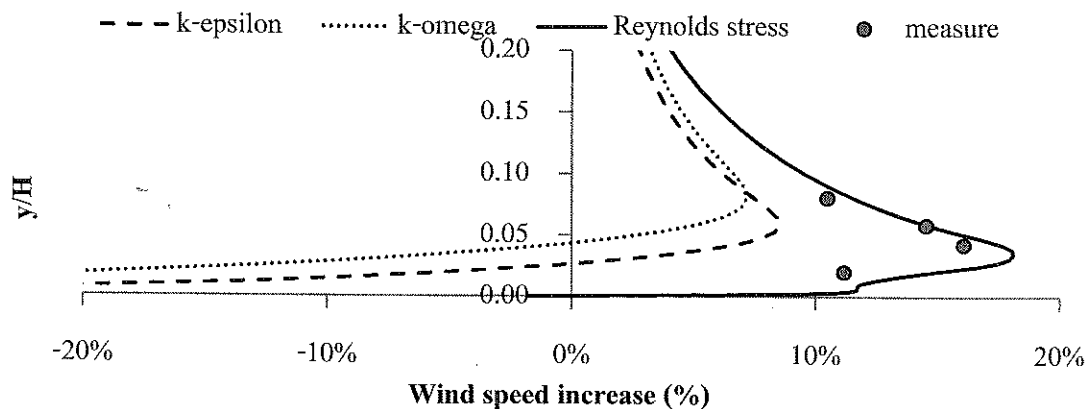


Figure 5.11 The comparison of wind velocity at hill top of difference models

Figure 5.12 showed the comparison of velocity in longitudinal direction of the flow. The weather stations located at x/H are -1.0, 0, 0.5, 1.0, 1.5 and 2.0 of the flow. An anemometer installed 5 m height from ground. The interval of wind speed recording is 10 second while 15 minutes of recorded time is collected. Raw data from site are improved, series of wind speed data of the flow are arranged together with appropriate of time.

From Figure 5.12, it is seen that RSM methods has little overestimate the speed-up effect compared to experimental results at $x/H = 0$ and 1.5. In the recirculating area at $x/H = 0.5$, no model predicts as large negative values of the horizontal velocity as the experimental results. Moving over to $x/H = 1.0$, it seems like none of the numerical methods have the ability to rebuild the boundary layer as fast as seen in the experiments. It seems like the diffusion in nature

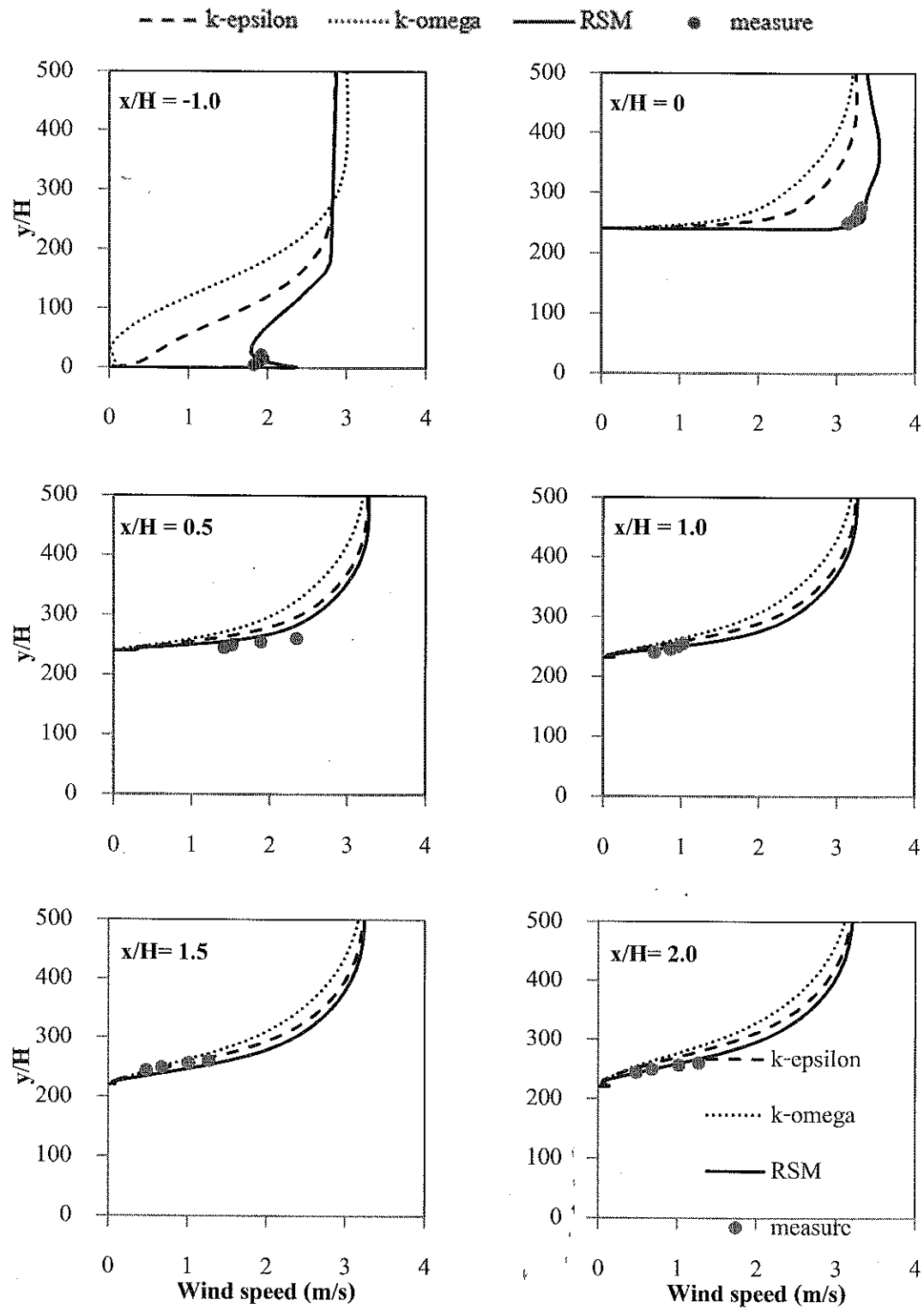


Figure 5.12 The comparison of velocity profiles in longitudinal direction

The speed-up seems to depend on the separation point location. A late separation is connected to larger pressure gradients and increased velocity at the hill summit. The $k-\omega$ method estimates the smallest recirculation bubble, as seen in Appendix C. From Figure 5.12, the RSM method also estimates the largest speed-up. This strong flow dependency on the recirculation bubble is also a problem in conjunction with model validation for flow cases with recirculating flow. The separation point estimation becomes the main parameter that describes the methods ability to predict the flow, and this can be quite random. This is clearly seen in conjunction with the RSM with the indirect wall function approach, which is found to depend largely on the thickness of the surface cell. This is also one of the conclusions where highly differing recirculation zones were found with different turbulence models, but also within groups of equal turbulence models.

Regarding the RSM method where good accordance between the measurements. The RSM turbulence model is also clearly differing from each other. The RSM results have some more numerical diffusion than the standard $k-\epsilon$ and standard $k-\omega$ methods. The velocity shear between the free stream flow and the recirculation zone is higher in the reference solution. This is probably both connected to the addition of artificial viscosity, and the fact that an eddy viscosity is used to calculate the diffusion of both ϵ and the Reynolds stresses.

Another effect that is seen in Figure 5.12 is the wiggle in the RSM results at the hill summit. This is connected to both large advection connected to large speed and a large pressure gradient. This is the well-known problem caused by the velocity-pressure coupling connected to collocated grid.

5.3.3 Comparison of turbulence kinetic energy

The turbulence kinetic energy illustrated measures and simulations. The $k-\epsilon$ model showed greatly approach with the measured since reference station to $x/H = 0.5$, while RSM and $k-\omega$ model expression dissimilar. After the distance $x/H = 0.5$ the all of simulation appear underestimation of TKE at 10 m height.

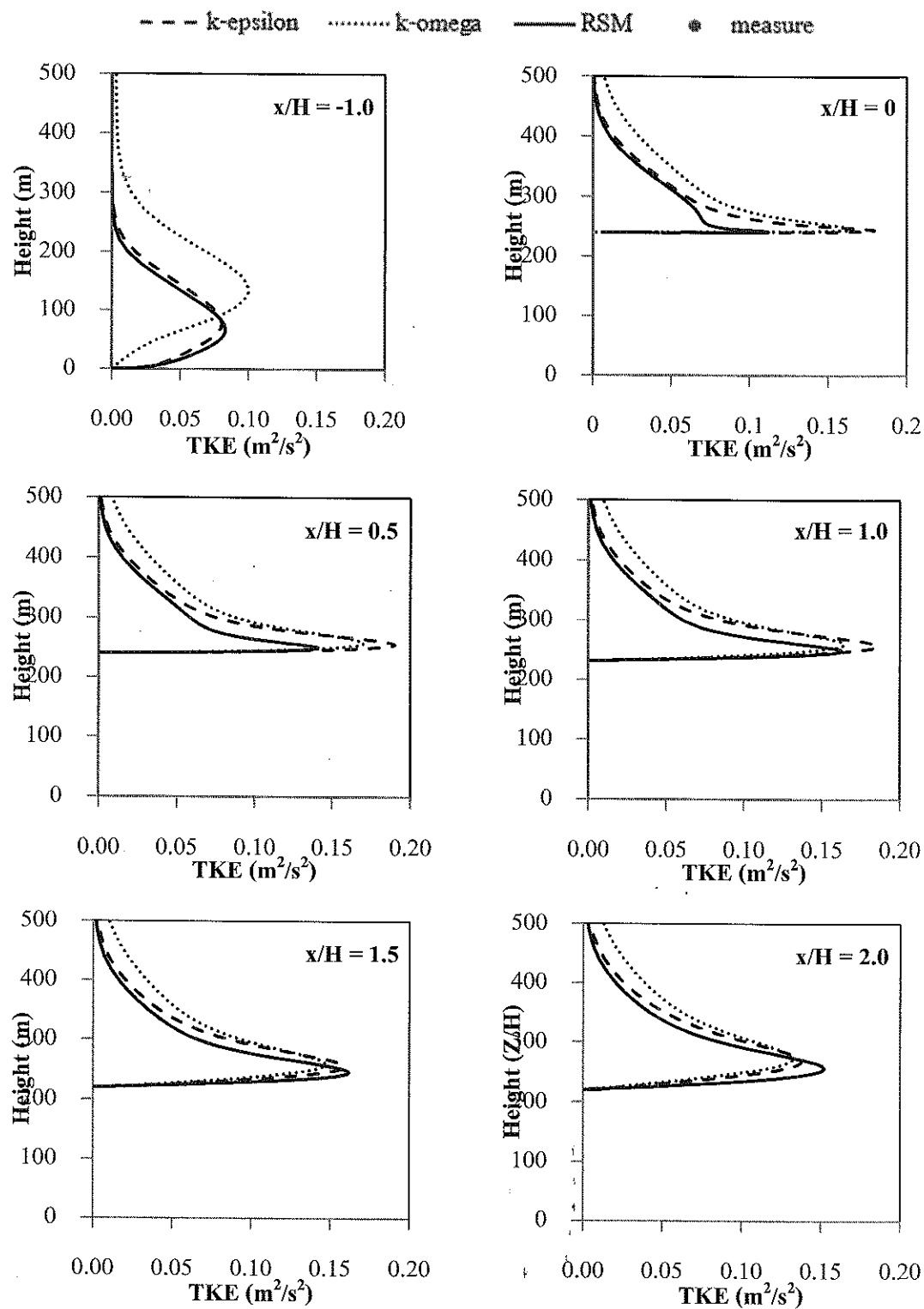


Figure 5.13 Comparison of turbulence kinetic energy in longitudinal direction

Turbulence kinetic energy show kinetic energy of mass, received from root mean square of Eddies current. Figure 5.13 showed the turbulence kinetic energy at distance $x/H = 0.5$, its maximum peak indicated near ground, but RSM showed overestimation around the ground. On the other hand, the $k-\epsilon$ model and $k-\omega$ model showed underestimation. The peak value of turbulence kinetic energy for the RSM, $k-\epsilon$ model and $k-\omega$ model appeared at $0.288 \text{ m}^2/\text{s}^2$, $0.190 \text{ m}^2/\text{s}^2$ and $0.166 \text{ m}^2/\text{s}^2$, respectively.

The main focus of this analysis has been on the lower wall, the surface where the obstruction is located. It is seen that the flow above the lower wall depends on the separation point. An analysis of the undisturbed boundary profile can give some additional information. Figure 5.13 and 5.14 shows the profile of the turbulent kinetic energy in longitudinal and vertical height. There are no measurements in the near wall area, so results are only compared to the wind stations. The turbulent kinetic energy from whole methods is higher while the velocity is lower than measures data.

5.3.4 Mean velocity component in the longitudinal

Velocities profiles in longitudinal direction of the flow are illustrated increasing speed of the flow along the hill. Three simulation methods were made for comparison. The initial and boundary conditions of the simulation are similarly. Measures data from wind stations with error bar have been applied to compare. Standard variation technique has been used to generate error bar of the data. In this case, two dimensions flows have been consider avoiding direction mistake.

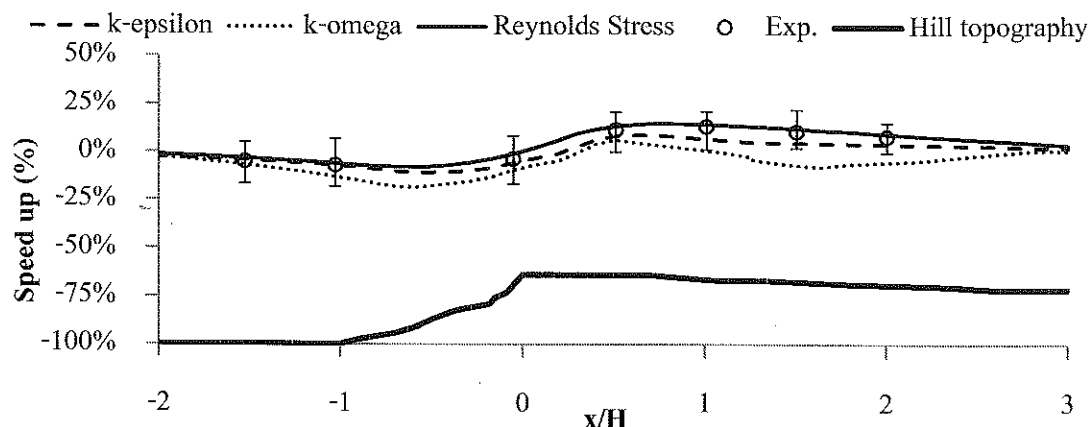


Figure 5.14 Mean velocity component in the longitudinal direction

The different turbulence models give qualitatively similar results, but quantitatively there are some differences; particularly in turbulence levels, but also in the velocities in the wake of the hill. From the speed-up profiles through the hill given in Figure 5.14, the upstream value is seen to be a little higher in the RSM case. This is probably connected to the fact that all turbulence models use the same inflow boundary profile. This profile is developed with the RNG turbulence model and is not the equilibrium state of the other turbulence models. As seen in Figure 5.10, profiles of the flow at reference station are no longer equal. The RSM value over 20 m height is quite high, but close to the ground the RSM has the nearest values with the measure. This indicates that the RSM acts similarly to a lower friction, and the increased velocity propagates up in the boundary layer. This difference could have been accounted for by adjusting the roughness friction value.

The standard $k-\epsilon$ model and standard $k-\omega$ are seen to be quite equal in the evaluated speed-ups in longitudinal direction. The $k-\omega$ model differs most from the other methods. As seen from Figure 5.15, this method gives low values in the lower parts of the hill distance in the flow direction, and increased speed-up at the hilltop, compared to the $k-\epsilon$ based methods. The RSM method calculates the highest speed-up values in the wake along the flow, where only the $k-\omega$ method is within the uncertainty limit. Along the stream line, the $k-\epsilon$ and $k-\omega$ methods underestimate the speed-up in the wake, while only $k-\omega$ method is within the uncertainty limit. No numerical results capture the difference from the ground to 5 m height. This is probably caused by subgrid topographic effects, measurement errors or a data treatment error.

5.3.5 Estimation of wind power density from Pha Taem

To estimated wind power density from Pha Taem hill, the data of Ubonratchathani region from years 2008 – 2010 in previous session have been used. The mean wind speed at 10 m, 30 m and 40 m height indicated 1.094 m/s, 1.784 m/s and 2.445 m/s, respectively. In Figures 5.11 and 5.14, maximum increased speed of the flow indicated at x/H and y/H equal 0.635 and 0.038, respectively, while the maximum speed of the flow increased 18.065 %.

Using air density ρ , scale factor c and shape factor k from Ubonratchathani region, wind power density of Pha Taem can be calculated from

$$P = \frac{1}{2} \rho c^3 \Gamma \left[1 + \frac{3}{k} \right] \quad (5.1)$$

$$P = \frac{1}{2} (1.2576)(2.3148^3) \Gamma \left[1 + \frac{3}{1.6040} \right] \quad (5.2)$$

$$P = 6.9910 \text{ W/m}^2 \quad (5.3)$$

The mean power density of Pha Taem hill is about 6.9910 W/m^2 . To calculate more accurate power, yearly wind data should be provided from installed weather station at position $x/H = 1$ front of the hill with 10 m tower height.

5.4 Comparison of Pha Taem geography and geometry shape

Pha Taem hill topography is similar with trapezoid geometry. To investigate suitable site of wind turbine matching with real topography reference geometry shape was used to associate with the actual hill structure as shown in Figure 5.15. The hill shape can be separated into two parts, the hill with 20.06° steep in front side and the flat rocky plate with 1.66° slopes in backside and few fences. The trapezoid geometry in the simulation is 20.0° steep and the flat plate 1.7° slopes in backside with 0.04 m height of roughness.

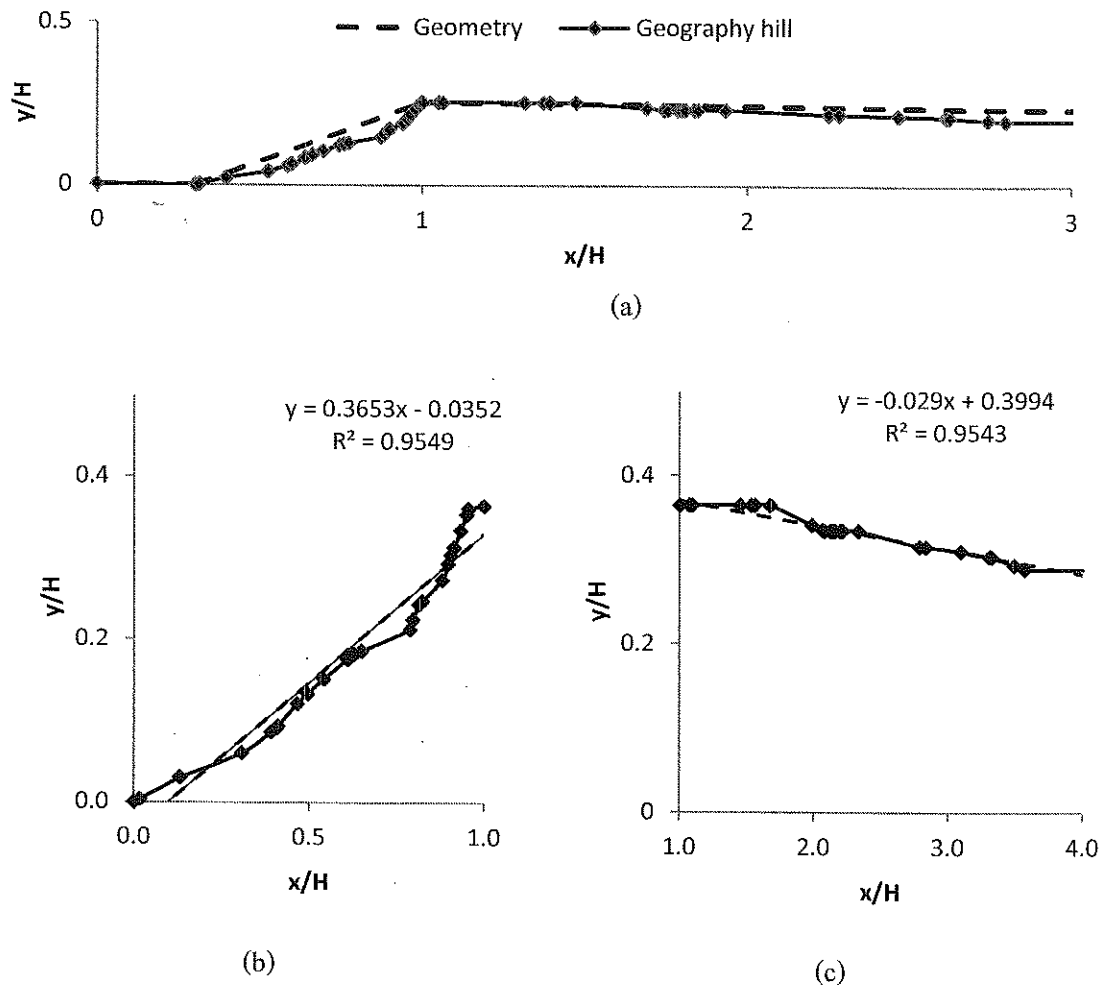


Figure 5.15 Pha Taem topography associate with reference trapezoid geometry

(a) Geometry matching with Pha Taem geometry, (b) Hill steep, (c) Flat plate

To comparison of the suitable site for turbine, identically initial and boundary conditions of both simulations domain have been applied. Pha Taem topography is 95.46% likewise with the trapezoid geometry, so, the potential position of wind energy should be valuable. In CFD simulation technique, results of the simulation afforded from their domain, initial and boundary condition, turbulence model, wall function approach, et al. Therefore, potential position of the flow over geometry resembles hill concurrently with its geometry likewise.

5.4.1 Comparison of wind speed

Figure 5.16 showed increasing velocity at $L/s = 0.5$ from the hill top. The RSM simulations indicated that resulted from Pha Taem hill topography provide similar velocity with

reference geometry shape from ground to $2z/H$ in vertical height, but in higher region the RSM showed further resulted at 2.63% in this region. The simulations from $k-\epsilon$ model and $k-\omega$ model illustrated similar tendency, which Pha Taem hill topography always appearance additional results at 5.02% and 10.53%. Since, rocky plate roughness surface from topography compose more turbulent intensity. The graphic of the results are indicated in Appendix B.

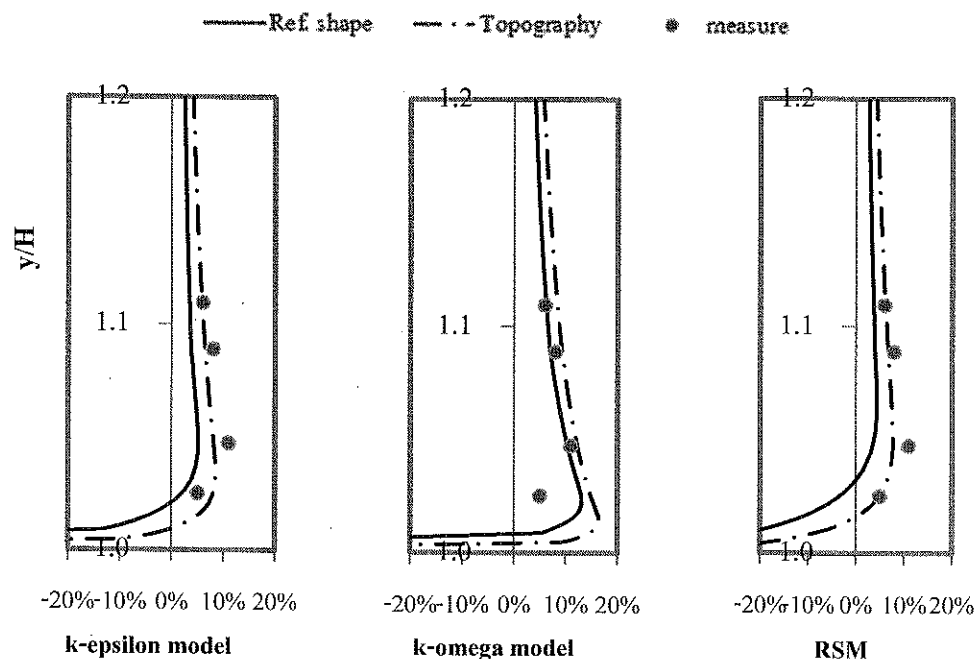


Figure 5.16 Increasing of velocity comparison of Pha Taem hill topography and reference geometry

The results comparison of the topography and geometry illustrated similarly trend. The wind speed increasing from Pha Taem has additional shift. The velocity profiles in RSM method indicated likewise with measurement while the standard $k-\epsilon$ and standard $k-\omega$ method indicated further speed at ground to $y/H = 0.2$ and rapidly decrease afterward. In additional speed zone from ground to $y/H = 0.5$, the RSM demonstrated most resemble with the measurements, the standard $k-\epsilon$ showed added speed at 5 m height and diminish at 10 m height, while indicated most further at 5 m height. In diminish zone after $y/H = 0.5$, the entire method displayed comparable results. Whole methods harvest sufficiency effect, tiny data are dissimilar from fluctuation in the flow.

Comparison of topography and geometry, the flow dependency on the topography has some recirculation from knobby on landscape surface. The recirculation bubble is also a problem in conjunction with model validation for flow cases with recirculating flow. The separation point estimation becomes the main parameter that describes the methods ability to predict the flow, and this can be quite random. This is clearly seen in conjunction with the RSM, which is found to depend largely on the thickness of the surface cell. This is also one of the conclusions where highly differing recirculation zones were found with different turbulence models, but also within groups of equal turbulence models.

5.4.2 Comparison of Turbulence kinetic energy

Investigation of the turbulence kinetic energy, comparison of the flow over Pha Taem hill topography and reference geometry shape are considered. The simulations results from k- Ω model showed mostly neighbor at 2.97% difference, while the k- ϵ model showed 8.02% difference as illustrated in Figure 5.17. The RSM resulted demonstrated two times further of turbulence kinetic energy.

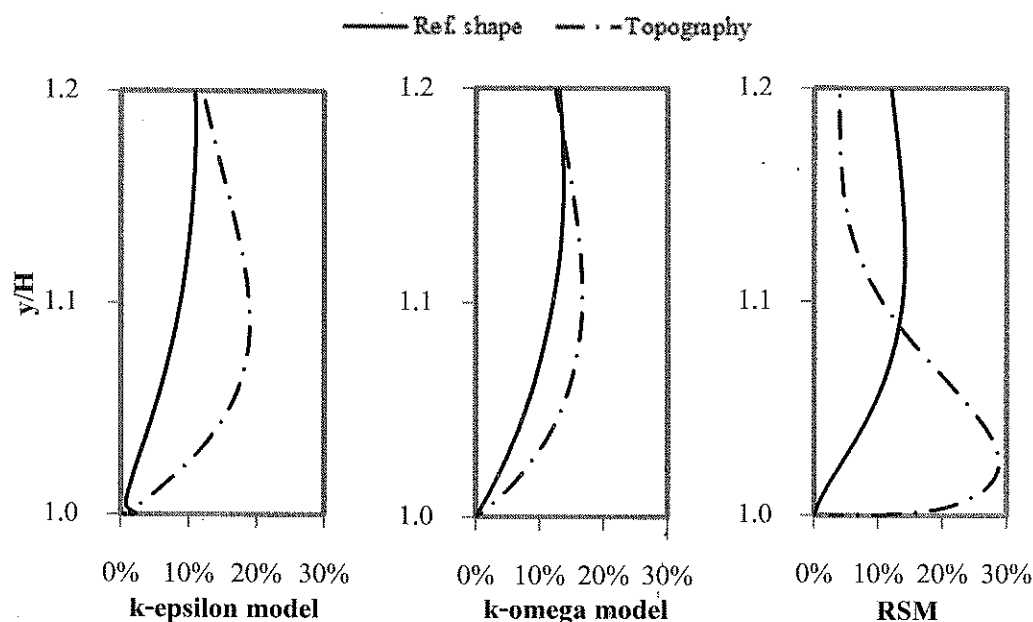


Figure 5.17 Comparison of turbulence kinetic energy increasing of the flow over Pha Taem hill topography and reference geometry shape

The turbulent kinetic energy profiles from trapezoid geometry have slighter increase in whole methods. This is maybe caused by the more roughness after hilltop. After $y/H = 0.2$ in RSM method has rapidly decrease of turbulent kinetic energy, this is probably both connected to the addition of artificial viscosity, and the fact that an eddy viscosity is used to calculate the diffusion of both \mathcal{E} and the Reynolds stresses.

5.5 Generate wind turbine suitable site chart

5.5.1 Simulation results of initial and boundary conditions dependence

This session demonstrated effect of hill angle, wind speed and roughness surface on suitable position of wind turbine hub. The simulations showed the position for each condition combined. Linear graph is generated for identified suitable position for small wind turbine. Figure 5.18 indicated suitable position of the turbine on trapezoid hill shape. Effect of hill angle, wind speed and roughness surface are considered. The simulation results are shown in Appendix B.

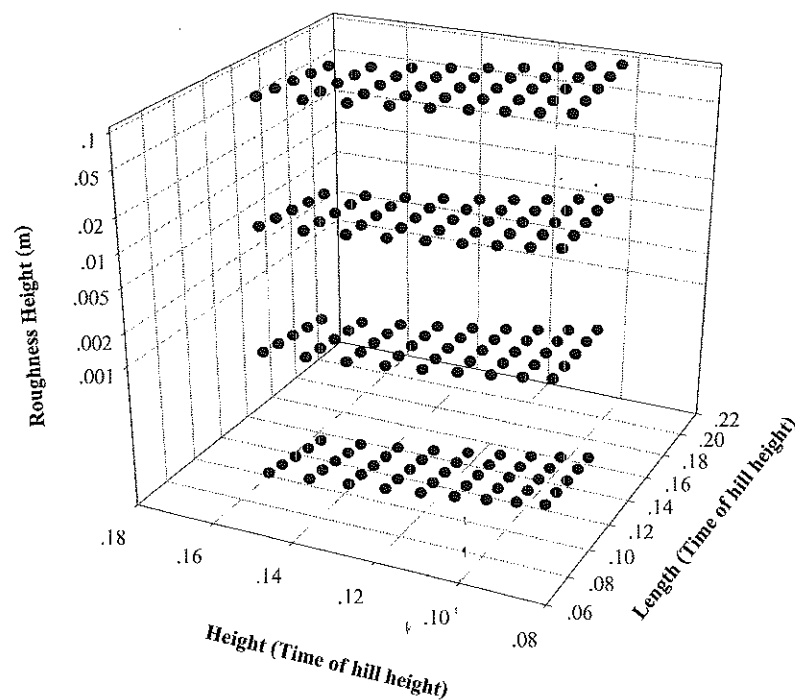


Figure 5.18 Suitable position from simulation results of the flow over trapezoid geometry terrain

Examination of hill angle transform with steady wind speed and roughness surface of the flow over trapezoid hill shape. The simulations indicated the suitable position of the hub has direct variation with hill angle in vertical, while reverse variation is shown in horizontal.

Roughness surface from 0.0001 – 0.1 m are applied in the simulations. Suitable position in vertical and horizontal are according variation with roughness height. The incompressible air will be lift up when flow over canopy top. While horizontal distances have less depends on roughness surface.

Most of commercial wind turbine has cut-in speed from 2.5 m/s. This work applied 2.0 – 10.0 m/s of background wind speed in the simulation. Since, wind data record in previous session was 0.5 – 11.0 m/s. The results of simulation indicated suitable position in horizontal are agree increase with background wind speed, while reverse variation are shown in vertical. Air is incompressible flow, therefore, suitable position are reverse with the speed to conserve the atmospheric pressure.

5.5.2 Extrapolation of wind turbine suitable site

We now describe in detail how to compute the coefficients $c_j = f[x_0, x_1, \dots, x_j]$, of the Newton extrapolating polynomial $p_n(x)$, and how to evaluate $p_n(x)$ efficiently using these coefficients.

The computation of the coefficients proceeds by filling in the entries of a divided-difference table. This is a triangular table consisting of $n+1$ columns, where n is the degree of the extrapolating polynomial to be computed. For $j = 0, 1, \dots, n$, the j th column contains $n-j$ entries, which are the divided differences $f[x_k, x_{k+1}, \dots, x_{k+j}]$, for $k = 0; 1, \dots, n-j$.

We construct the data by filling in the $n+1$ entries in column 0, which are the trivial divided differences $f[x_j] = f(x_j)$, for $j = 0, 1, \dots, n$. Then, we use the recursive definition of the divided differences to fill in the entries of subsequent columns. Once the construction of the table is complete, we can obtain the coefficients of the Newton extrapolating polynomial from the first entry in each column, which is $f[x_0, x_1, \dots, x_j]$, for $j = 0, 1, \dots, n$.

In a practical implementation of this algorithm, we do not need to store the entire table, because we only need the first entry in each column. Because each column has one fewer entry than the previous column, we can overwrite all of the other entries that we do not need. The following algorithm implements this idea.

The algorithm is given n distinct extrapolation points x_0, x_1, \dots, x_n and the values of a function $f(x)$ at these points, the following algorithm computes the coefficients $c_j = f[x_0, x_1, \dots, x_j]$ of the Newton extrapolating polynomial. The algorithm codes of the wind turbine suitable site chart are indicated in appendix D.

5.5.3 Generate the chart

The simulations results with effect of wind speed, hill angle and roughness surface on suitable positions are mentioned examine. Increasing of suitable position depended on variations demonstrated in constant increasing rate. Therefore, trend lines of the data with extrapolation technique have been used to expandable suitable position chart for trapezoid hill as shown in Figure 5.19 – 5.22. Finally, instruction manual of the chart are illustrated in Appendix E.

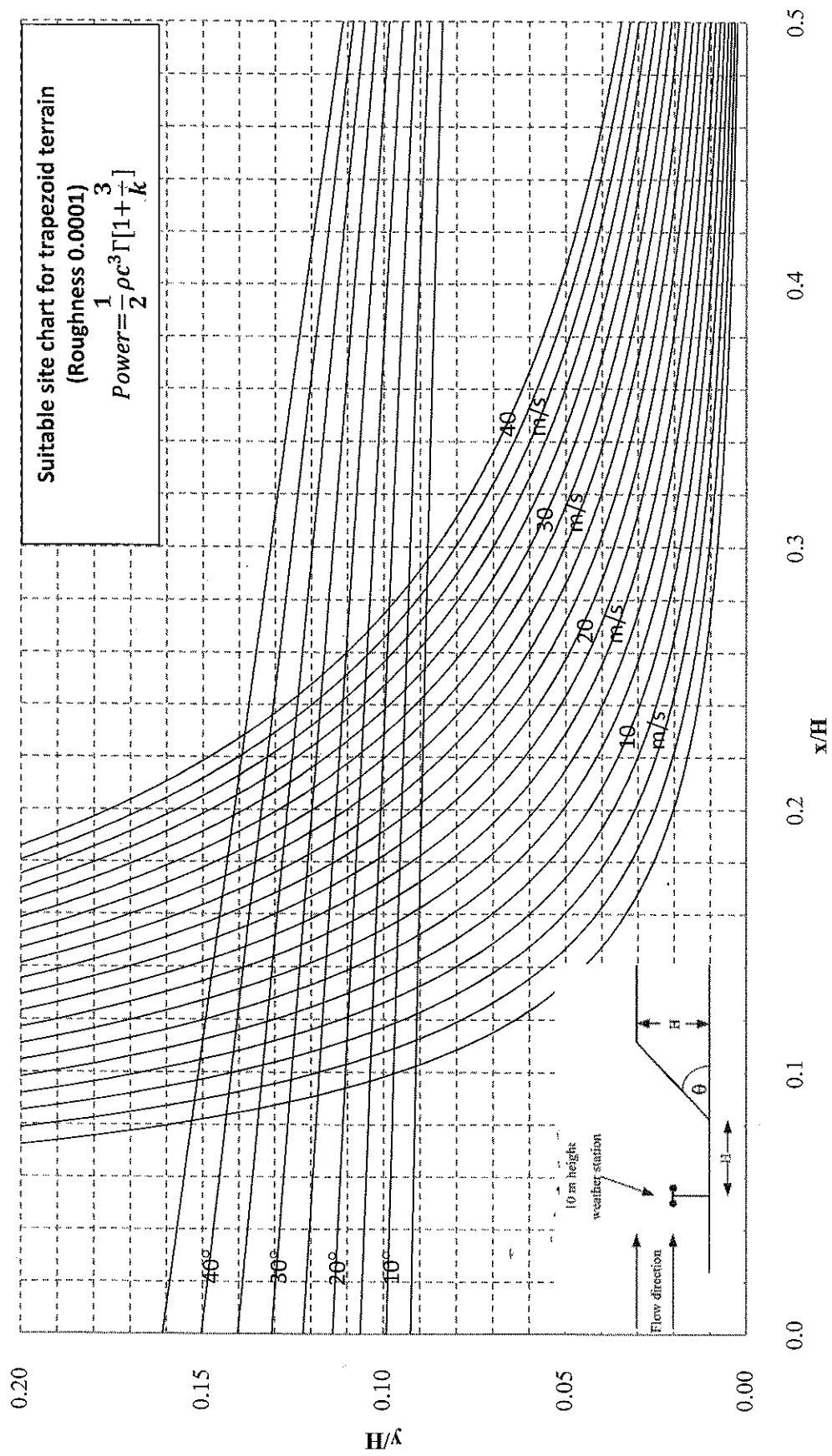


Figure 5.19 Suitable site chart for trapezoid hill shape at 0.0001 m of roughness height

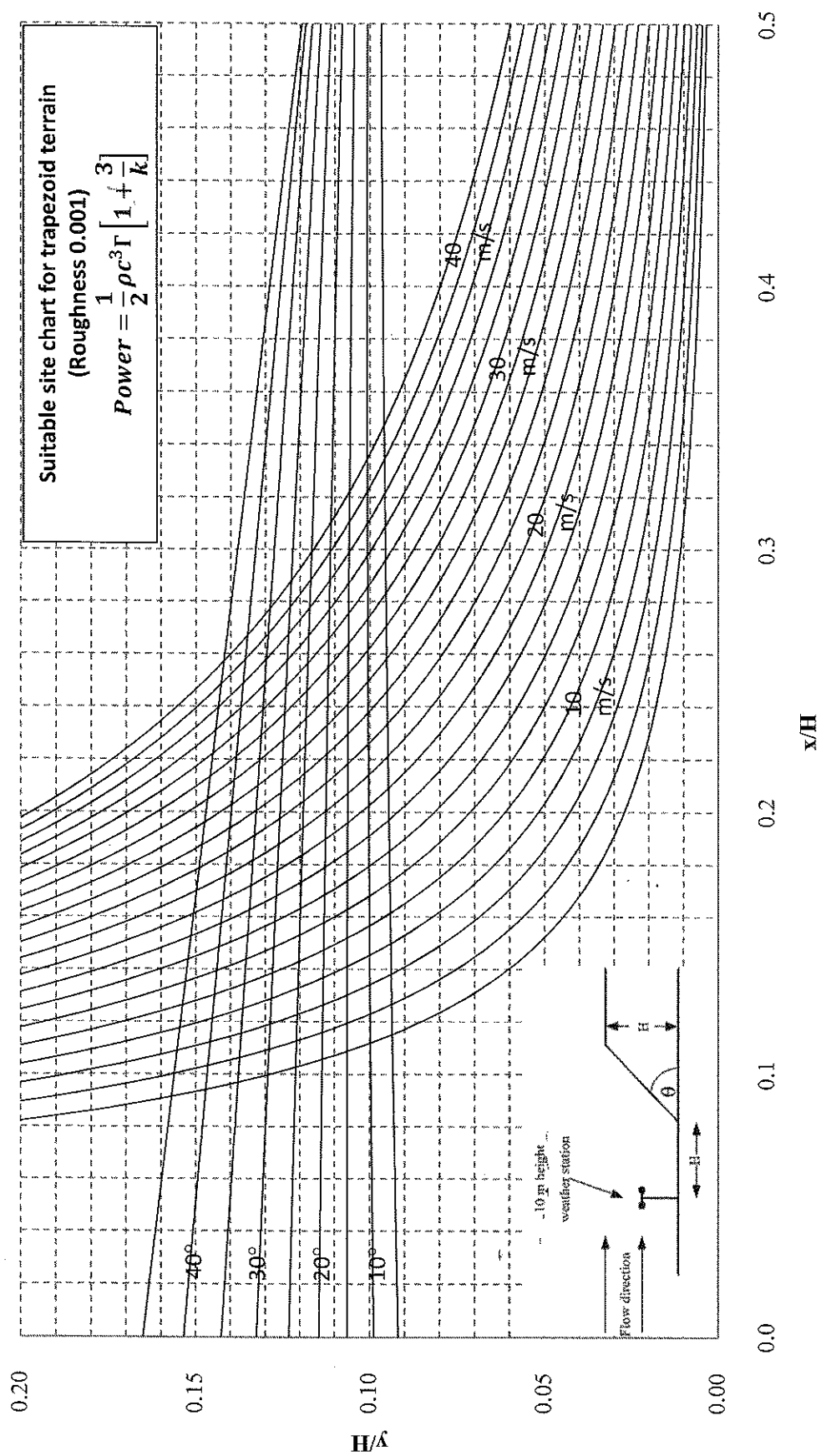


Figure 5.20 Suitable site chart for trapezoid hill shape at 0.001 m of roughness height

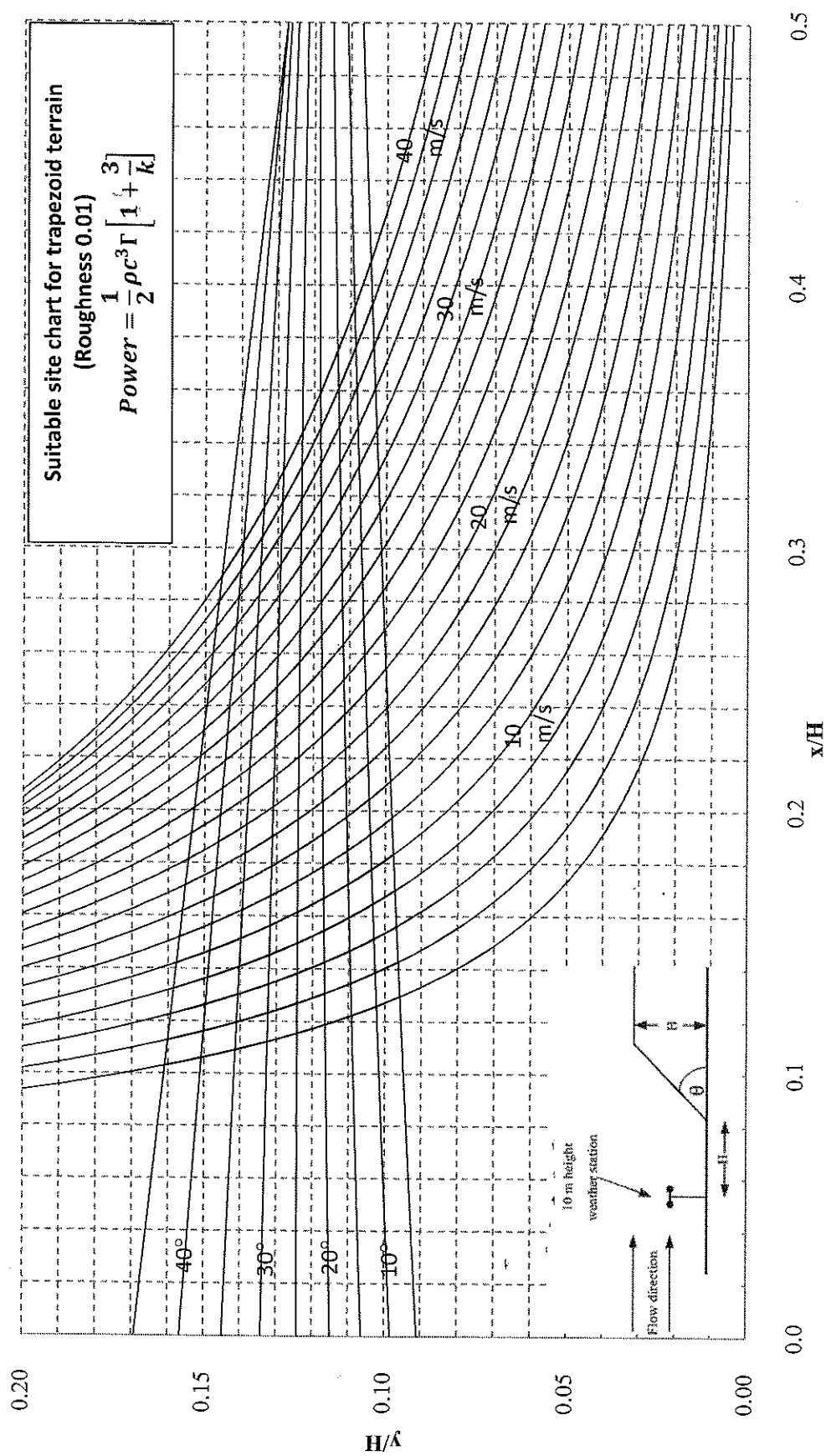


Figure 5.21 Suitable site chart for trapezoid hill shape at 0.01 m of roughness height

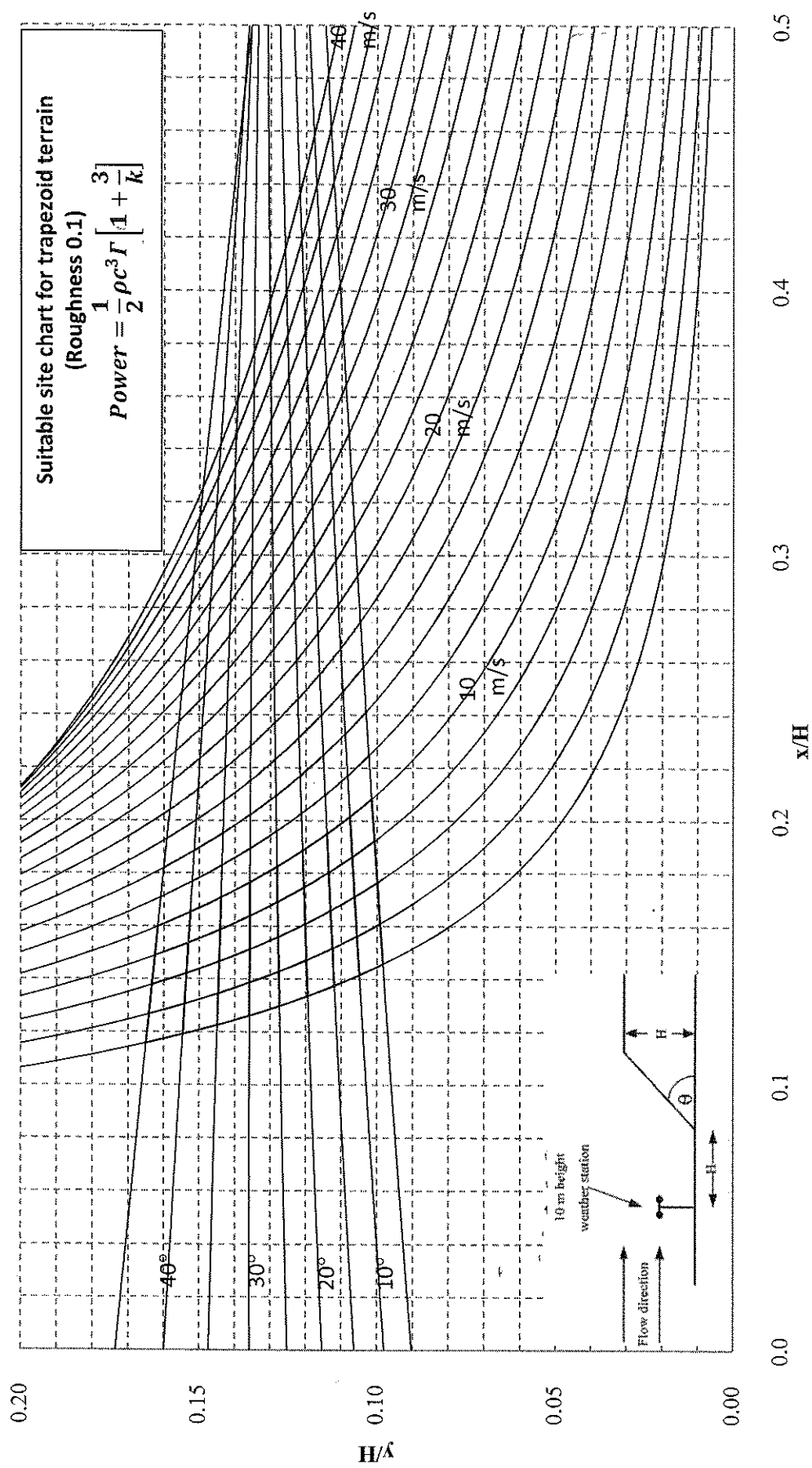


Figure 5.22 Suitable site chart for trapezoid hill shape at 0.1 m of roughness height

CHAPTER 6

CONCLUDING REMARKS

6.1 Wind energy potential assessment

Detailed of statistical study of wind data and potential assessment at 10 m, 30 m and 40 m heights in Ubonratchathani region for the years 2008–2010 are presented. Wind speeds are modeled using Weibull probability function whose parameters are estimated from the approximated approach. It is shown that the Weibull probability function, with parameters estimated from the approximated approach, predicts the wind speed and wind power more accurately than the other approach. Weibull parameters are used to estimate the approximated approach, the monthly and annual capacity factors are calculated for selected commercial wind turbine generators at 10 m, 30 m and 40 m heights.

Finally, it worth mentioning that the current work is only a preliminary study in order to estimate the wind energy potential analysis of Ubonratchathani, in order to have a comprehensive wind data base and obtain good predictions prior to construction and installation of wind energy conversion systems. In assessing the wind power potential or choosing the suitable type of wind turbine, not only the wind data but also the site circumstances (terrain, different referred height, etc.) should be considered that this issue can be addressed for application of new wind energy generation technology.

6.2 Simulation of Pha Taem hill

The computational fluid dynamics is used to analyze wind flow over Pha Taem hill which the hill shape can be separated into two parts, the hill with 20.06° steep and the flat rocky plate with 1.66° slope in backside and few fences. The simulation results of standard k- ϵ model, standard k- ω model and RSM were used to compare with the measurements.

Wind speed data of Pha Taem collected every 10 second from 7 stations in longitudinal. The mean wind velocity at reference station is 3.014 m/s. Investigation of wind velocity and uncertainty limits at 10 m height of measurements and simulations are adopted.

The results front of hilltop illustrate that the standard k- ϵ model and the measured are similar. After $x/H = 1.0$, the RSM method showed exact result with the measures while standard k- ϵ model and standard k- ω model show underestimation. The turbulence kinetic energy in the simulations illustrate that standard k- ϵ model show similar result with the measured from $x/H = -3.0$ to $x/H = 0.5$ after impacted, after $x/H = 0.5$ the simulation show underestimation of TKE at 10 m height.

6.3 Comparison of hill shape and geometry shape

Comparison of the Pha Taem hill topography is similar with 20.0° steep trapezoid geometry and the flat plate at 1.7° slopes in backside with 0.04 m roughness. The coefficient of determination between Pha Taem hill and trapezoid is 0.9546. The RSM simulations indicated that result of velocity from Pha Taem hill similar with trapezoid from ground to $y/H = 2$ in vertical. The simulation illustrated the 95.46% matching terrain have 91.28% of corresponding results.

6.4 Generate wind turbine suitable site chart

Suitable position of wind tower and hub height are effect on many variables such as wind speed and direction, atmospheric, hill shape and obstacles. Therefore effect of canopy height must be considering for choosing for install the wind turbine. The suitable site chart for wind turbine tower and hub of the flow over trapezoid indicated in linear chart which depend on wind speed, hill angle and roughness height are presented.

6.5 Suggestion and comments for further study

Wind flow in atmosphere contains short-term power fluctuation in variation are turbulence. Therefore, more measure station with more frequency and more sensitive instruments should be provided to collect most accurate wind data.

Geographic Information System is a system to store and indicated geographic data of the terrestrial. However, GIS data non-included any grass, plant and small obstacles. The 1:50,000 scales of data include much error into the simulations.

REFERENCES

- [1] Coelingh J.P., van Wijk A.J.M. and Holtslag A.A.M. "Analysis of wind speed observation solver the North Sea", Journal of Wind Engineering and Industrial Aerodynamics. 61: 51–69; 1996.
- [2] Sahin A.Z. and Aksakal A. "Wind power energy potential at the northeastern region of Saudi Arabia", Renewable Energy. 14: 435–40; 1998.
- [3] Vogiatzis N., Kotti K., Spanomitsios S. and Stoukides M. "Analysis of wind potential and characteristics in North Aegean Greece", Renewable Energy. 29: 1193–1208; 2004.
- [4] Naif M. and Al-Abbadi. "Wind energy resource assessment for five locations in Saudi Arabia", Renewable Energy. 30: 1489–1499; 2005.
- [5] Al Nassar W., Alhajraf S., Al-Enizi A. and Al-Awadhi L. "Potential wind power generation in the State of Kuwait", Renewable Energy. 30: 2149–2161; 2005.
- [6] Energy Policy and Planning Office. "Energy resource of Thailand", Energy resource of Thailand. <http://www.eppo.go.th/index-E.html>. 27 July, 2011.
- [7] Takahashi T., Ohtsu T., Yassin M.F., Kato S., Murakami S. "Turbulence characteristics of wind over a hill with a rough surface", Journal of Wind Engineering and Industrial Aerodynamics. 90: 1697-1706; 2002.
- [8] Coelingh J.P., van Wijk A.J.M. and Holtslag A.A.M. "Analysis of wind speed observations over the North Sea", Journal of Wind Engineering and Industrial Aerodynamics. 61(1): 51-69; 1996.
- [9] Ahmet Z. Şahin and Ahmet Aksakal. "Wind power energy potential at the northeastern region of Saudi Arabia", Renewable Energy. 14(1-4): 435-440; 1998.
- [10] Vogiatzis N., Kotti K., Spanomitsios S. and Stoukides M. "Analysis of wind potential and characteristics in North Aegean, Greece", Renewable Energy. 29(7): 1193-1208; 2004.
- [11] Naif M. and Al-Abbadi. "Wind energy resource assessment for five locations in Saudi Arabia", Renewable Energy. 30(10): 1489-1499; 2005.
- [12] Al-Nassar W., Alhajraf S., Al-Enizi A. and Al-Awadhi L. "Potential wind power generation in the State of Kuwait", Renewable Energy. 30(14): 2149-2161; 2005.

- [13] Bonfils Safari and Jimmy Gasore. "A statistical investigation of wind characteristics and wind energy potential based on the Weibull and Rayleigh models in Rwanda", Renewable Energy. 35(12): 2874-2880; 2010.
- [14] Ali Naci Celik. "A statistical analysis of wind power density based on the Weibull and Rayleigh models at the southern region of Turkey", Renewable Energy. 29(4): 593-604; 2004.
- [15] Mungwena W. "The distribution and potential utilizability of Zimbabwe's wind energy resource", Renewable Energy. 26: 363-377; 2002.
- [16] Weisser D. "A wind energy analysis of Grenada: an estimation using the Weibull density function", Renewable Energy. 28: 1803-1812; 2003.
- [17] Ulgen K. and Hepbasli A. "Determination of Weibull parameters for wind energy analysis of Izmir, Turkey", International Journal of Energy Research. 26: 495-506; 2002.
- [18] Seguro J.V. and Lambert T.W. "Modern estimation of the parameters of the Weibull wind speed distribution for wind energy analysis", Journal of Wind Engineering Industrial Aerodynamics. 85(1): 75-84; 2000.
- [19] Justus C.G. "Methods for estimating wind speed frequency distributions", Journal of Applied Meteorological. 1978.
- [20] Burton T., Sharpe D., Jenkins N. and Bossanyi E. Wind energy handbook. England: John Wiley and Sons, 2001.
- [21] Fawzi A. and Jowder L. "Wind power analysis and site matching of wind turbine generator in kingdom of Bahrain", Applied Energy. 86: 358-545; 2009.
- [22] Ali Naci Celik. "A statistical analysis of wind power density based on the Weibull and Rayleigh models at the southern region of Turkey", Renewable Energy. 29(4): 593-604; 2003.
- [23] Launder B.E. and Spalding D.B. Lectures in Mathematical Models of Turbulence. London, England: Academic Press, 1972.
- [24] Jonas Bredberg. On Two-equation Eddy-Viscosity Models. Sweden: University of Technology, 2001.
- [25] The Ministry of Interior. "Population of Thailand in year 2008" Royal Thai Consulate-General. http://www.dopa.go.th/stat/y_stat.html. 5 September, 2010.

- [26] Feregh GM. "Wind energy potential for Bahrain", Energy Conversion Management. 34(6): 499-506; 1993.
- [27] Wilcox D.C. Turbulence Modeling for CFD. California, United State: DCW Industries, Inc. La Canada, 1998.
- [28] Gibson M.M., and Launder B.E. "Ground Effects on Pressure Fluctuations in the Atmospheric Boundary Layer", Journal of Fluid Mechanics. 86: 491- 511; 1978.
- [29] Launder B.E. "Second-Moment Closure", International Journal of Heat and Fluid Flow. 10(4): 282-300; 1989.
- [30] Launder B.E, Reece G.J, and Rodi W. "Progress in the Development of a Reynolds-Stress Turbulence Closure", Journal of Fluid Mechanics. 68(3): 537-566; 1975.
- [31] Keyhani A., Ghasemi-Varnamkhasti M., Khanali M. and Abbaszadeh R. "An assessment of wind energy potential as a power generation source in the capital of Iran, Tehran", Energy. 35(1): 188-200; 2009.
- [32] Ramazan Kose. "An evaluation of wind energy potential as a power generation source in Kutahya, Turkey", Energy Conversion and Management. 45: 1631-1641; 2004.
- [33] Clarke K.C. "Advances in geographic information systems", Computers, Environment and Urban Systems. 10: 175-184; 1986.
- [34] Goodchild, Michael F. "Twenty years of progress: GIScience in 2010", Journal of Spatial Information Science. 11: 1-8; 2010.
- [35] Federal Geographic Data Committee. "Geospatial Positioning Accuracy Standards Part 3: National Standard for Spatial Data Accuracy", National Aeronautics and Space Administration. 1998.
- [36] Longley, P. A, Goodchild, M.F, McGuire D.J, and Rhind D.W. Analysis of errors of derived slope and aspect related to DEM data properties. West Sussex, England: John Wiley and Sons, 2005.
- [37] Hunter G.J., and Goodchild M.F. "Modeling the uncertainty of slope and aspect estimates derived from spatial databases", Geographical Analysis. 29 (1): 35-49; 1997.
- [38] Meishen Li and Xianguo Li. "Investigation of wind characteristics and assessment of wind energy potential for Waterloo region, Canada", Energy Conversion and Management. 46: 3014-3033; 2005.

- [39] Murat Gokcek, Ahmet Bayulken and sukrü Bekdemir. "Investigation of wind characteristics and wind energy potential in Kırklareli, Turkey", Renewable Energy. 32: 739–752; 2007.
- [40] Elamouri M. and Ben Amar F. "Wind energy potential in Tunisia", Renewable Energy. 33: 758–768; 2008.
- [41] Jacob A. Wisse and Kees Stigter. "Wind engineering in Africa", Journal of Wind Engineering and Industrial Aerodynamics. 95: 908–927; 2007.
- [42] Al-Mohamad A. and Karmeh H. "Wind energy potential in Syria", Renewable Energy. 28: 1039–1046; 2003.
- [43] Adrian Ilinca. "Wind potential assessment of Quebec Province", Renewable Energy. 28: 1881–1897; 2003.
- [44] Nfaoui H., Buret J., and Sayigh A.A.M. "Wind characteristics and wind energy potential in Morocco", Solar Energy. 63(1): 51–60; 1998.
- [45] Shuzo Murakami, Akashi Mochida and Shinsuke Kato. "Development of local area wind prediction system for selecting suitable site for windmill", Journal of Wind Engineering and Industrial Aerodynamics. 91: 1759–1776; 2003.
- [46] Atsushi Yamaguchi, Takeshi Ishihara and Yozo Fujino. "Experimental study of the wind flow in a coastal region of Japan", Journal of Wind Engineering and Industrial Aerodynamics. 91: 247–264; 2003.
- [47] Getachew Bekele and Bjorn Palm. "Wind energy potential assessment at four typical locations in Ethiopia", Applied Energy. 86: 388–396; 2009.
- [48] Ioannis Fyrripiis, Petros J. Axaopoulos and Gregoris Panayiotou. "Wind energy potential assessment in Naxos Island, Greece", Applied Energy. 87: 577–586; 2010.
- [49] Bert Blocken. "CFD simulation of the atmospheric boundary layer: wall function problems", Atmospheric Environment. 41: 238–252; 2007.
- [50] Hargreaves D.M and Wright N.G. "On the use of the k- ϵ model in commercial CFD software to model the neutral atmospheric boundary layer", Journal of Wind Engineering and Industrial Aerodynamics. 95: 355–369; 2007.
- [51] Undheim O. "2D simulations of terrain effects on atmospheric flow", in Conference proceedings MekIT'05. 1-93. Norway: Institute for Energy Technology, 2005.

- [52] Ove Undheim. "Comparison of turbulence models for wind evaluation in complex terrain", Conference proceedings EWEC 2003. Norway: Institutt for energiteknikk, 2003.
- [53] Ian P. Castro and David D. Apsley. "Flow and dispersion over topography: A comparison between numerical and laboratory data for two-dimensional flows" Atmospheric Environment. 31: 839-850; 1997.
- [54] Pual Carpenter and Nicholas Locke. "Investigation of wind speeds over multiple 2D hills", Journal of Wind Engineering and Industrial Aerodynamics. 83: 109-120; 1999.
- [55] Keith W. Ayotte. "Computational modelling for wind energy assessment", Journal of Wind Engineering and Industrial Aerodynamics. 96: 1571-1590; 2008.
- [56] Apsley D.D. and Leschziner M.A. "A new low-Reynolds-number nonlinear two-equation turbulence model for complex flows", International Journal of Heat and Fluid Flow. 19: 209-222; 1998.
- [57] Menter F.R. "Two-equation eddy viscosity turbulence models for engineering applications", AIAA Journal. 32: 1598-1605; 1994.
- [58] Paul Stangroom. CFD Modelling of Wind Flow Over Terrain. Ph.D: University of Nottingham, 2004.

APPENDICES

APPENDIX A
WIND DATA OF UBONRATCHATHANI IN YEAR 2008 - 2010

Table A.1 The frequency of wind speeds for height of 10 m for year 2008-2010

Speed (m/s)	0.5	1.0	1.5	2.0	2.5	3.0	3.5	4.0	4.5	5.0	5.5	6.0	6.5	7.0	7.5	8.0	8.5	9.0	9.5	10.0	10.5	11.0
January	1,177	329	184	174	101	125	43	41	20	15	11	9	1	0	2	0	0	0	0	0	0	0
February	1,082	330	194	198	110	69	32	20	1	4	0	0	0	0	0	0	0	0	0	0	0	0
March	1,198	395	228	190	89	76	24	18	6	5	2	1	0	0	0	0	0	0	0	0	0	0
April	1,266	399	187	148	70	57	12	12	2	6	1	0	0	0	0	0	0	0	0	0	0	0
May	1,346	398	188	131	68	52	19	12	8	7	2	1	0	0	0	0	0	0	0	0	0	0
June	1,252	426	158	146	66	47	27	21	9	7	1	0	0	0	0	0	0	0	0	0	0	0
July	1,247	369	183	163	93	66	41	40	19	9	2	0	0	0	0	0	0	0	0	0	0	0
August	1,276	387	150	150	87	80	36	30	21	9	3	3	0	0	0	0	0	0	0	0	0	0
September	1,563	300	128	80	48	26	10	4	1	0	0	0	0	0	0	0	0	0	0	0	0	0
October	1,364	376	152	125	55	54	34	25	10	10	2	2	2	1	2	0	0	0	0	0	0	0
November	964	229	108	139	90	90	63	49	27	11	7	2	3	4	1	0	0	0	0	0	0	0
December	911	356	177	201	139	143	99	75	61	46	22	11	6	1	0	0	0	0	0	0	0	0
Summary	14,646	4,294	2,037	1,845	1,016	885	440	347	185	129	53	29	12	6	5	0	0	0	0	0	0	0

Table A.2 The frequency of wind speeds for height of 30 m for year 2008-2010

Speed (m/s)	0.5	1.0	1.5	2.0	2.5	3.0	3.5	4.0	4.5	5.0	5.5	6.0	6.5	7.0	7.5	8.0	8.5	9.0	9.5	10.0	10.5	11.0
January	786	316	192	201	134	185	115	98	56	64	35	19	7	10	4	6	2	0	0	2	0	0
February	691	296	212	206	182	179	101	91	32	33	11	4	2	0	0	0	0	0	0	0	0	0
March	704	456	263	255	145	167	73	70	44	33	9	7	2	3	0	1	0	0	0	0	0	0
April	804	465	258	219	115	114	70	57	28	12	9	4	1	3	1	0	0	0	0	0	0	0
May	657	495	268	272	162	142	78	68	36	26	10	7	4	4	2	1	0	0	0	0	0	0
June	671	458	263	229	143	157	83	80	27	18	18	9	4	0	0	0	0	0	0	0	0	0
July	636	436	246	243	171	147	106	109	52	47	20	12	6	1	0	0	0	0	0	0	0	0
August	626	456	252	234	160	139	103	100	56	49	22	16	11	2	3	2	1	0	0	0	0	0
September	972	452	192	187	121	96	43	56	22	13	5	1	0	0	0	0	0	0	0	0	0	0
October	787	348	180	235	143	174	100	91	52	43	22	16	8	7	1	2	1	2	2	0	0	0
November	713	288	103	92	92	90	76	103	79	84	54	30	15	7	3	2	1	3	3	2	0	0
December	606	300	171	179	159	170	123	151	91	104	59	34	31	15	15	11	3	2	1	0	0	0
Summary	8,653	4,766	2,600	2,552	1,727	1,760	1,071	1,074	575	526	274	159	91	52	29	25	8	7	6	4	0	0

Table A.3 The frequency of wind speeds for height of 40 m for year 2008-2010

Speed (m/s)	0.5	1.0	1.5	2.0	2.5	3.0	3.5	4.0	4.5	5.0	5.5	6.0	6.5	7.0	7.5	8.0	8.5	9.0	9.5	10.0	10.5	11.0
January	334	196	135	199	177	229	195	291	182	110	66	48	22	15	7	9	9	5	1	0	0	2
February	278	192	168	186	183	226	217	240	148	120	40	25	11	4	2	0	0	0	0	0	0	0
March	285	253	186	222	193	307	224	246	129	96	47	25	5	6	4	3	1	0	0	0	0	0
April	331	305	232	291	184	265	186	163	87	68	15	16	7	5	2	2	0	1	0	0	0	0
May	393	311	247	273	221	289	175	147	64	55	19	16	9	4	3	4	2	0	0	0	0	0
June	347	325	200	290	217	249	172	175	67	60	22	16	9	9	1	1	0	0	0	0	0	0
July	356	282	206	237	204	251	179	202	107	103	43	38	14	6	4	0	0	0	0	0	0	0
August	354	261	205	269	200	273	162	180	98	99	43	43	16	18	3	2	3	2	1	0	0	0
September	625	367	226	230	153	198	155	84	53	46	10	8	4	1	0	0	0	0	0	0	0	0
October	490	270	174	191	130	169	171	195	143	118	64	49	27	23	8	4	0	2	0	3	1	1
November	863	290	120	122	111	119	104	107	80	90	62	42	22	10	8	6	2	2	0	0	0	0
December	523	240	133	166	135	177	138	197	142	132	68	71	27	31	11	23	9	5	2	0	2	0
Summary	5,179	3,292	2,232	2,676	2,108	2,752	2,078	2,227	1,300	1,097	499	397	173	132	53	54	26	17	4	3	3	3

APPENDIX B
WIND POWER DENSITY CALCULATION

Example of wind power density calculation using Weibull distribution

Case : wind speed data in January, 2008 – 2010 at 40 m height.

To assess wind power density using Weibull distribution function at weather station site, the whole wind data in January from date 1 to 31 in years 2008 – 2010 at 40 m height are adopt in this calculations.

1. mean monthly wind speed (V_m)

$$V_m = \left[\frac{\sum V_i}{N} \right]$$

$$V_m = \left[\frac{3.5 + 2.3 + 1.8 + 3.1 + \dots}{24 \times 31 \times 3} \right]$$

$$V_m = 2.910 \text{ m/s}$$

2. Standard Deviation (σ)

$$\sigma = \left[\frac{\sum (V - V_i)^2}{N} \right]^{1/2}$$

$$\sigma = \left[\frac{(3.5 - 2.91)^2 + (2.3 - 2.91)^2 + \dots + (1.8 - 2.91)^2 + (3.1 - 2.91)^2 + \dots}{24 \times 31 \times 3} \right]^{1/2}$$

$$\sigma = 1.761058$$

3. Shape factor (k)

$$k = \left[\frac{\sigma}{V_m} \right]^{-1.086}$$

$$k = \left[\frac{1.7610584}{2.910} \right]^{-1.086}$$

$$k = 0.891363$$

4. Gamma function (Γ)

$$\Gamma(x) = (2\pi x)^{1/2} (x)^{x-1} (e)^{-x} \left(1 + \frac{1}{12x} + \frac{1}{288x^2} - \frac{139}{51840x^3} + \dots \right)$$

$$\Gamma\left(\frac{k+3}{k}\right) = \left[\left(2\pi \frac{k+3}{k} \right)^{1/2} \left(\frac{k+3}{k} \right)^{\frac{k+3}{k}-1} (e)^{-\frac{k+3}{k}} \times \left(1 + \frac{1}{12 \times \frac{k+3}{k}} + \frac{1}{288 \times \frac{k+3}{k}^2} - \frac{139}{51840 \times \frac{k+3}{k}^3} + \dots \right) \right]$$

$$\Gamma(2.73812) = \left[(4.7382\pi)^{1/2} (2.7382)^{1.7382} (e)^{-2.7382} \times \left(1 + \frac{1}{32.8592} + \frac{1}{2159.3489} - \frac{139}{1064291.2489} + \dots \right) \right]$$

$$\Gamma(2.73812) = 1.59302$$

5. Scale factor (c)

$$c = \frac{V_m}{\Gamma\left(\frac{1}{1+k}\right)}$$

$$c = \frac{2.910}{\Gamma\left(\frac{1}{1+0.891363}\right)}$$

$$c = 2.864660 \text{ (m/s)}$$

So, calculation results of wind power density for Weibull approximation methods are indicated in Table B.1. The whole parameters values of the calculation are indicated in Chapter 2.

Table B.1 Parameters in Weibull approximation method for wind power density calculation in January, 2008 – 2010 at 40 m height

Month	Average wind speed V_m (m/s)	standard deviation σ (m/s)	Shape factor (k)	Scale factor (c) (m/s)
January	2.910	1.761	0.891	2.864

6. Wind power density

$$P_{WmW} = \frac{1}{2} \rho c^3 \Gamma\left[1 + \frac{3}{k}\right]$$

$$P_{WmW} = \frac{1}{2} (1.374) (2.864^3) \Gamma\left[1 + \frac{3}{0.891}\right]$$

$$P_{WmW} = 16.93 \text{ W/m}^2$$

APPENDIX C
SIMULATION RESULTS OF PHA TAEM AND
TARPEZOID GEOMETRY

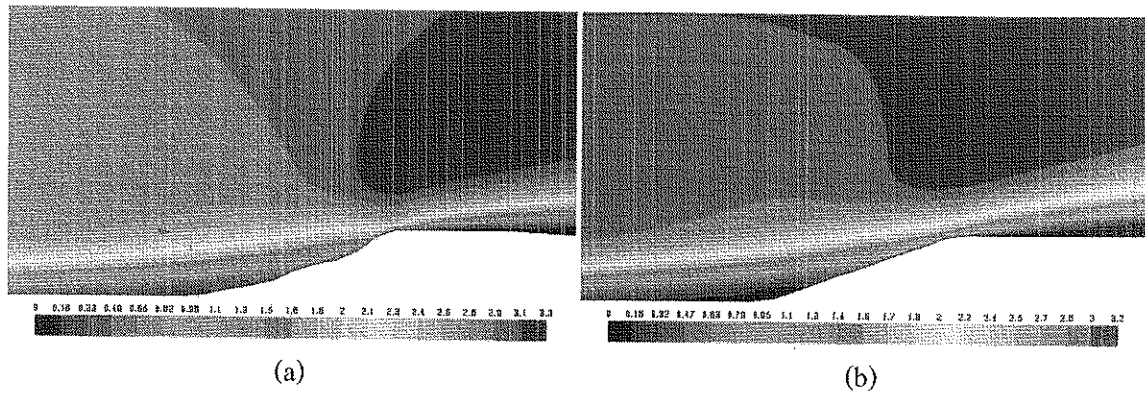


Figure. C.1 The contour plot of the velocity magnitude from the flow over terrain calculated with $k-\epsilon$ turbulence model

(a) Pha Taem topography, (b) trapezoid geometry

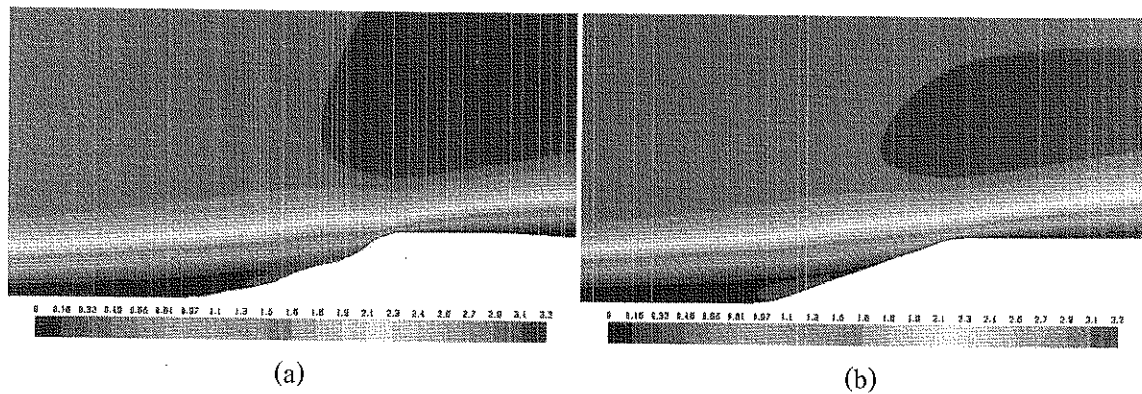


Figure. C.2 The contour plot of the velocity magnitude from the flow over Pha Taem terrain calculated with $k-O$ turbulence model

(a) Pha Taem topography, (b) Trapezoid geometry

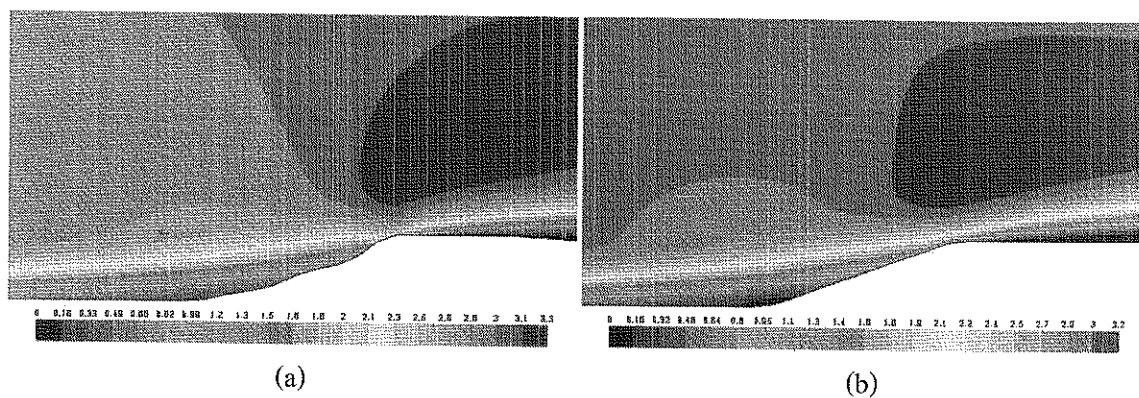


Figure. C.3 The contour plot of the velocity magnitude from the flow over terrain calculated with Reynolds stress model

(a) Pha Taem topography, (b) Trapezoid geometry

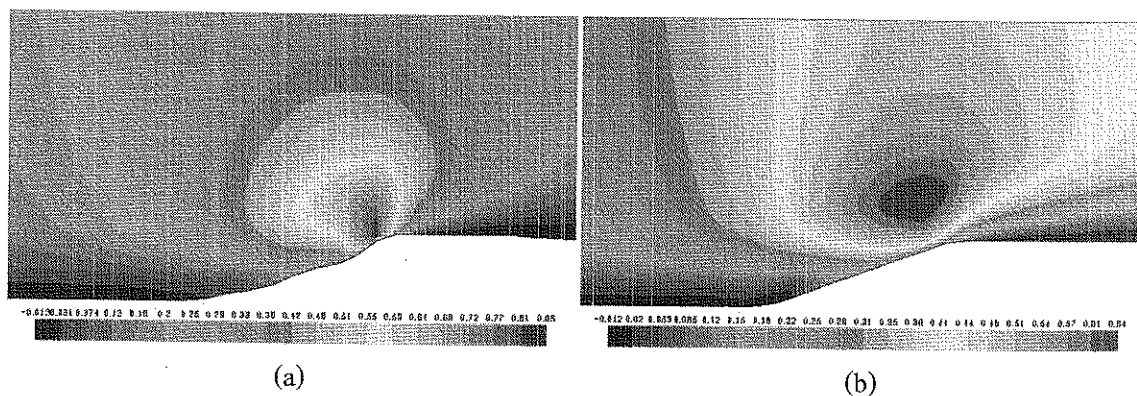


Figure. C.4 The contour plot of the vertical velocity from the flow over terrain calculated with k- ϵ turbulence model

(a) Pha Taem topography, (b) Trapezoid geometry

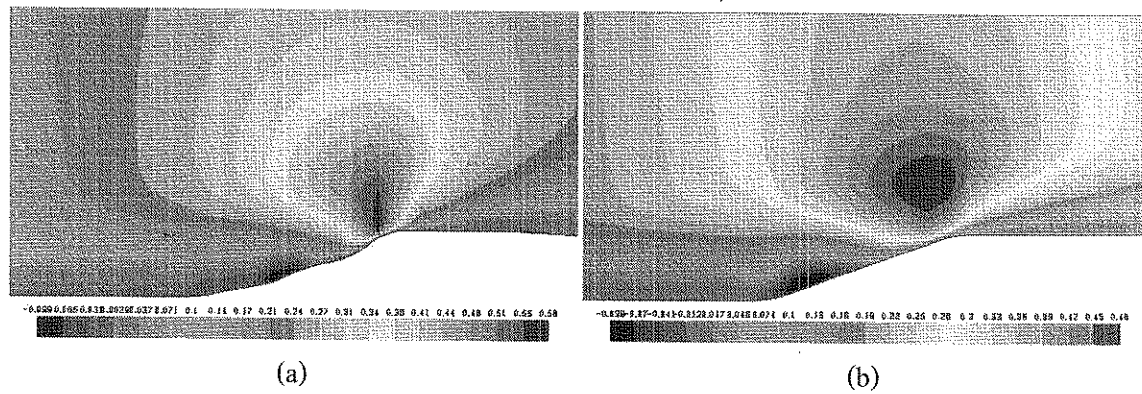


Figure. C.5 The contour plot of the vertical velocity from the flow over terrain calculated with $k-\omega$ turbulence model

(a) Pha Taem topography, (b) Trapezoid geometry

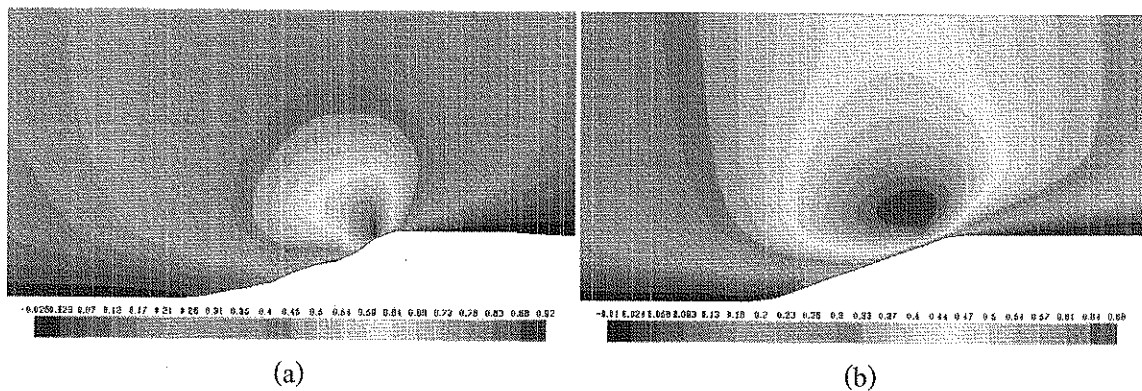


Figure. C.6 The contour plot of the vertical velocity from the flow over terrain calculated with Reynolds stress model

(a) Pha Taem topography, (b) Trapezoid geometry

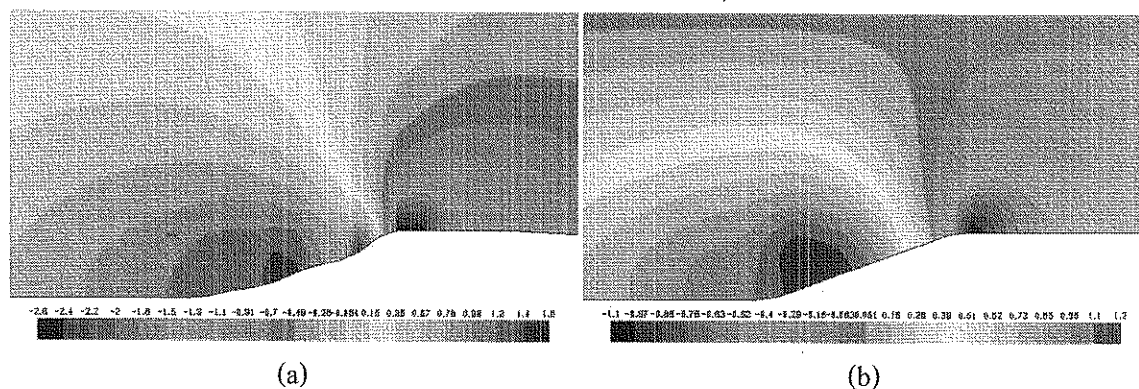


Figure. C.7 The contour plot of the static pressure from the flow over terrain calculated with $k-\epsilon$ turbulence model

(a) Pha Taem topography, (b) Trapezoid geometry

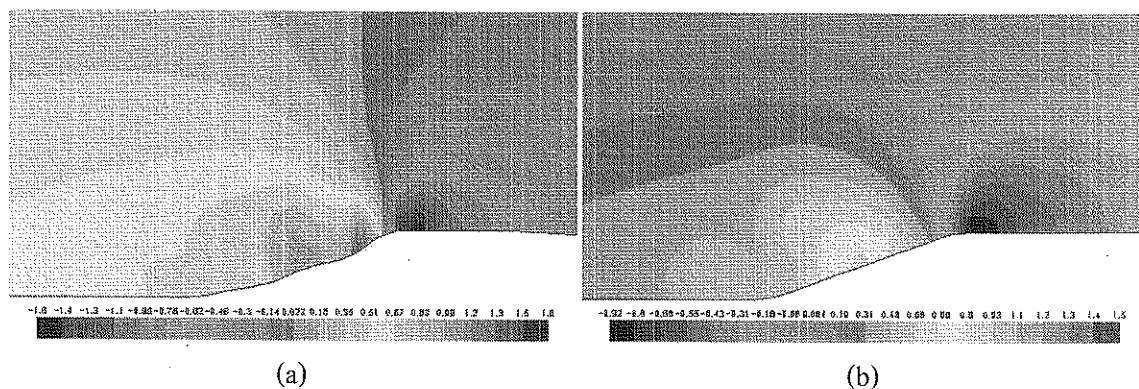


Figure. C.8 The contour plot of the static pressure from the flow over terrain calculated with $k-\Omega$ turbulence model

(a) Pha Taem topography, (b) Trapezoid geometry

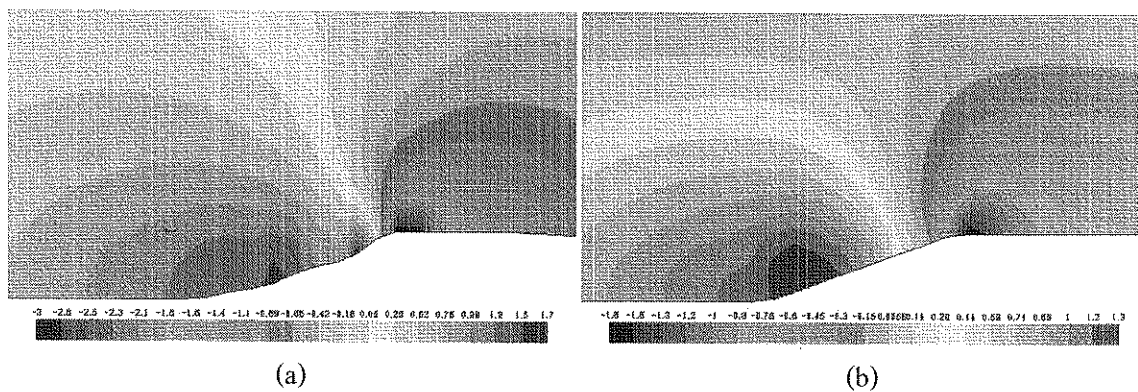


Figure. C.9 The contour plot of the static pressure from the flow over terrain calculated with Reynolds stress model

(a) Pha Taem topography, (b) Trapezoid geometry

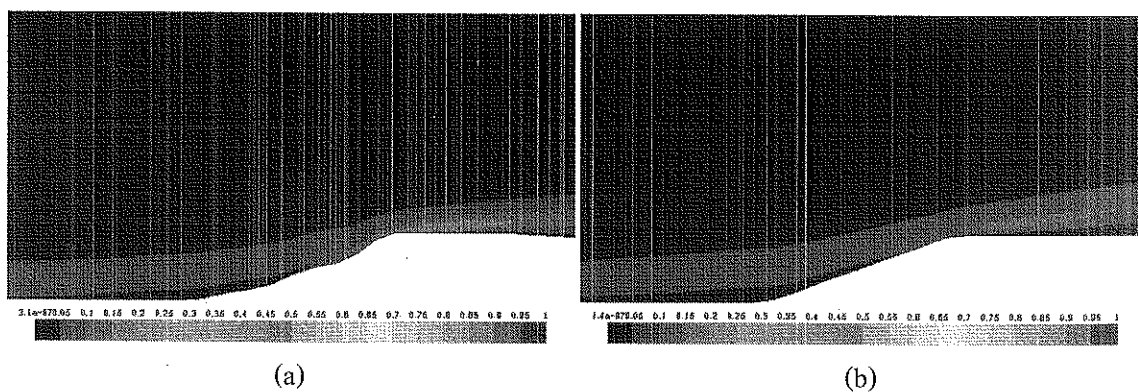


Figure. C.10 The contour plot of the turbulence kinetic energy from the flow over terrain calculated with $k-\epsilon$ turbulence model

(a) Pha Taem topography, (b) Trapezoid geometry

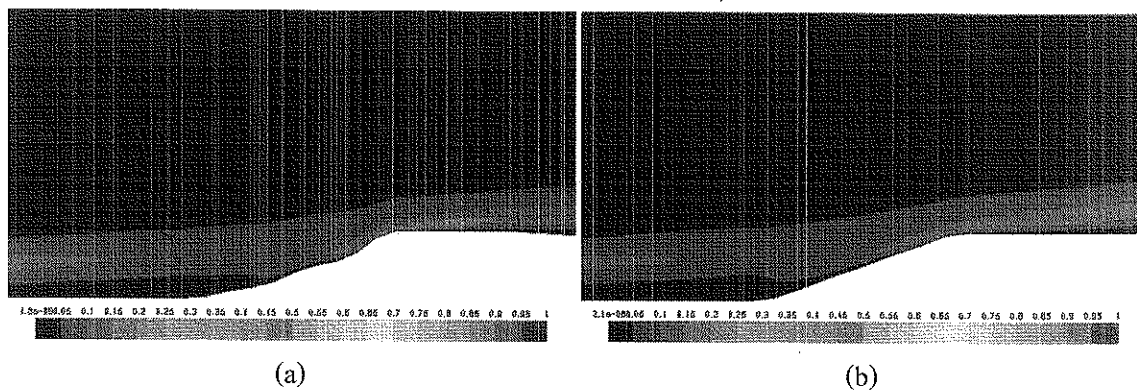


Figure. C.11 The contour plot of the turbulence kinetic energy from the flow over terrain calculated with $k-\omega$ turbulence model

(a) Pha Taem topography, (b) Trapezoid geometry

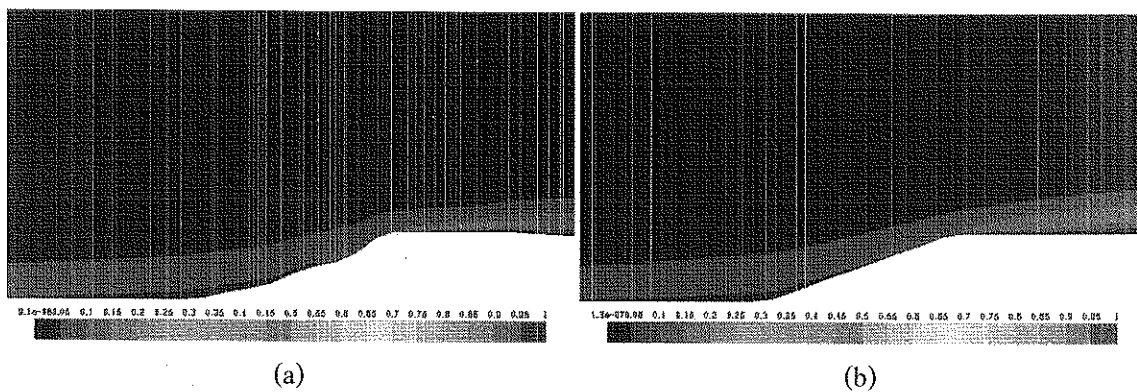


Figure. C.12 The contour plot of the turbulence kinetic energy from the flow over terrain calculated with Reynolds stress model

(a) Pha Taem topography, (b) Trapezoid geometry

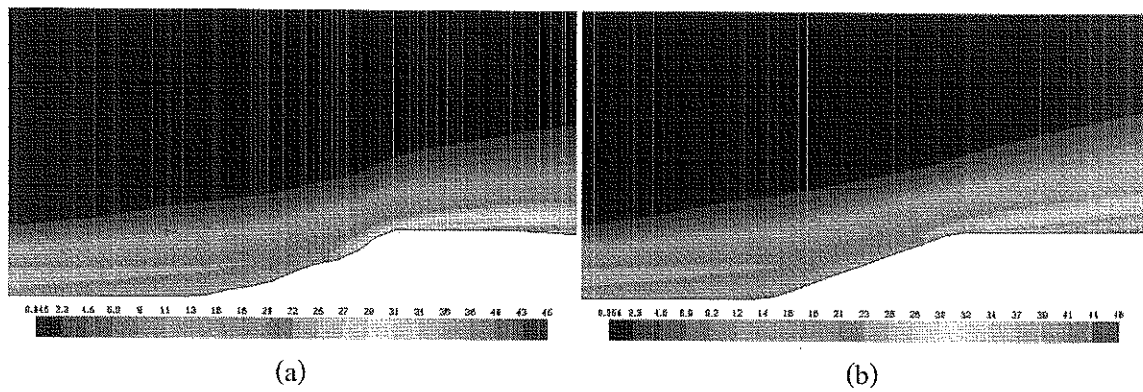


Figure. C.13 The contour plot of the turbulence intensity from the flow over terrain calculated with $k-\epsilon$ turbulence model

(a) Pha Taem topography, (b) Trapezoid geometry

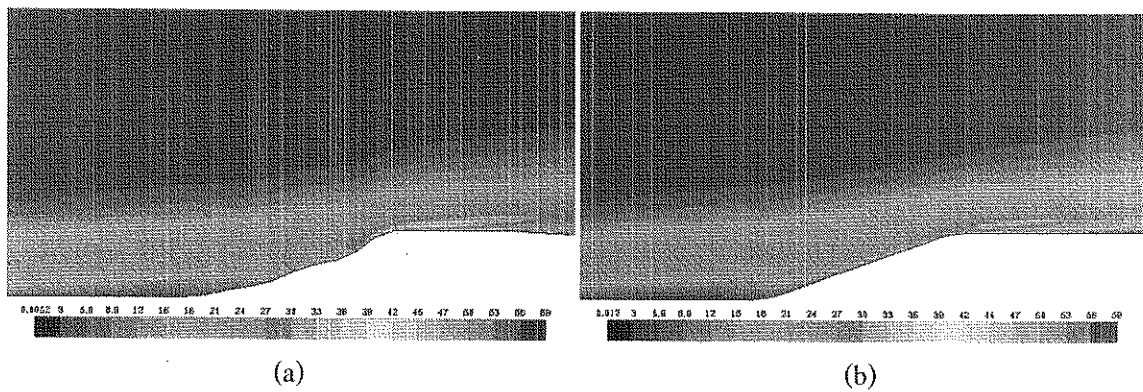


Figure. C.14 The contour plot of the turbulence intensity from the flow over terrain calculated with $k-\Omega$ turbulence model

(a) Pha Taem topography, (b) Trapezoid geometry

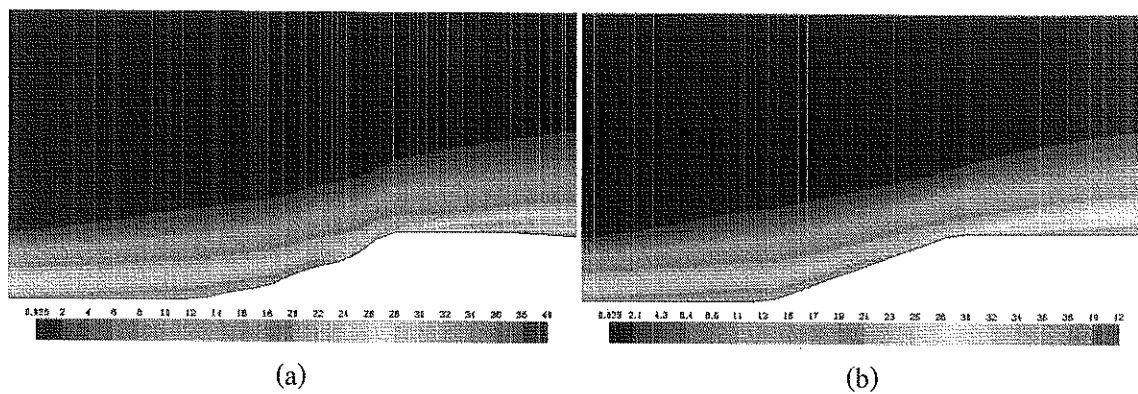


Figure. C.15 The contour plot of the turbulence intensity from the flow over terrain calculated with Reynolds stress model

(a) Pha Taem topography, (b) Trapezoid geometry

APPENDIX D
CODE PROGRAMING OF NEWTON'S EXTRAPOLATING POLYNOMIAL

Example Code Programing of Newton's extrapolation polynomial

Case : front hill angle is 20° and roughness height is 0.1 m.

SciLab 4.1.2 (x32) software

```

clc ; clear all;

//input distinct points

x = [2 4 6 8 10]; // Wind speed, V (m/s)
y = [0.13376 0.14729 0.16095 0.17476 0.18871] // F(V), x/H
yy = [0.11939 0.11976 0.12013 0.12050 0.12086] //F(V), y/H

//input point x to fine f(x)>>> Wind speed, V (m/s)

first_x = 12; //first desired point (x)
last_x = 40; //last desired point
dist_x = 2; //distance of each point
xx = []; //define desired point
iter = (last_x - first_x)/ dist_x +1; //iteration >> the number of desired point
for i =1: iter

    xx(i) = first_x + (i-1)*dist_x;

end

n = length(x);

printf("\n\n***** DISTINCT DATA ***** \n\n");
printf(" \tWind speed, V (m/s) \t\t\t F(V), x/H \t\t\t F(V), y/H \n\n")

for i = 1: n

    printf("\t %f\t\t\t\t\t %f\t\t\t\t\t %f\n",x(i),y(i),yy(i));

end

//compute the coefficients

for i =1: n

    c(i) = y(i);

    cc(i)= yy(i);

end

```

```

for i = 2:n
    for k = 1:n
        tem_c(k) = c(k);
        tem_cc(k) = cc(k);
    end
    for j = i:n
        c(j) = (tem_c(j) - tem_c(j-1))/(x(j)-x(j-i+1));
        cc(j) = (tem_cc(j) - tem_cc(j-1))/(x(j)-x(j-i+1));
    end
end

//compute desired f(x) at given x value
m = length(xx)
fx_1 = [ ];
fx_2 = [ ];
for i = 1:m //fine f(x) at each x
    fx_1(i) = c(1);
    fx_2(i) = cc(1);
    for j = 2: n //sum entire terms of formula
        cx_1 = c(j);
        cx_2 = cc(j);
        for k = 1: j-1 // multiply each term of formula >> coefficient and x-x(i)
            cx_1 = cx_1 *(xx(i)-x(k));
            cx_2 = cx_2 *(xx(i)-x(k));
        end
        fx_1(i) = fx_1(i) + cx_1;
        fx_2(i) = fx_2(i) + cx_2;
    end
end

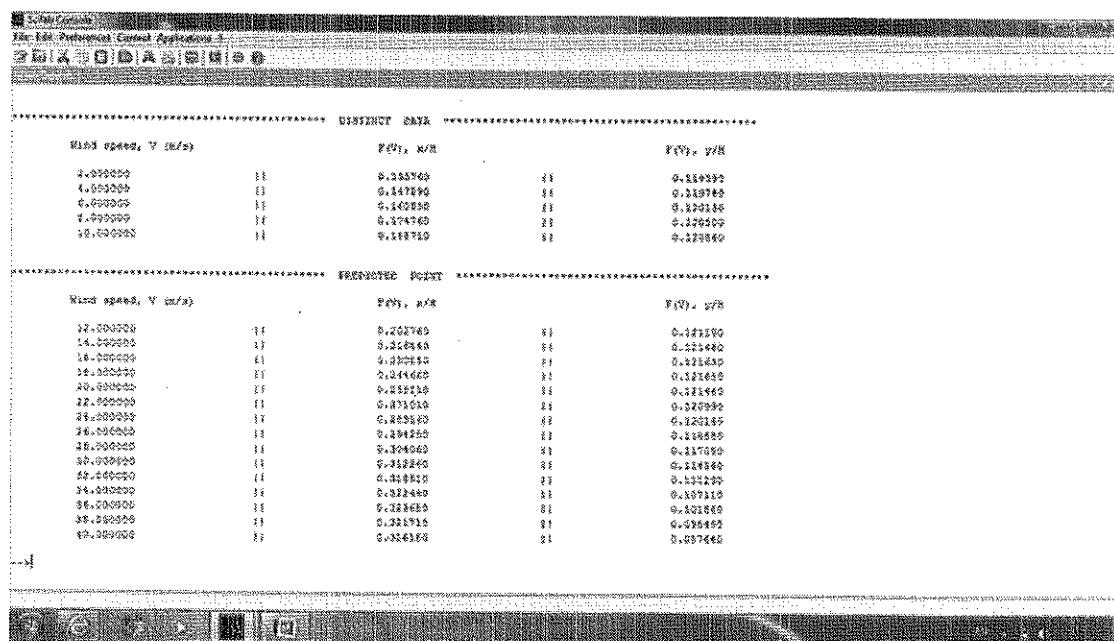
printf("\n\n***** PREDICTED POINT ***** \n\n");
printf("\tWind speed, V (m/s) \t\t\t F(V), x/H \t\t\t\t F(V), y/H \n\n")

```

```
for i = 1: length(xx)
    printf("\t %f\t\t ||\t\t %f\t\t ||\t\t %f\n",xx(i),fx_1(i),fx_2(i));
end
```

The programing results of SciLab 4.1.2 are indicated in Figure D.1. The SciLab console showed suitable positions of turbine with the initial conditions user input for the program. Figure D.1 illustrated result of program for case front hill angle is 20° and roughness height is 0.1 m.

Figure D.1 Result of SciLab console interface for SciLab 4.1.2 programing.



DISTINCT DATA		
Wind speed, V (m/s)	F(V), m/s	F(V), y/H
2.000000	0.265760	0.159392
4.000000	0.147890	0.149760
6.000000	0.100000	0.140100
8.000000	0.174760	0.176100
10.000000	0.118710	0.170000

EXTRACTED POINT		
Wind speed, V (m/s)	F(V), m/s	F(V), y/H
12.000000	0.202760	0.141100
14.000000	0.320000	0.121000
16.000000	0.300000	0.121000
18.000000	0.240000	0.121000
20.000000	0.250000	0.121000
22.000000	0.371010	0.120000
24.000000	0.385000	0.120000
26.000000	0.430000	0.118000
28.000000	0.400000	0.117000
30.000000	0.312200	0.114000
32.000000	0.310000	0.112000
34.000000	0.322000	0.107000
36.000000	0.280000	0.101000
38.000000	0.221710	0.095000
40.000000	0.354000	0.097000

APPENDIX E
WIND TURBINE SUITABLE SITE CHART INSTRUCTION MANUAL

Instruction manual of wind turbine suitable site chart

To assess suitable site of wind turbine of the flow over trapezoid shape, the chart have been used to identify. Data of the site should be provided associate with the wind data previously. Procedure of site selecting can be performing with follow step.

1. Measure wind speed

Measure wind speed data from site at 10 m height at least 3 years data with 1 hour period measured are sufficiency in the procedure. Mean wind speed of the site can calculate from

$$V_m = \left[\frac{\sum V_i}{N} \right]$$

2. Measure terrain structures

Terrain structures are important factor for site selecting. Height and front hill angle of the terrain can provided from GIS data or measure and calculate using GPS technology. While typical canopy height in surrounding can be observe from below table.

Table E.1 Typical roughness length

Land Cover Types	Typical Roughness Length (m)
Woodlands and forest	0.4-1.2
Farmland and grassy plains	0.002-0.30
Many trees and hedges, a few buildings	0.30
Scattered trees and hedges	0.15
Many hedges	0.085
Few trees (summer)	0.055
Crops and tall grass	0.050
Isolated trees	0.025
Few trees (winter)	0.010
Large expanses of water	0.0001-0.001
Flat desert	0.0001-0.001

3. Site selecting

After complete data collection of the site, chart sequence can be select from roughness height of terrain as show in Number (1).

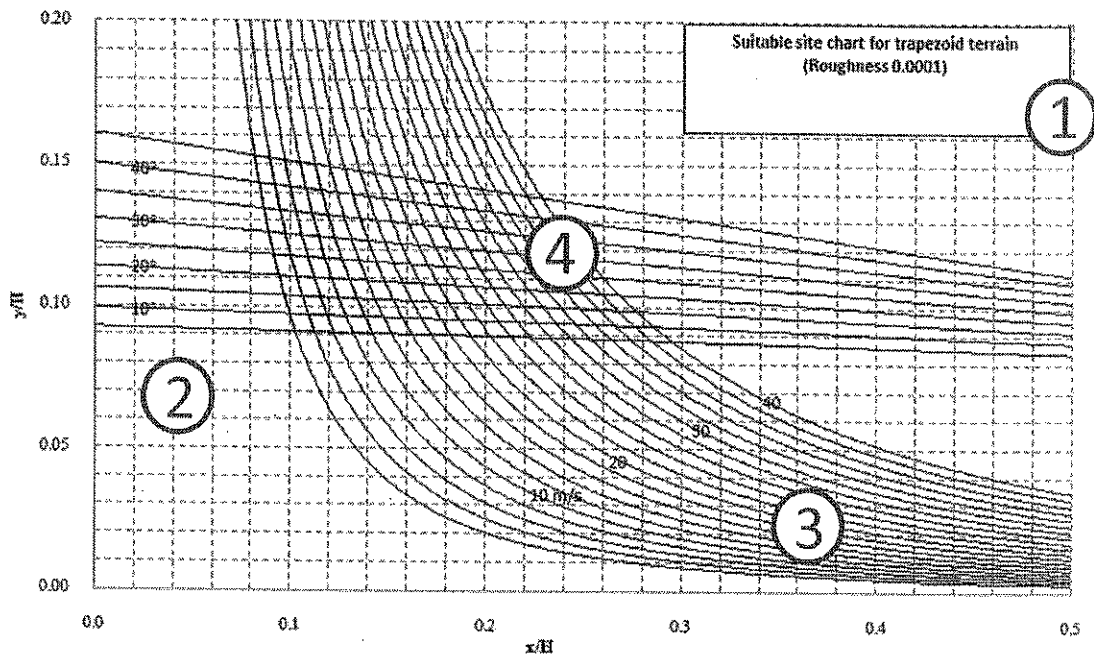


Figure E.1 Stage of site selection

To select site for wind turbine terrain structure and wind speed data are have been used in this section. Front hill angle can be select from horizontal lines Number (2), while mean wind speed data select from incline lines Number (3). Afterward, suitable site ratios with terrain height for turbine are indicated at intersection point at Number (4). Finally, calculations of actual position of turbine hub at site, multiply value in the chart with real height of the hill.

Example:

Pha Taem terrain has front hill angle is about 20° with 240 m height, and roughness height is 0.01 m. Mean wind speed from the site is 24 m/s parallel with front hill angle direction.

Site selection of wind turbine adopt from roughness 0.01 m sheet. Then, select site from intersection point of lines hill angle 20° and wind speed 24 m/s as show in below figure.

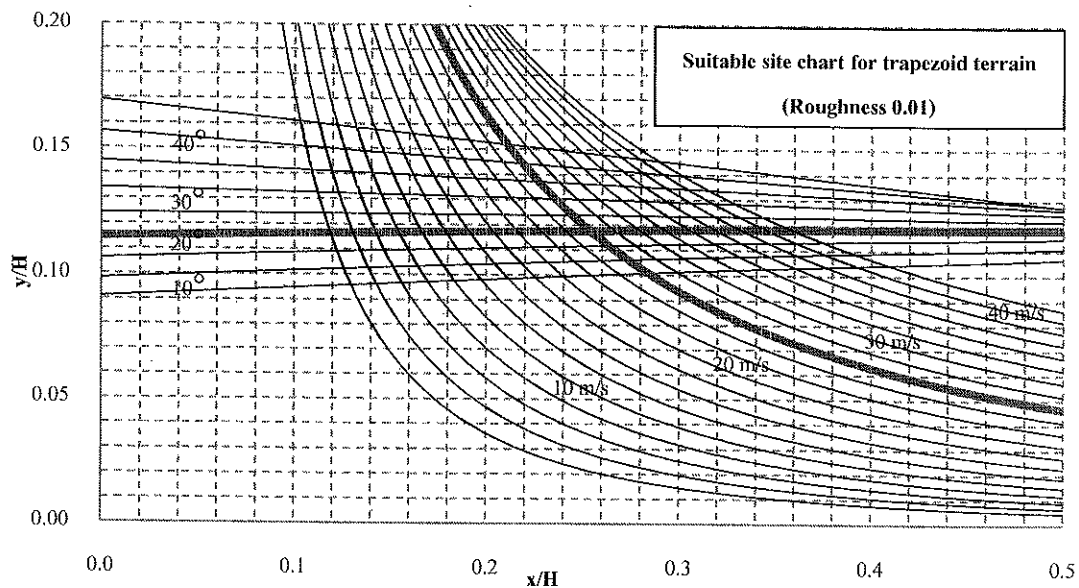


Figure E.2 Selecting intersection point from the chart

Obtaining site of wind turbine i 0.258 x/H in horizontal and 0.117 y/H in vertical.

Calculation actual site of turbine from real height of terrain are

- Horizontal direction

$$x = 0.258 \times 240 \text{ m} = 61.92 \text{ m}$$

- Vertical direction

$$y = 0.117 \times 240 \text{ m} = 28.08 \text{ m}$$

So, wind turbine should be installed at 61.92 m behind hill top and hub of the turbine should height 28.08 m from ground.

APPENDIX F
LIST OF PUBLICATIONS FROM THIS WORK

1. International Journal

Thitipong Unchai, Adun Janyalertadun and Arne Erik Holdø. "Wind Energy Potential Assessment as Power Generation Source in Ubonratchathani Province, Thailand", Wind Engineering, 36(2) : 131-144 ; 2012.

2. International Conference

T. Unchai, A. Janyalertadun and A.E. Holdø. "CFD on Wind Energy Potential Assessment in Ubonratchathani University" in 4th GMSARN International Conference on Energy Security and Climate Change: Problems & Issues in GMS, Vietnam : GMSARN, 25-27 November, 2009.

3. National Conference

Thitipong Unchai and Adun Janyalertadun. "CFD Evaluation of Wind Flow Over Hill: A Comparison of Trapezoid Hill Shape and Relatively Geometry", in The 8th Conference on Energy Technology Network of Thailand, Thailand : 2-4 May 2012.

VITAE

NAME

Mr.Thitipong Unchai

EDUCATION

2005, B.Sc.(Physics), Khon Kaen University

2007, M.Sc.(Applied Physics),

Naresuan University

WORK EXPERIENCE

2007-Present, Lecturer in Ubon Ratchathani

Rajabhat University

2010-Present, Researcher in Center of

Excellence for Environmental and Hazardous

Waste Management

POSITION AND WORKPLACE

2007-Present, Lecturer in Department of

Physics, Faculty of Science,

Ubon Ratchathani Rajabhat University